

UNIVERSITY  
OF OSLO

Aslak Wigdahl Bergersen

**On software tools and variability in  
medical image-based  
computational fluid dynamics**

**Thesis submitted for the degree of Philosophiae Doctor**

Department of Informatics  
Faculty of Mathematics and Natural Sciences

Simula Research Laboratory  
Department of Computational Physiology



**2023**

© **Aslak Wigdahl Bergersen, 2023**

*Series of dissertations submitted to the  
Faculty of Mathematics and Natural Sciences, University of Oslo  
No. 2611*

ISSN 1501-7710

All rights reserved. No part of this publication may be reproduced or transmitted, in any form or by any means, without permission.

Cover: UiO.  
Print production: Graphic Center, University of Oslo.

*To my daughter, wife, mother, stepfather, family, friends, and colleagues; this  
thesis is dedicated to you.*



# Preface

This thesis is submitted in partial fulfillment of the requirements for the degree of *Philosophiae Doctor* at the University of Oslo. The research presented here is conducted under the supervision of senior scientist Kristian Valen-Sendstad at Simula Research Laboratory from October 2016 to September 2022.

The thesis is a collection of four papers, all of which I am the first or co-first author of, and all the papers are published. The work is presented in chronological order of when it was conducted. The overarching theme is reproducibility in medical imaged-based computational fluid mechanics, with a focus on intracranial aneurysms. The papers are preceded by an introductory chapter that relates them together and provides background information and motivation for the work.

## Acknowledgements

I would like to extend my greatest gratitude to my supervisors; Kristian Valen-Sendstad, Joakim Sundnes, and Sam Wall for their advice and patience during this work.

I would also like to give a special thanks to Kristian Valen-Sendstad for always going the extra mile in your supervision. You have passed on a lot of knowledge to me, both in an academic and professional context.

A special thanks to the hospitality of Professor Alison Marsden and the members of the Marsden lab at Stanford University for hosting me for nine months during the work of this thesis. During the period of this thesis I have also been fortunate to also work closely with Professor David Steinman and his lab at University of Toronto, and Professor Patrick Sagers and his lab at University of Ghent, in particular Viviana Manchini. These collaborations have been important to me, and you all have my gratitude.

During my PhD I have had the pleasure of co-supervising four master students, to: Henrik, Andreas, Sebastian, and Guttorm I would like to thank for letting me part of your education.

I would also like to thank all my co-workers at Simula for all your thoughts during lunch, and my office mates over the years; Øyvind, Gabriel, Siri, Alex, Bernardo, and Alban. I would also like to thank Jonas van den Brink for your friendship, kindness, and excellent dinners.

## Preface

---

To my wife, Chloé Beate Steen, there is a million things I'd like to thank you for, but for brevity all I'll say is; I love you with all of my heart. To my family and friends, thank you for your support and patience over the years.

• **Aslak Wigdahl Bergersen**

Oslo, October 2022

# List of papers

## Paper I

Aslak W. Bergersen, Mikael Mortensen, and Kristian Valen-Sendstad 'The FDA nozzle benchmark: "In theory there is no difference between theory and practice, but in practice there is"'. In: *Journal of Numerical Methods in Biomedical Engineering* **35**(1) (2019), DOI: 10.1002/cnm.3150.

## Paper II

Kristian Valen-Sendstad\*, Aslak W. Bergersen\* (co-first), Yuji Shimogonya, Leonid Goubergrits, Jan Bruening, Jordi Pallares, Salvatore Cito, Senol Piskin, Kerem Pekkan, Arjan J. Geers, Ignacio Larrabide, Saikiran Rapaka, Viorel Mihalef, Wenyu Fu, Aike Qiao, Kartik Jain, Sabine Roller, Kent-Andre Mardal, Ramji Kamakoti, Thomas Spirka, Neil Ashton, Alistair Revell, Nicolas Aristokleous, J. Graeme Houston, Masanori Tsuji, Fujimaro Ishida, Prahlad G. Menon, Leonard D. Browne, Stephen Broderick, Masaaki Shojima, Satoshi Koizumi, Michael Barbour, Alberto Aliseda, Hernán G. Morales, Thierry Lefèvre, Simona Hodis, Yahia M. Al-Smadi, Justin S. Tran, Alison L. Marsden, Sreeja Vaippummadhom, G. Albert Einstein, Alistair G. Brown, Kristian Debus, Kuniyasu Niizuma, Sherif Rashad, Shin-ichiro Sugiyama, M. Owais Khan, Adam R. Updegrave, Shawn C. Shadden, Bart M. W. Cornelissen, Charles B. L. M. Majoie, Philipp Berg, Sylvia Saalfield, Kenichi Kono, and David A. Steinman 'Real-world variability in the prediction of intracranial aneurysm wall shear stress: The 2015 international aneurysm CFD challenge' In: *Cardiovascular Engineering and Technology*, **9**(4) DOI: 10.1016/j.jbiomech.2019.109342.

## Paper III

Aslak W. Bergersen, Christophe Chnafa, Diego Gallo, Marina Piccinelli, David A. Steinman, and Kristian Valen-Senstad 'Automated and objective removal of bifurcation aneurysms: incremental improvements, and validation against healthy controls.'. In: *Journal of Biomechanics* **96** (2019), DOI: 10.1016/j.jbiomech.2019.109342.

## Paper IV

Aslak W. Bergersen, Henrik A. Kjeldsberg, and Kristian Valen-Sendstad 'A framework for automated and objective modification of tubular structures: Application to the internal carotid artery'. In *International Journal of Numerical Methods in Biomedical Engineering* **36**(5) (2020), DOI: 10.1002/cnm.3330



# Contents

Preface	iii
List of papers	v
Contents	vii
<b>1 Introduction</b>	<b>1</b>
1.1 Medical background and societal impact . . . . .	1
1.2 Clinical problem and treatment options . . . . .	2
1.3 Image based computational fluid dynamics of intracranial aneurysms . . . . .	4
1.4 Motivation and objectives . . . . .	8
1.5 Summary of papers . . . . .	10
1.6 Discussion and future work . . . . .	14
<b>Bibliography</b>	<b>17</b>
<b>Papers</b>	<b>30</b>
<b>I The FDA nozzle benchmark: "In theory there is no     difference between theory and practice, but in practice     there is"</b>	<b>31</b>
<b>II Real-world variability in the prediction of intracranial     aneurysm wall shear stress: The 2015 international     aneurysm CFD challenge</b>	<b>43</b>
<b>III Automated and objective removal of bifurcation     aneurysms: Incremental improvements, and validation     against healthy controls</b>	<b>67</b>
<b>IV A framework for automated and objective modification     of tubular structures: Application to the internal carotid     artery</b>	<b>77</b>



# 1. Introduction

## 1.1 Medical background and societal impact

According to the *Global Burden of Disease Study 2019* [1], stroke is the second-leading cause of death worldwide, responsible for more than 6.55 million deaths in 2019 alone. Strokes fall into one of two categories, ischemic or hemorrhagic. An ischemic stroke occurs when an artery that supplies blood to the brain is blocked or narrowed, often caused by an unstable atherosclerotic plaque or a blood clot. In contrast, a hemorrhagic stroke, occurs when a blood vessel breaks open and blood leaks into the brain and is usually caused by intracranial aneurysms [2] that are often described as balloon-shaped blobs on blood vessels. For both categories of stroke, blood is prevented from flowing downstream, which may cause permanent brain tissue damage or death.

The prevalence of intracranial aneurysms is estimated to be 2–3% [3, 4]. At a population level, intracranial aneurysms have a low yearly rupture risk of only 0.05–1% [5, 6]. However, in a prospective follow-up study of unruptured aneurysms, almost 30% of aneurysms detected in patients under 50 years old ruptured during their lifetime [7]. In other words, even though the yearly rupture risk is low, the cumulative risk of rupture during a lifetime can be high, but the majority of aneurysms do not rupture. Aneurysm rupture has a mortality rate of around 50%, and of the survivors, only 25% report full recovery without any psychosocial or neurological problems [8]. Naturally, of equal importance is the personal tragedy of those affected.

Although intracranial aneurysms constitute only 5% of all strokes [9], they occur at a young age compared to other types of strokes, with a mean age of 50 years [4]. Notably, aneurysms are responsible for approximately 27% of the *years of life lost* due to stroke [10]. Combined with substantial direct costs [11], this highlights the significant societal impact of intracranial aneurysms.

Intracranial aneurysms are most often found on, or in the vicinity of, the arteries that constitute the circle of Willis [12, 13], as illustrated in Figure 1.1A. Arteries adapt continuously to the local hemodynamics, which can cause adverse long-term remodeling from abnormal stresses over the years. Endothelial cells, which line the lumen of the vessel as sketched in Figure 1.1B, sense the mechanical forces from the local hemodynamics. The stress from the local hemodynamics activates signaling pathways that increase or decrease the production of factors that relax or contract the wall both in the short and long term [14, 15, 16].

## 1. Introduction

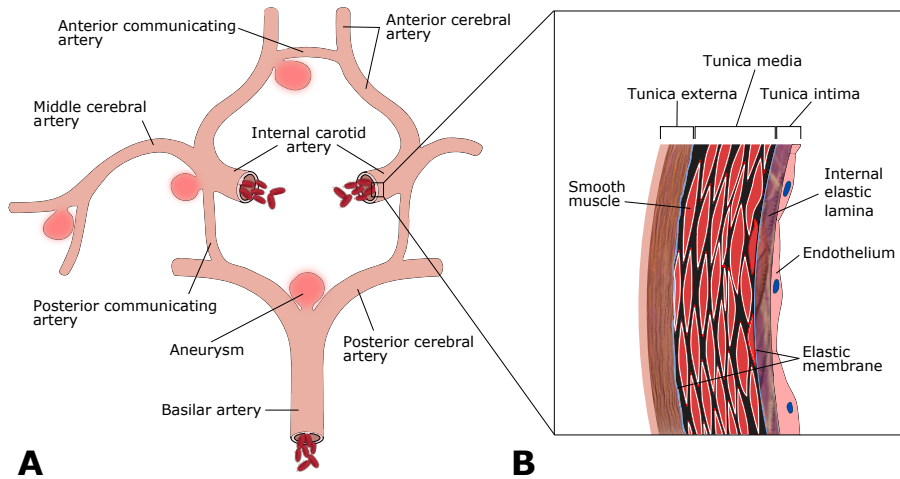


Figure 1.1: **A:** A sketch of circle of Willis, with blood flowing into the internal carotid arteries and basilar artery. The most common locations of an aneurysm are marked in the figure. **B:** A sketch of the composition of an artery wall.

Therefore, hemodynamic stresses play an important role in cardiovascular health, and abnormal stresses are of particular interest in many vascular pathologies, for instance, atherosclerosis in the coronaries [17, 18] and the common carotid artery [19, 20], and intracranial aneurysms [21, 22].

Intracranial aneurysms do not constitute one single disease but can be considered a shared manifestation of a wide range of diseases [23]. Regardless of the underlying condition, the initiation of an intracranial aneurysm is associated with abnormal hemodynamic stresses, such as high wall shear stress (WSS) [24]. The abnormal stresses are believed to disrupt the internal elastic lamina, which is in the inner layer of the vessel (Figure 1.1B) [25, 26, 27]. After the initial disruption, an aneurysm could start to form, presumably to repair the damaged wall [28]. The enlargement is most likely driven by a combination of adverse remodeling from hemodynamic stresses and wall expansion due to increased proliferation of the mural cells [29, 30]. While the pathogenesis of intracranial aneurysms is a mechanobiological problem that is not fully understood [30, 31], the instantaneous event of rupture is a mechanical problem: the stress exceeds the vessel wall strength, causing a rupture and hemorrhagic stroke.

## 1.2 Clinical problem and treatment options

Symptomatic unruptured aneurysms are generally treated immediately [31]. However, most aneurysms are asymptomatic and are detected incidentally when imaging for other purposes [32]. While treating asymptomatic unruptured aneurysms is a topic of debate [33], there is a consensus that the side effects of

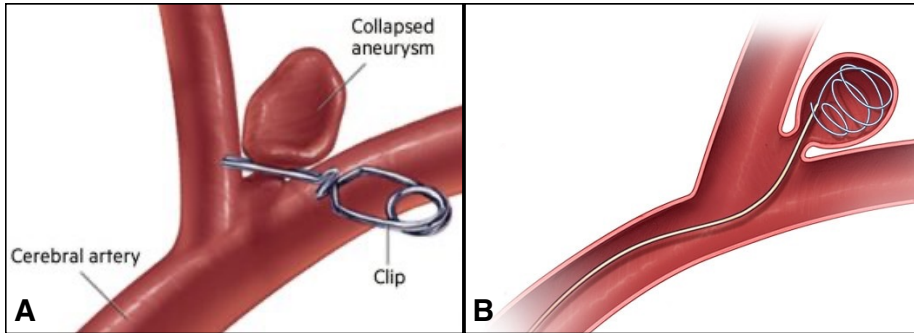


Figure 1.2: A sketch of the treatment options for intracranial aneurysms, **A**: A surgical approach: the aneurysm is clipped during open brain surgery. **B**: Endovascular treatment where a coil is being deposited into the aneurysm. Image credits: Mayo Clinic.

surgically treating all asymptomatic aneurysms outweigh the benefits [5].

The clinicians and patients are left with the option of operating on the aneurysm proactively or monitoring it over time. Currently, two commonly used approaches to proactive treatment exist: surgical and endovascular [34], both sketched in Figure 1.2. The former is an invasive open brain surgery where a small clip is placed on the aneurysm neck to prevent blood from entering the aneurysm. The less invasive option is placing a device, like a flow diverter or coil, into the aneurysm or artery to prevent blood from entering the aneurysm. The device is commonly deposited by entering the vasculature in the groin. Using coils or stents is considered less robust, and aneurysms recurrence is higher than clipping [35].

To create a patient-specific treatment strategy, it is important to consider known factors that correlate with the risk of rupture [36], for instance, the patient's demographic and genetic factors [37, 38], medical history [39, 40, 41, 42], and aneurysm-specific factors, such as its location, size, and morphology [43, 44]. Except for the size and morphology, these factors are not directly linked to the instantaneous event of aneurysm rupture. Therefore, there is potential to improve the identification of which aneurysms are at risk of rupture.

Ideally, we would have measured the vessel wall strength and thickness using medical imaging. However, compared to other locations in the human body, the vessel walls are much thinner intracranially relative to the lumen size [23]. Additionally, the vessel wall of aneurysms is even thinner, generally within the range of 30–200 micrometers [45, 46], which is too small to accurately resolve with current medical imaging.

Since WSS plays an essential role in the remodeling of arteries, a reasonable hypothesis might be that aneurysms with wall-thinning have different hemodynamic stress compared to a stable aneurysm. As a surrogate measure of wall strength and thickness, researchers have sought a link between the stresses

from local hemodynamics and rupture [21, 22]. While the local hemodynamics cannot be adequately measured through 3D medical imaging, the patient-specific vessel morphology can be reconstructed. This geometry can be combined with computational fluid dynamics (CFD) to simulate the patient-specific local hemodynamics [47]. Over the last three decades [48], researchers have used CFD as a tool to provide new insight into aneurysm formation [25, 27, 49], treatment [50, 51, 52], and rupture [21, 22, 53].

### 1.3 Image based computational fluid dynamics of intracranial aneurysms

In contrast to industrial CFD applications, there are no standard operating procedures for medical imaged-based CFD, and there is often no patient-specific measurement except the medical image. When performing a medical image-based CFD study, the modeler, therefore, faces many choices – for instance, assumptions for the boundary conditions [54, 55] or which sections of the vasculature to include in the segmentation [56, 57].

In this section, I provide a brief introduction to the steps taken in most medical image-based CFD studies. This serves as an overview of the simulations performed in this thesis, while also focusing on the many choices the researcher must make. Typically, the steps in a study of this kind include:

1. Acquiring images from a patient cohort, and segmenting them into a three-dimensional surface to generate a volumetric mesh.
2. Deciding upon a numerical approach for solving the Navier-Stokes equation for modeling the blood flow.
3. Prescribing plausible boundary conditions, often based on scaling laws correlating flow rates with vessel diameter, due to unknown patient-specific flow rates.
4. Post-processing the simulation results to create derived quantities that describe the stresses exerted on the vessel walls.

#### 1.3.1 Image acquisition, segmentation, and meshing

Setting idealized models aside, medical image-based CFD relies on scans from aneurysm patients. The most used imaging modalities are magnetic resonance angiogram, computed tomography angiography, three-dimensional digital subtraction angiography, and three-dimensional rotational angiography [58, 59], which is the current gold standard [60].

A medical image is segmented, based on the intensity of each voxel within it, to create a three-dimensional surface representing the patient’s aneurysm and surrounding vasculature. While multiple methods exist for image segmentation, level-set methods [61] are most frequently used, with the vascular modeling

tool kit (VMTK) [62, 63] being the most widely used tool [64]. Although many automated tools are available, segmentation remains manual and labor-intensive, with a median segmentation time of 6 hours [64]. Image segmentation is, therefore, a non-negligible bottleneck in the medical image-based CFD, complicating the analyses of larger patient cohorts.

To model blood flow using CFD, a volumetric mesh of the three-dimensional surface obtained from the segmentation is needed. To describe the resolution of the mesh, studies usually report the average characteristic length of the cells in the mesh, along with the number of cells. Notably, the mesh size should be suited for the combination of flow characteristics and CFD solver [65].

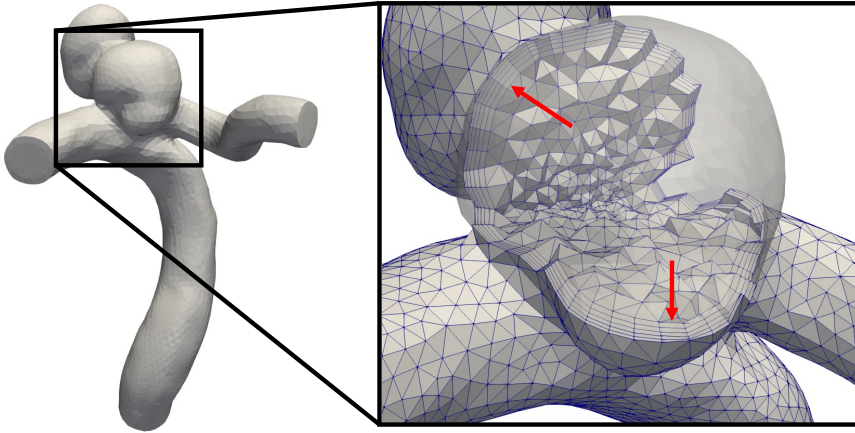


Figure 1.3: Illustrative example of a mesh with boundary layers, highlighted with red arrows.

To properly resolve the boundary layer of the flow along the wall, the gradient of the flow field should be well resolved in the normal direction of the wall. To achieve this, the mesh should also include a boundary layer along the wall, as illustrated in Figure 1.3, where the cells are shaped differently and are skewed towards the wall. Of note is that the boundary layer will also help to accurately estimate the WSS.

### 1.3.2 Numerical approximation of Navier-Stokes equation

CFD solvers numerically approximate a solution to the Navier-Stokes equation:

$$\frac{\partial \mathbf{u}}{\partial t} + \nabla \mathbf{u} = -\frac{1}{\rho} \nabla p + \frac{\mu}{\rho} \nabla^2 \mathbf{u} + \mathbf{f} \quad (1.1)$$

$$\nabla \cdot \mathbf{u} = 0 \quad (1.2)$$

where  $\mathbf{u}$  is the velocity,  $p$  is the pressure,  $\mathbf{f}$  is the body force,  $\rho$  is the fluid density, and  $\mu$  is the dynamic viscosity. For idealized problems with simplified

## 1. Introduction

---

boundary conditions and domains, there are analytical solutions to the Navier-Stokes equation, but there is no general analytical solution. However, we can approximate a solution numerically by splitting the domain of interest into a mesh, where we can numerically solve the discretized equation in each cell. The most common approximation methods in medical imaged-based CFD are finite volume and finite element. There is a wide range of general solution approaches, for instance, fully implicit, artificial compressibility, or operator splitting methods like projection schemes [66]. In this thesis, I used a finite element projection method without turbulence modeling [67, 68]. Specifically, I applied the open-source solver *Oasis* [69]. An essential aspect of this choice is the absence of added numerical viscosity and second-order spatial and temporal accuracy [70, 71].

Before results from a numerical solver can be trusted, it is necessary to perform verification and validation. The former checks if the equations are correctly implemented, for instance, with the method of manufactured solutions (MMS) [72]. MMS has been shown to catch all errors affecting the accuracy order introduced in a numerical scheme [73]. Validation is the process of checking if the correct equations are implemented. Specifically, one checks if the chosen solution approach is appropriate for a type of problem. For intracranial aneurysms, the solver should be validated for arterial blood flow with complex flow patterns that are turbulent-like, preferably following CFD-community guidelines [74, 75]. However, validation is a moving target, and additional validation can always be performed.

Simply having a verified and validated solver is insufficient when solving a specific application. It is also recommended to perform a convergence study to show appropriate spatial and temporal resolution [72, 74, 75]. However, researchers often reference the Reynolds number at that site in the cardiovascular system and, if less than 2300, argue that the flow should be laminar and that a solution approach for a laminar flow could be used. However, the Reynolds number is only relevant for a constant flow rate in a straight pipe. In contrast, the main supplier of blood to the brain, the internal carotid artery, is a "pipe" with curvature, torsion, variations in cross-sectional area, and a pulsatile flow, all of which can cause turbulent-like flows at lower Reynolds numbers. The assumption of a laminar flow might cause undetected turbulent-like flow characteristics in the literature [76, 77].

Blood is not a homogeneous fluid but consists of plasma and white and red blood cells. Instead of tracking each cell and its interaction with the fluid, the problem is commonly simplified by either applying a non-Newtonian viscosity model, like modified cross [78], or by assuming a Newtonian fluid with constant viscosity. Non-Newtonian models are created to mimic blood flow behavior irrespective of flow characteristics. For the flow characteristics in arteries, the viscosity of blood is approximately constant [79], and this assumption has been well studied [80, 81, 82]. All simulations presented in this thesis use the assumption that blood can be modeled as a Newtonian fluid.



### 1.3.3 Boundary conditions

Typically, patient-specific inlet boundary conditions are not acquired during imaging, and assumptions about inlet boundary conditions must be made when conducting a CFD study. These assumptions are usually related to (i) inlet velocity profile [56, 83, 55], (ii) how the flux changes during a heartbeat or waveform [84, 85], and (iii) mean flow rate during a heartbeat [54, 86, 87].

First, for the choice of inlet velocity profile, there are three common options: plug, parabolic, or Womersley. The most commonly used are plug inlet velocity profile (59%) and Womersley (25%) [88].

Second, when prescribing the waveform, the most straightforward approach is to ignore the pulsatility and apply a constant flux. Still, the most common method is to use a waveform from either a single patient [21] or population-averaged from patients with the same characteristics as typical aneurysm patients (older adults) [89]. A measured waveform can be scaled to achieve “patient-specific” flow rates.

Third, one needs to set the “patient-specific” mean flow rate during a heartbeat. This is done combining the population-average flow rate, which may range between 3.7mL/s to 4.6 mL/s [86], with a scaling law proportional to the vessel diameter. The scaling law incorporates the change in size of the vessel in response to the local hemodynamics [90]. It is commonly set as [91]: A constant flow rate ( $D^0$ ) [21], a constant velocity ( $D^2$ ) [92, 54], or a constant WSS ( $D^3$ ) [22]. This can be formulated as the following equation:

$$Q_i = Q_{average} \frac{D_i^n}{(D^n)_{average}} \quad (1.3)$$

where  $i$  represents one specific patient,  $Q_i$  is flux at the inlet for a particular patient,  $Q_{average}$  is the average flow rate for the population,  $n$  is the scaling, and  $D_{average}$  is the population average inlet diameter.

In contrast to inlet boundary conditions, where velocity is prescribed, it is more common to specify the pressure on the outlets. One common approach is to set the pressure to zero on all outlets [88]. The flow split is then dominated by the geometry, which means it is sensitive to segmentation choices and the number of outlets included [93]. Alternatively, one can precompute what the flow split should be based on vessel diameters [93, 94] and adjust the pressure boundary conditions in each timestep to reach the flow split target [95].

### 1.3.4 Derived quantities

As mentioned in section 1.2, aberrant WSS is believed to be correlated with aneurysm rupture. The most common hemodynamic index of interest is time averaged wall shear stress (TAWSS) [53]

$$\tau = \mu \frac{\partial u}{\partial y_w} \Big|_{w=0} \quad (1.4)$$

$$\text{TAWSS} = \frac{1}{T} \int_0^T |\tau| dt \quad (1.5)$$

## 1. Introduction

---

where  $\mu$  is the viscosity,  $y_w$  is the distance to the wall,  $u$  is the tangential velocity to the wall, and  $\tau$  is wall shear stress (WSS). From WSS there are many other derived indices, for instance, maximum WSS (MWSS) is commonly defined as the maximum of the TAWSS in the aneurysm dome. Another example is the low shear area (LSA), which is the proportion of area in the aneurysm where the WSS is lower than a threshold, for instance, 10% of MWSS. Also important is the oscillatory shear index (OSI) [96], which measures how similar the instantaneous WSS is to the TAWSS as defined by:

$$\text{OSI} = \frac{1}{2} \left( 1 - \frac{\left| \int_0^T \tau \, dt \right|}{\int_0^T |\tau| \, dt} \right) \quad (1.6)$$

All of these, TAWSS, MWSS, LSA, and OSI, have been reported to correlate with aneurysm rupture by different studies [53].

### 1.4 Motivation and objectives

Following the typical steps outlined in the above section, medical image-based CFD studies of intracranial aneurysms have shown promise as a research tool. However, the field has had several contentious areas, some of which could be attributed to the multitude of options and assumptions.

One of these is the seemingly contradictory result that low and high WSS correlate with aneurysm rupture. For instance, the studies from Meng et al. (2011) [21] and Cebal et al. (2011) [22], which used images from 106 and 128 patients, respectively, reached different conclusions. Meng et al. found a significant correlation between lower WSS and rupture, while Cebal et al. found that higher WSS correlates with rupture. An editorial in *American Journal of Neuroradiology* in 2012 addressed these inconsistencies and refers to CFD as both "*confounding factor dissemination*" and "*color for doctors*" [97]. In the editorial, it is explicitly stated that the field's computational scientists need to "*address the conflicting information*" to make CFD a clinically relevant tool. The editorial was quickly followed by three others [98, 99, 100].

The scientific discussion in these editorials culminated in a two-part review to explore the apparent contradictions in the data. In the first part, the authors proposed multiple pathways to aneurysm rupture, suggesting that both too low and too high WSS cause aneurysm initiation and growth, which ends in rupture [26]. The second part describes the different wall shear stress definitions in the literature and how this can be a source of discrepancy in reported values [101]. The new and unifying hypothesis from part one has gained much attention. However, to my knowledge, no study has combined or reexamined the two cohorts from Meng et al. and Cebal et al. using the same solution approach. For instance, the inlet boundary conditions were set to have the same flow rate for all patients in the study by Meng et al. In contrast, the WSS at the inlet was set to be constant in the study by Cebal et al. If there is a correlation between inlet artery size [102] and aneurysm rupture status, this would skew

the WSS results in opposite directions. It is therefore impossible to rule out the possibility that differences in the study design might have skewed the results.

The above example illustrates how methodological approach variability may result in inconsistent results between studies. To investigate the discrepancies, there have been organized *scientific community challenges*. The organizers invite research groups in the field to submit a solution to a specific problem. The results from each group are then collected and analyzed, making scientific community challenges an efficient and unbiased way to assess interlaboratory variability.

The first community challenge was triggered by the findings from [50], where they compared simulated pre-operative and post-operative blood flow based on imaging of seven giant aneurysms treated with a flow-diverting stent. Four aneurysms were successfully treated, and three ruptured after the treatment. Specifically, they pointed out that the relief of a pre-aneurysm stenosis could have caused aneurysm sac pressures to increase by 20–25 mmHg and caused the rupture. A scientific discussion followed in [103, 104], which argued that the pressure changes were unphysiologically high, again questioning the applicability of CFD as a robust research tool in combination with medical images. In the first community challenge, the 27 participating research groups were provided with the geometry, pulsatile flow rates, and blood properties as studied in [50] by the challenge organizers. On the other hand, the participants were free to select which meshing approach, numerical scheme, and CFD solver to apply. The outcome of the challenge showed that while simulated pressures were consistent [105], visually, there was relatively large variability in the peak-systolic velocity in the aneurysm sac. Some exhibited turbulent-like flows while others did not.

Although not explicitly aimed at intracranial aneurysm CFD, the "nozzle" benchmark launched by the *US Food and Drug Administration* (FDA) [106] added to the skepticism towards CFD as a robust research tool. The goal of the benchmark was two-fold: to compare experimental results from three laboratories to improve replicability and to use the results as a benchmark for CFD solvers. The benchmark consisted of a tubular structure with a nozzle into a throat section, followed by a sudden expansion, referred to as a "*generic medical device*". The experimental data was generated at three independent laboratories using a blood mimicking fluid with five flow rates corresponding to a Reynolds number of 500, 2000, 3500, 5000, and 6500 in the throat section. Blinded to the experimental results, 28 teams submitted numerical results of the same configurations, which showed both high interlaboratory variability and poor agreement with the experimental results [107].

We hypothesized that the problem is not that CFD is an inappropriate research tool in this context, but that there are reproducibility and replicability challenges that must be overcome. Instead of focusing on specific problems like the simulation approach or boundary conditions, I will focus on the challenges of replicability and reproducibility within the field. Since these issues also apply to other areas of science, my results are likely to benefit research beyond the use of CFD in aneurysm studies.

The scientific contributions of this thesis can be split into two categories. The first revisits the FDA benchmark (Paper I) and builds upon the work

from previous scientific community challenges (Paper II). The two first papers focus on community efforts towards improving replicability and robustness. The second part will focus on new open-source software tools which can facilitate reproducibility and replication and reduce manual labor (Paper III and Paper IV).

### 1.5 Summary of papers

#### **Paper I: The FDA nozzle benchmark: "In theory there is no difference between theory and practice, but in practice there is"**

The seminal paper by Valen-Sendstad et al. (2014) [76] shows that the spatiotemporal resolution and solution approaches most commonly utilized in the literature are too coarse to detect "turbulent-like" flow. This is consistent with the results in the scientific community challenge by Steinman et al. (2011) [105]. The solver used to perform what is referenced as "*high-resolution*" in [76] was the open-source solver *Oasis* [69]. Following up on [76], Khan et al. (2015) [77] compared the solution approach in *Oasis*, which is second order and minimally dissipative, with a more commonly used stabilized first-order solver and showed that acceptable levels of spatiotemporal resolution vary among solution approach. They found that *Oasis* could adequately resolve relevant indices at relatively low spatial and temporal resolutions and thus generate CFD results within clinically acceptable timeframes.

Research efforts of this kind are necessary if we are to regain confidence in CFD results and avoid future controversies. To build on these results and establish greater trust in *Oasis*, the study's goal was to provide further validation of the open-source solver *Oasis*. Each validation benchmark tests a specific aspect of a solver's capabilities and given the lack of consistent agreement between the 28 teams and the experimental results, we hypothesized that this benchmark was a good choice. However, as our computational results did not align with the experimental results from the benchmark, the paper has an extended discussion section to contextualize our results.

We focused on the transitional flow regime (3500) and found that when we spatially refined the mesh, the jet consistently broke down further downstream. We further investigated the cause of the inconsistency with i) a spectral element solver, ii) impact of noise at the inlet, iii) geometric distortion of mesh elements, and iv) comparing our outcomes with other results in the literature. Each of these approaches also indicated that the jet should not break down if the spatial and temporal resolution were improved beyond a threshold.

We conclude that high-fidelity CFD may introduce too little noise compared to the "noise" that is inherently present experimentally. Still, by adding noise, the benchmark gives consistent results and can be utilized by others. We also conclude that *Oasis* was successfully validated against the FDA benchmark.

## **Paper II: Real-world variability in the prediction of intracranial aneurysm wall shear stress: The 2015 international aneurysm CFD challenge**

One of the conclusions made by Steinman et al. (2011) in the first scientific community challenge was that future challenges should focus on hemodynamic indices thought to be of clinical interest. To follow up, a second challenge was launched to investigate rupture prediction between a ruptured and an unruptured aneurysm, in addition to predicting the rupture site [108, 109]. The 26 participating teams were only provided with the segmented lumen geometry in the first phase. The rupture prediction rate was very good (81%), despite considerable variation in mesh sizes and numerical approaches. However, only one team was able to predict the rupture site correctly [108]. In the second phase, participants were provided with flow rates and blood properties to isolate and investigate variation related to the chosen solution strategy alone on hemodynamic indices. These results showed reasonable agreement among teams [109]. One caveat is that participants had prior knowledge that one aneurysm was ruptured, and one was not. This does not mimic a clinical situation where the aneurysms would be assessed individually, and some teams might classify both as ruptured or unruptured. Therefore, the rupture predictions could be considered unnaturally high compared to a clinical setting.

As described in section 1.3, researchers must make many assumptions and choices when performing a medical image-based CFD of intracranial aneurysms. These assumptions have been studied individually by individual research groups [86, 93, 58]. In contrast, we organized and analyzed a scientific community challenge to quantify the variability in all steps of the medical image-based CFD pipeline, i.e., the total "real-world" variability. Participants were given medical images from five intracranial aneurysm cases and were asked to execute their version of the medical image-based CFD pipeline while reporting intermediate results and solution approaches.

While the challenge was well organized and had excellent participation, with 26 teams contributing to solutions, the results were slightly discouraging as there was little to no consensus on the approaches used by the teams. The results showed wide variability in nearly all intermediate steps of the pipeline and resulted in interquartile ranges of sac average WSS up to 56%. Normalizing WSS to the parent artery values reduced the variability, but there was modest consensus between the teams on the rank-ordering of the five cases based on WSS. Notably, we evaluated the teams' experience level in CFD of aneurysms and found that experience was not a significant predictor of variability. We published all the data in an online repository to allow replicability of the results and for others to perform new analyses [110].

While eliminating all interlaboratory variability may be difficult, our findings suggest it can be reduced by establishing guidelines for model extents, inflow rates, and blood properties; and by encouraging reporting of normalized hemodynamic parameters. Such guidelines could potentially help improve replicability and facilitate clinical adaptation of medical image-based CFD

in intracranial aneurysms.

The results from this scientific community challenge agree with those from previous events. In the first challenge [105], the flow conditions were such that the simulated flow results could be characterized as turbulent-like if adequately resolved. However, in the second challenge, the flow was laminar independent of the simulation approach, with much more consistent results than in the first challenge. Based on this observation alone, we can hypothesize that the ease of replicability in each case depends on the local fluid dynamics. This observation is further supported by studies comparing simulation approaches, showing that the flow dynamic can change from laminar to turbulent-like [76, 77]. Based on 50 bifurcation aneurysms, Khan et al. (2021) [111] found that the prevalence of flow instabilities is around 50% and is therefore not something that can be overlooked.

Together, these efforts demonstrate the power of scientific community challenges to address complex questions and quantify interlaboratory variability in the field while striving for reproducibility and replicability.

### **Paper III: Automated and objective removal of bifurcation aneurysms: Incremental improvements, and validation against healthy controls**

Based on the scripts and tools created for the analysis in Paper II, we identified a lack of open-source software tools for automatic and robust alteration of vascular geometries. An interesting research question is to determine whether there is a correlation between wall shear stresses and aneurysm rupture. However, there are inherent limitations, for instance, immunohistochemical staining show that many ruptured aneurysms had loss of endothelium and disorganized mural cells, both phenotypically different from a healthy vessel wall [112, 113]. Instead, one could focus on aneurysm initiation, but longitudinal imaging of patients that later develop aneurysms is rare. Instead, a commonly adopted strategy is to digitally remove the aneurysm and compute the WSS of the approximated pre-aneurysmal geometries.

Most research efforts have manually removed the aneurysm using smoothing or splining tools [114, 115, 116, 117, 118]. A caveat is that aneurysm removal is an operator-dependent and manual task, making these studies difficult to reproduce. At least three methods have been proposed for automatic parent artery reconstruction by Karmonik et al. (2004) [119], Ford et al. (2009) [120], and Chen et al. (2013) [121]. Karmonik et al.'s approach is to add a new circular surface in the aneurysm neck, identified by the distance from the centerline. The two other approaches, which are conceptually similar, find or mark where the aneurysm ends and extrapolate between these points. Of the three proposed methods, only Ford et al. can handle aneurysm removal irrespective of location. In other words, this method can remove both side-wall and bifurcation aneurysms. However, the final comment in the manuscript from Ford et al. states: "(...)

*while the parent artery reconstructions are plausible, it remains to be proven that they are faithful representations of the pre-aneurysmal artery".*

Following up on the study by Ford et al., we sought to perform a validation of the method against healthy controls to check if we could reconstruct the bifurcation. Additionally, from our previous usage of the tool, we hypothesized that an artificial notch in the apex of the bifurcations was influencing the results. Therefore, we suggested an improvement to the method and validated it with healthy controls using the solver *Oasis* from Paper I.

In our validation, we found that the computed indices are reasonably similar when comparing the original and reconstructed surfaces. Furthermore, we improved the previously proposed algorithm by not only "extrapolating" the Voronoi diagram from the parent artery to the daughter branches and vice-versa, but also between the daughter branches. The results from the improved method were validated such that future studies can use the method with confidence and with a better understanding of its accuracy.

Of note is that, although the reconstruction might be accurate based on the current geometry, it still might not be a good representation of the pre-aneurysmal situation. During aneurysm growth, it might interact with the perianeurysmal environment (like bone) which would affect the parent vessel geometry [122].

#### **Paper IV: A framework for automated and objective modification of tubular structures: Application to the internal carotid artery**

As mentioned in the summary of Paper III, the pre-aneurysmal geometries are simply approximations. This is a limitation that might never be completely overcome; however, we can use another approach to study aneurysm initiation.

A widely accepted hypothesis is that aberrant hemodynamic stresses cause remodeling and aneurysm initiation. If this is the case, then the stress at the sites of aneurysm initiation should differ from locations where aneurysms did not develop. However, structural and fluid properties, flow rates, and morphology ultimately determine the local hemodynamics. Structural and fluid properties are considered to be rather homogeneous in the population, while flow rates correlate with vessel size [86]. In contrast, specific morphological features are statistically different compared with healthy controls [92, 123, 124]. It would therefore be of interest to investigate the impact of altering one of these morphological features, while keeping everything else fixed, and observe the changes in hemodynamics.

This could be achieved by studying hundreds of cases and correlating morphology and hemodynamic indices. However, separating the impact of each morphological feature is a challenge. Furthermore, segmentation is manual and labor-intensive. Parametrized, idealized models are an alternative to using medical images to obtain a three-dimensional surface. Idealized models have a mathematical description, such as perfect tubular pipes with spherical blobs mimicking blood vessels and aneurysms. Such simplified models have been used to perform proof-of-concept studies that explore how changes in morphology impact hemodynamics [125, 126]. However, an inherent drawback is that the

geometries are often too simplistic as they do not have the same variation of curvature, torsion, and cross-sectional area as patient-specific geometries.

This study aimed to combine the best from both approaches and allow for parameterized patient-specific models. To this end, we heavily relied upon the core concept of the method in Paper III: the Voronoi diagram. The Voronoi diagram can be viewed as an analog to a Fourier series of a signal, where one can decompose and individually manipulate specific sections or "frequencies". In the Voronoi diagram, the three-dimensional surface is represented by spheres that are tangential to the surface. Each sphere can be represented by a point (center) and a radius. The reconstructed surface could be manipulated by either moving the points, adjusting the radius, or removing spheres.

We present a new framework for morphological manipulation, *morphman*, that allows researchers to objectively alter the area, move branches, alter angles of bifurcations, and manipulate the curvature. For instance, the cross-sectional area can be changed, a fusiform aneurysm or stenosis may be created, or the cross-sectional area variations along a segment can be increased or decreased. The framework is presented as a well-documented open-source software that is free for others to use and adapt. Although motivated by aneurysm initiation, the methods can be applied to any tubular structure. We have performed an example where we manipulated a left ventricular atrium (heart) morphology and simulated the blood flow in both geometries.

### 1.6 Discussion and future work

Up to this point, I have focused on replicability and reproducibility of medical image-based CFD in intracranial aneurysms, and the results from Paper II paint a grim picture of the current state. This raises the question: is this problem specific to this field, or is it a broader problem within scientific research?

Over the last decade, researchers have made several comprehensive large-scale replication and reproducibility efforts [127, 128, 129], and there have been published new guidelines and recommendations from scientific societies [130, 131]. All give the same message: replicability rates must improve. Specifically, in cancer biology, The Reproducibility Project: Cancer Biology prepared to investigate 53 high-profile papers, but the researchers found that more than half of the studies could not be replicated owing to missing critical methodological information. Only one in ten studies could be fully replicated [132]. Similarly, The Open Science Collaboration [127] tried to replicate the experiments from 100 published papers in psychology. Of these, 97% of the original experiments reported significant results, in contrast to only 36% of the new experiments, which also showed much smaller effect sizes.

The above studies show that the replicability rate is below 50% in these fields. *Nature's* 2016 survey on reproducibility [133] suggests that this holds true for other areas of science too. The survey, which assessed reproducibility across a range of research fields, garnered the opinions of 1576 scientists about whether there is a reproducibility crisis in science. 90% replied that there is a



slight or significant crisis, 3% answered that there is no crisis, and 7% said they do not know. Alarming, 27% responded that less than half of the papers in their field could be trusted, and surprisingly more than half of the respondents answered that they have failed to reproduce their own results. Reproducibility is a significant problem across almost all scientific disciplines. Alternatively, quoting Open Science Collaboration (2015) [127], "... *there is still more work to do to verify whether we know what we think we know*".

A common first step in a new research effort is to reproduce a previous study. Building on what we know to be in accordance with previous work, we can alter the study design to investigate a new hypothesis. However, an absence of code, data, or basic key methodological information hinders such efforts. For instance, for intracranial aneurysms, a review by Liang et al. (2019) [53], which evaluated CFD studies focusing on aneurysm rupture, found that papers often failed to report several critical methodological details. Of the 46 studies included, four out of five reported the number of cardiac cycles simulated (79%) and spatial resolution (80%), while only half reported temporal resolution (53%) and inflow conditions (54%). The lack of methodological details makes it impossible for others to reliably replicate the study results. A similar point was raised by Valen-Sendstad et al. (2014) [76], who noted that studies rarely provide enough detail about the spatial resolution (i.e., node spacing, element types, and mesh sizes) or solver parameters to enable others to accurately reproduce the work.

Out of curiosity, I attempted to quantify how many medical image-based CFD studies disclose enough methodological details to be reproducible. To find relevant studies, I used the following search term: "CFD / Computational Fluid Dynamic / Computational Fluid Dynamics / Computer Simulation / Computational Hemodynamics AND Brain / Cerebral / Intracranial AND aneurysm" in *PubMed* on November 30th, 2020, resulting in 1540 matches. The search term is adapted from Liang et al. (2020) [53] but leaves out "rupture" from the keywords. The results from the *PubMed* search were enriched with the number of citations from *Google Scholar*. For a study to be included, it must describe a CFD simulation that plays a key role in the study's conclusions, and is applied to, or relevant to, intracranial aneurysms. I then systematically went through the most cited papers until I found 50 that matched the inclusion criteria.

Each manuscript was evaluated based on 19 criteria divided into five categories: data acquisition, segmentation and mesh, numerical modeling, post-processing, and code. The raw data, the script for adding citations, the link to perform the same search later, the processed data, and a description of the 19 criteria can be found in an online data repository [134]. None of the studies provided adequate information to meet these criteria, and the median number of criteria met was 7 (37%). Surprisingly, none of these studies shared any code or data (like mesh or segmented models), thus none are reproducible. Of note is that these 50 studies used medical images from 857 patients (assuming no overlap between studies). If these images were shared, it would facilitate a range of new studies. Sharing methodological details is a simple, critical step in accelerating research, and future work is needed to systematically measure the

extent and propose mitigating efforts to improve reproducibility.

All the studies in this thesis were performed with the goal of open science and reproducibility. Specifically, in Paper I, we validated an open-source solver, *Oasis*, so that future users can be confident that this solver is well-suited for similar applications. In Paper II, we made all data and results available as an online resource [110] to enable future re-analysis or cross-challenge meta-analysis studies. In Paper III, the software implementation was published open source along with a detailed tutorial for easy access and reproducibility. The code used for meshing, running the CFD simulation, and post-processing, are all hosted on the collaborative version control platform GitHub [135], adding to the growing number of tools available for better reproducibility. In Paper IV, we present methods for reproducibly and robustly altering relevant morphological properties of arteries, which solves a problem that previously only had a manual, and thereby labor-intensive and hard-to-reproduce, alternative.

Fortunately, reproducibility and replicability have gained significant attention in recent years. Specifically, in medical image-based CFD for intracranial aneurysms, better reproducibility and replicability may help advance CFD as a robust research tool, which ultimately could assist clinicians in improving treatment strategy and patient outcomes. The scientific community is moving in the right direction: towards an increased awareness of the issues and more stringent guidelines for openness. This thesis is a contribution toward this goal. Every step towards openness and reproducibility will accelerate scientific progress, thus facilitating innovation.

# Bibliography

- [1] Feigin, V. L. et al. “Global, regional, and national burden of stroke and its risk factors, 1990–2019: A systematic analysis for the Global Burden of Disease Study 2019”. In: *The Lancet Neurology* vol. 20, no. 10 (2021), pp. 795–820.
- [2] Grotta, J. C. et al. *Stroke E-Book: Pathophysiology, diagnosis, and management*. Elsevier Health Sciences, 2021.
- [3] Rinkel, G. J. et al. “Prevalence and risk of rupture of intracranial aneurysms: a systematic review”. In: *Stroke* vol. 29, no. 1 (1998), pp. 251–256.
- [4] Vlak, M. H. et al. “Prevalence of unruptured intracranial aneurysms, with emphasis on sex, age, comorbidity, country, and time period: a systematic review and meta-analysis”. In: *The Lancet Neurology* vol. 10, no. 7 (2011), pp. 626–636.
- [5] Unruptured Intracranial Aneurysms Investigators, I. S. of. “Unruptured intracranial aneurysms—risk of rupture and risks of surgical intervention”. In: *New England Journal of Medicine* vol. 339, no. 24 (1998), pp. 1725–1733.
- [6] Juvela, S., Porras, M., and Poussa, K. “Natural history of unruptured intracranial aneurysms: probability of and risk factors for aneurysm rupture”. In: *Journal of neurosurgery* vol. 93, no. 3 (2000), pp. 379–387.
- [7] Korja, M., Lehto, H., and Juvela, S. “Lifelong rupture risk of intracranial aneurysms depends on risk factors: a prospective Finnish cohort study”. In: *Stroke* vol. 45, no. 7 (2014), pp. 1958–1963.
- [8] Kool Hieke MD Albrecht Kees WMD Rinkel Gabriël JEMD, A. S. after Treatment for Ruptured Aneurysms Study Group Wermer Marieke JHMD m. wermer@umcutrecht.nl. “Subarachnoid hemorrhage treated with clipping: long-term effects on employment, relationships, personality, and mood”. In: *Neurosurgery* vol. 60, no. 1 (2007), pp. 91–98.
- [9] Van Gijn, J., Kerr, R. S., and Rinkel, G. J. “Subarachnoid haemorrhage”. In: *The Lancet* vol. 369, no. 9558 (2007), pp. 306–318.

- [10] Johnston, S. C., Selvin, S., and Gress, D. R. “The burden, trends, and demographics of mortality from subarachnoid hemorrhage”. In: *Neurology* vol. 50, no. 5 (1998), pp. 1413–1418.
- [11] Rivero-Arias, O., Gray, A., and Wolstenholme, J. “Burden of disease and costs of aneurysmal subarachnoid haemorrhage (aSAH) in the United Kingdom”. In: *Cost effectiveness and resource allocation* vol. 8, no. 1 (2010), pp. 1–12.
- [12] Alpers, B. J., Berry, R. G., and Paddison, R. M. “Anatomical studies of the circle of Willis in normal brain”. In: *AMA Archives of Neurology & Psychiatry* vol. 81, no. 4 (1959), pp. 409–418.
- [13] Alpers, B. J. and Berry, R. G. “Circle of Willis in cerebral vascular disorders: the anatomical structure”. In: *Archives of Neurology* vol. 8, no. 4 (1963), pp. 398–402.
- [14] Chien, S. “Effects of disturbed flow on endothelial cells”. In: *Annals of biomedical engineering* vol. 36, no. 4 (2008), pp. 554–562.
- [15] Diamond, S., Eskin, S., and McIntire, L. “Fluid flow stimulates tissue plasminogen activator secretion by cultured human endothelial cells”. In: *Science* vol. 243, no. 4897 (1989), pp. 1483–1485.
- [16] Brooks, A. R., Lelkes, P. I., and Rubanyi, G. M. “Gene expression profiling of human aortic endothelial cells exposed to disturbed flow and steady laminar flow”. In: *Physiological genomics* vol. 9, no. 1 (2002), pp. 27–41.
- [17] Taylor, C. A., Fonte, T. A., and Min, J. K. “Computational fluid dynamics applied to cardiac computed tomography for noninvasive quantification of fractional flow reserve: scientific basis”. In: *Journal of the American College of Cardiology* vol. 61, no. 22 (2013), pp. 2233–2241.
- [18] Kwak, B. R. et al. “Biomechanical factors in atherosclerosis: mechanisms and clinical implications”. In: *European heart journal* vol. 35, no. 43 (2014), pp. 3013–3020.
- [19] Lee, S.-W. et al. “Geometry of the carotid bifurcation predicts its exposure to disturbed flow”. In: *Stroke* vol. 39, no. 8 (2008), pp. 2341–2347.
- [20] Nixon, A. M., Gunel, M., and Sumpio, B. E. “The critical role of hemodynamics in the development of cerebral vascular disease: a review”. In: *Journal of neurosurgery* vol. 112, no. 6 (2010), pp. 1240–1253.
- [21] Xiang, J. et al. “Hemodynamic–morphologic discriminants for intracranial aneurysm rupture”. In: *Stroke* vol. 42, no. 1 (2011), pp. 144–152.
- [22] Cebal, J. R. et al. “Quantitative characterization of the hemodynamic environment in ruptured and unruptured brain aneurysms”. In: *American Journal of Neuroradiology* vol. 32, no. 1 (2011), pp. 145–151.
- [23] Krings, T. et al. “Intracranial aneurysms: from vessel wall pathology to therapeutic approach”. In: *Nature Reviews Neurology* vol. 7, no. 10 (2011), pp. 547–559.

- 
- [24] Chalouhi, N. et al. “Biology of intracranial aneurysms: role of inflammation”. In: *Journal of Cerebral Blood Flow & Metabolism* vol. 32, no. 9 (2012), pp. 1659–1676.
- [25] Meng, H. et al. “Complex hemodynamics at the apex of an arterial bifurcation induces vascular remodeling resembling cerebral aneurysm initiation”. In: *Stroke* vol. 38, no. 6 (2007), pp. 1924–1931.
- [26] Meng, H et al. “High WSS or low WSS? Complex interactions of hemodynamics with intracranial aneurysm initiation, growth, and rupture: toward a unifying hypothesis”. In: *American Journal of Neuroradiology* vol. 35, no. 7 (2014), pp. 1254–1262.
- [27] Kulcsár, Z. et al. “Hemodynamics of cerebral aneurysm initiation: the role of wall shear stress and spatial wall shear stress gradient”. In: *American Journal of neuroradiology* vol. 32, no. 3 (2011), pp. 587–594.
- [28] Frosen, J. et al. “Remodeling of saccular cerebral artery aneurysm wall is associated with rupture: histological analysis of 24 unruptured and 42 ruptured cases”. In: *Stroke* vol. 35, no. 10 (2004), pp. 2287–2293.
- [29] Frösen, J. et al. “Saccular intracranial aneurysms: pathology and mechanisms”. In: *Acta neuropathologica* vol. 123, no. 6 (2012), pp. 773–786.
- [30] Chalouhi, N., Hoh, B. L., and Hasan, D. “Review of cerebral aneurysm formation, growth, and rupture”. In: *Stroke* vol. 44, no. 12 (2013), pp. 3613–3622.
- [31] Williams, L. N. and Brown, R. D. “Management of unruptured intracranial aneurysms”. In: *Neurology: Clinical Practice* vol. 3, no. 2 (2013), pp. 99–108.
- [32] Gabriel, R. A. et al. “Ten-year detection rate of brain arteriovenous malformations in a large, multiethnic, defined population”. In: *Stroke* vol. 41, no. 1 (2010), pp. 21–26.
- [33] Korja, M. and Kaprio, J. “Controversies in epidemiology of intracranial aneurysms and SAH”. In: *Nature Reviews Neurology* vol. 12, no. 1 (2016), p. 50.
- [34] Seibert, B. et al. “Intracranial aneurysms: review of current treatment options and outcomes”. In: *Frontiers in neurology* vol. 2 (2011), p. 45.
- [35] Crobeddu, E et al. “Review of 2 decades of aneurysm-recurrence literature, part 1: reducing recurrence after endovascular coiling”. In: *American Journal of Neuroradiology* vol. 34, no. 2 (2013), pp. 266–270.
- [36] Etminan, N. et al. “The unruptured intracranial aneurysm treatment score: a multidisciplinary consensus”. In: *Neurology* vol. 85, no. 10 (2015), pp. 881–889.
- [37] Ronkainen, A. et al. “Familial intracranial aneurysms”. In: *The Lancet* vol. 349, no. 9049 (1997), pp. 380–384.

- [38] Wermer, M. J. et al. “Risk of rupture of unruptured intracranial aneurysms in relation to patient and aneurysm characteristics: an updated meta-analysis”. In: *Stroke* vol. 38, no. 4 (2007), pp. 1404–1410.
- [39] Bonita, R. “Cigarette smoking, hypertension and the risk of subarachnoid hemorrhage: a population-based case-control study.” In: *Stroke* vol. 17, no. 5 (1986), pp. 831–835.
- [40] Knekt, P. et al. “Risk factors for subarachnoid hemorrhage in a longitudinal population study”. In: *Journal of clinical epidemiology* vol. 44, no. 9 (1991), pp. 933–939.
- [41] Korja, M. et al. “Risk factors and their combined effects on the incidence rate of subarachnoid hemorrhage—a population-based cohort study”. In: *PloS one* vol. 8, no. 9 (2013), e73760.
- [42] Sandvei, M. S. et al. “Risk factors for aneurysmal subarachnoid hemorrhage in a prospective population study: the HUNT study in Norway”. In: *Stroke* vol. 40, no. 6 (2009), pp. 1958–1962.
- [43] Kamp, L. T. van der et al. “Risk of rupture after intracranial aneurysm growth”. In: *JAMA neurology* vol. 78, no. 10 (2021), pp. 1228–1235.
- [44] Raghavan, M. L., Ma, B., and Harbaugh, R. E. “Quantified aneurysm shape and rupture risk”. In: *Journal of neurosurgery* vol. 102, no. 2 (2005), pp. 355–362.
- [45] MacDonald, D. J., Finlay, H. M., and Canham, P. B. “Directional wall strength in saccular brain aneurysms from polarized light microscopy”. In: *Annals of biomedical engineering* vol. 28, no. 5 (2000), pp. 533–542.
- [46] Kadasi, L. M., Dent, W. C., and Malek, A. M. “Cerebral aneurysm wall thickness analysis using intraoperative microscopy: effect of size and gender on thin translucent regions”. In: *Journal of neurointerventional surgery* vol. 5, no. 3 (2013), pp. 201–206.
- [47] Taylor, C. A. and Steinman, D. A. “Image-based modeling of blood flow and vessel wall dynamics: applications, methods and future directions”. In: *Annals of biomedical engineering* vol. 38, no. 3 (2010), pp. 1188–1203.
- [48] Steinman, D. A. et al. “Image-based computational simulation of flow dynamics in a giant intracranial aneurysm”. In: *American Journal of Neuroradiology* vol. 24, no. 4 (2003), pp. 559–566.
- [49] Can, A. and Du, R. “Association of hemodynamic factors with intracranial aneurysm formation and rupture: systematic review and meta-analysis”. In: *Neurosurgery* vol. 78, no. 4 (2016), pp. 510–520.
- [50] Cebal, J. et al. “Aneurysm rupture following treatment with flow-diverting stents: computational hemodynamics analysis of treatment”. In: *American journal of neuroradiology* vol. 32, no. 1 (2011), pp. 27–33.

- 
- [51] Ouared, R. et al. “Computational fluid dynamics analysis of flow reduction induced by flow-diverting stents in intracranial aneurysms: a patient-unspecific hemodynamics change perspective”. In: *Journal of NeuroInterventional Surgery* vol. 8, no. 12 (2016), pp. 1288–1293.
- [52] Janiga, G. et al. “An automatic CFD-based flow diverter optimization principle for patient-specific intracranial aneurysms”. In: *Journal of biomechanics* vol. 48, no. 14 (2015), pp. 3846–3852.
- [53] Liang, L. et al. “Towards the Clinical utility of CFD for assessment of intracranial aneurysm rupture—a systematic review and novel parameter-ranking tool”. In: *Journal of neurointerventional surgery* vol. 11, no. 2 (2019), pp. 153–158.
- [54] Valen-Sendstad, K. et al. “Estimation of inlet flow rates for image-based aneurysm CFD models: where and how to begin?” In: *Annals of biomedical engineering* vol. 43, no. 6 (2015), pp. 1422–1431.
- [55] Marzo, A. et al. “Influence of inlet boundary conditions on the local haemodynamics of intracranial aneurysms”. In: *Computer methods in biomechanics and biomedical engineering* vol. 12, no. 4 (2009), pp. 431–444.
- [56] Castro, M., Putman, C. M., and Cebal, J. “Computational fluid dynamics modeling of intracranial aneurysms: effects of parent artery segmentation on intra-aneurysmal hemodynamics”. In: *American Journal of Neuroradiology* vol. 27, no. 8 (2006), pp. 1703–1709.
- [57] Hua, Y., Oh, J. H., and Kim, Y. B. “Influence of parent artery segmentation and boundary conditions on hemodynamic characteristics of intracranial aneurysms”. In: *Yonsei medical journal* vol. 56, no. 5 (2015), pp. 1328–1337.
- [58] Ren, Y. et al. “Reproducibility of image-based computational models of intracranial aneurysm: a comparison between 3D rotational angiography, CT angiography and MR angiography”. In: *Biomedical engineering online* vol. 15, no. 1 (2016), pp. 1–14.
- [59] Berg, P et al. “Does the DSA reconstruction kernel affect hemodynamic predictions in intracranial aneurysms? An analysis of geometry and blood flow variations”. In: *Journal of neurointerventional surgery* vol. 10, no. 3 (2018), pp. 290–296.
- [60] Rooij, W. J. van et al. “3D rotational angiography: the new gold standard in the detection of additional intracranial aneurysms”. In: *American Journal of Neuroradiology* vol. 29, no. 5 (2008), pp. 976–979.
- [61] Li, C. et al. “Distance regularized level set evolution and its application to image segmentation”. In: *IEEE transactions on image processing* vol. 19, no. 12 (2010), pp. 3243–3254.
- [62] Izzo, R. et al. “The vascular modeling toolkit: a Python library for the analysis of tubular structures in medical images”. In: *Journal of Open Source Software* vol. 3, no. 25 (2018), p. 745.

- [63] Antiga, L. et al. “An image-based modeling framework for patient-specific computational hemodynamics”. In: *Medical & biological engineering & computing* vol. 46, no. 11 (2008), pp. 1097–1112.
- [64] Berg, P. et al. “Multiple aneurysms anatomy challenge 2018 (MATCH): phase I: segmentation”. In: *Cardiovascular engineering and technology* vol. 9, no. 4 (2018), pp. 565–581.
- [65] Oberkampf, W. L. and Trucano, T. G. “Verification and validation in computational fluid dynamics”. In: *Progress in aerospace sciences* vol. 38, no. 3 (2002), pp. 209–272.
- [66] Langtangen, H. P., Mardal, K.-A., and Winther, R. “Numerical methods for incompressible viscous flow”. In: *Advances in water Resources* vol. 25, no. 8-12 (2002), pp. 1125–1146.
- [67] Pope, S. B. and Pope, S. B. *Turbulent flows*. Cambridge university press, 2000.
- [68] Constantin, P. and Foias, C. *Navier-stokes equations*. University of Chicago Press, 2020.
- [69] Mortensen, M. and Valen-Sendstad, K. “Oasis: a high-level/high-performance open source Navier–Stokes solver”. In: *Computer physics communications* vol. 188 (2015), pp. 177–188.
- [70] Perot, J. B. “An analysis of the fractional step method”. In: *Journal of Computational Physics* vol. 108, no. 1 (1993), pp. 51–58.
- [71] Guermond, J.-L., Mineev, P., and Shen, J. “An overview of projection methods for incompressible flows”. In: *Computer methods in applied mechanics and engineering* vol. 195, no. 44-47 (2006), pp. 6011–6045.
- [72] Roache, P. J. *Verification and validation in computational science and engineering*. Vol. 895. Hermosa Albuquerque, NM, 1998.
- [73] Salari, K. and Knupp, P. *Code verification by the method of manufactured solutions*. Tech. rep. Sandia National Lab.(SNL-NM), Albuquerque, NM (United States); Sandia . . . , 2000.
- [74] Celik, I. B. et al. “Procedure for estimation and reporting of uncertainty due to discretization in CFD applications”. In: *Journal of fluids Engineering-Transactions of the ASME* vol. 130, no. 7 (2008).
- [75] Cosner, R. et al. “AIAA Committee on standards for computational fluid dynamics: status and plans”. In: *44th AIAA Aerospace Sciences Meeting and Exhibit*. 2006, p. 889.
- [76] Valen-Sendstad, K. and Steinman, D. “Mind the gap: impact of computational fluid dynamics solution strategy on prediction of intracranial aneurysm hemodynamics and rupture status indicators”. In: *American Journal of Neuroradiology* vol. 35, no. 3 (2014), pp. 536–543.



- [77] Khan, M., Valen-Sendstad, K, and Steinman, D. “Narrowing the expertise gap for predicting intracranial aneurysm hemodynamics: impact of solver numerics versus mesh and time-step resolution”. In: *American Journal of Neuroradiology* vol. 36, no. 7 (2015), pp. 1310–1316.
- [78] Robertson, A. M., Sequeira, A., and Owens, R. G. “Rheological models for blood”. In: *Cardiovascular mathematics*. Springer, 2009, pp. 211–241.
- [79] Evju, Ø., Valen-Sendstad, K., and Mardal, K.-A. “A study of wall shear stress in 12 aneurysms with respect to different viscosity models and flow conditions”. In: *Journal of biomechanics* vol. 46, no. 16 (2013), pp. 2802–2808.
- [80] Castro, M. A. et al. “Unsteady wall shear stress analysis from image-based computational fluid dynamic aneurysm models under Newtonian and Casson rheological models”. In: *Medical & biological engineering & computing* vol. 52, no. 10 (2014), pp. 827–839.
- [81] Hippelheuser, J. E. et al. “Realistic non-Newtonian viscosity modelling highlights hemodynamic differences between intracranial aneurysms with and without surface blebs”. In: *Journal of biomechanics* vol. 47, no. 15 (2014), pp. 3695–3703.
- [82] Khan, M., Steinman, D., and Valen-Sendstad, K. “Non-Newtonian versus numerical rheology: Practical impact of shear-thinning on the prediction of stable and unstable flows in intracranial aneurysms”. In: *International journal for numerical methods in biomedical engineering* vol. 33, no. 7 (2017), e2836.
- [83] Hodis, S et al. “Artery length sensitivity in patient-specific cerebral aneurysm simulations”. In: *American Journal of Neuroradiology* vol. 36, no. 4 (2015), pp. 737–743.
- [84] Jansen, I. et al. “Generalized versus patient-specific inflow boundary conditions in computational fluid dynamics simulations of cerebral aneurysmal hemodynamics”. In: *American Journal of Neuroradiology* vol. 35, no. 8 (2014), pp. 1543–1548.
- [85] Najafi, M. et al. “How patient-specific do internal carotid artery inflow rates need to be for computational fluid dynamics of cerebral aneurysms?” In: *Journal of NeuroInterventional Surgery* (2020).
- [86] Chnafa, C et al. “Errors in power-law estimations of inflow rates for intracranial aneurysm CFD”. In: *Journal of biomechanics* vol. 80 (2018), pp. 159–165.
- [87] Marzo, A. et al. “Computational hemodynamics in cerebral aneurysms: the effects of modeled versus measured boundary conditions”. In: *Annals of biomedical engineering* vol. 39, no. 2 (2011), pp. 884–896.
- [88] Berg, P. et al. “Multiple Aneurysms AnaTomy CHallenge 2018 (MATCH)—phase II: rupture risk assessment”. In: *International journal of computer assisted radiology and surgery* vol. 14, no. 10 (2019), pp. 1795–1804.

- [89] Hoi, Y. et al. “Characterization of volumetric flow rate waveforms at the carotid bifurcations of older adults”. In: *Physiological measurement* vol. 31, no. 3 (2010), p. 291.
- [90] Resnick, N. et al. “Platelet-derived growth factor B chain promoter contains a cis-acting fluid shear-stress-responsive element.” In: *Proceedings of the National Academy of Sciences* vol. 90, no. 10 (1993), pp. 4591–4595.
- [91] Valen-Sendstad, K. et al. “Real-world variability in the prediction of intracranial aneurysm wall shear stress: the 2015 international aneurysm CFD challenge”. In: *Cardiovascular engineering and technology* vol. 9, no. 4 (2018), pp. 544–564.
- [92] Ingebrigtsen, T. et al. “Bifurcation geometry and the presence of cerebral artery aneurysms”. In: *Journal of neurosurgery* vol. 101, no. 1 (2004), pp. 108–113.
- [93] Chnafa, C et al. “Better than nothing: a rational approach for minimizing the impact of outflow strategy on cerebrovascular simulations”. In: *American Journal of Neuroradiology* vol. 39, no. 2 (2018), pp. 337–343.
- [94] Murray, C. D. “The physiological principle of minimum work: I. The vascular system and the cost of blood volume”. In: *Proceedings of the National Academy of Sciences* vol. 12, no. 3 (1926), pp. 207–214.
- [95] Gin, R., Straatman, A. G., and Steinman, D. A. “A dual-pressure boundary condition for use in simulations of bifurcating conduits”. In: *J. Biomech. Eng.* vol. 124, no. 5 (2002), pp. 617–619.
- [96] He, X. and Ku, D. N. “Pulsatile flow in the human left coronary artery bifurcation: average conditions”. In: *Journal of biomechanical engineering* vol. 118, no. 1 (1996), pp. 74–82.
- [97] Kallmes, D. F. “Point: CFD—computational fluid dynamics or confounding factor dissemination”. In: *AJNR: American Journal of Neuroradiology* vol. 33, no. 3 (2012), p. 395.
- [98] Cebral, J. R. and Meng, H. *Counterpoint: realizing the clinical utility of computational fluid dynamics—closing the gap*. 2012.
- [99] Robertson, A. and Watton, P. *Computational fluid dynamics in aneurysm research: critical reflections, future directions*. 2012.
- [100] Strother, C. and Jiang, J. *Intracranial aneurysms, cancer, x-rays, and computational fluid dynamics*. 2012.
- [101] Xiang, J et al. “CFD: computational fluid dynamics or confounding factor dissemination? The role of hemodynamics in intracranial aneurysm rupture risk assessment”. In: *American Journal of Neuroradiology* vol. 35, no. 10 (2014), pp. 1849–1857.
- [102] Piccinelli, M. et al. “Geometry of the internal carotid artery and recurrent patterns in location, orientation, and rupture status of lateral aneurysms: an image-based computational study”. In: *Neurosurgery* vol. 68, no. 5 (2011), pp. 1270–1285.

- [103] Fiorella, D et al. “Regarding “Aneurysm rupture following treatment with flow-diverting stents: computational hemodynamics analysis of treatment””. In: *AJNR: American Journal of Neuroradiology* vol. 32, no. 5 (2011), E95.
- [104] Steinman, D. *Computational modeling and flow diverters: a teaching moment*. 2011.
- [105] Steinman, D. A. et al. “Variability of computational fluid dynamics solutions for pressure and flow in a giant aneurysm: the ASME 2012 Summer Bioengineering Conference CFD Challenge”. In: *Journal of biomechanical engineering* vol. 135, no. 2 (2013).
- [106] Hariharan, P. et al. “Multilaboratory particle image velocimetry analysis of the FDA benchmark nozzle model to support validation of computational fluid dynamics simulations”. In: *Journal of biomechanical engineering* vol. 133, no. 4 (2011).
- [107] Stewart, S. F. et al. “Assessment of CFD performance in simulations of an idealized medical device: results of FDA’s first computational interlaboratory study”. In: *Cardiovascular Engineering and Technology* vol. 3, no. 2 (2012), pp. 139–160.
- [108] Janiga, G. et al. “The Computational Fluid Dynamics Rupture Challenge 2013—Phase I: prediction of rupture status in intracranial aneurysms”. In: *American Journal of Neuroradiology* vol. 36, no. 3 (2015), pp. 530–536.
- [109] Berg, P. et al. “The computational fluid dynamics rupture challenge 2013—phase II: variability of hemodynamic simulations in two intracranial aneurysms”. In: *Journal of biomechanical engineering* vol. 137, no. 12 (2015).
- [110] Valen-Sendstad, K. et al. *Data for "The 2015 International Aneurysm CFD Challenge"*. <https://doi.org/10.6084/m9.figshare.6383516.v2>. 2018.
- [111] Khan, M. et al. “On the prevalence of flow instabilities from high-fidelity computational fluid dynamics of intracranial bifurcation aneurysms”. In: *Journal of Biomechanics* vol. 127 (2021), p. 110683.
- [112] Frosen, J. et al. “Remodeling of saccular cerebral artery aneurysm wall is associated with rupture: histological analysis of 24 unruptured and 42 ruptured cases”. In: *Stroke* vol. 35, no. 10 (2004), pp. 2287–2293.
- [113] Kataoka, K. et al. “Structural fragility and inflammatory response of ruptured cerebral aneurysms: a comparative study between ruptured and unruptured cerebral aneurysms”. In: *Stroke* vol. 30, no. 7 (1999), pp. 1396–1401.
- [114] Baek, H., Jayaraman, M. V., and Karniadakis, G. E. “Wall shear stress and pressure distribution on aneurysms and infundibulae in the posterior communicating artery bifurcation”. In: *Annals of biomedical engineering* vol. 37, no. 12 (2009), pp. 2469–2487.

- [115] Shimogonya, Y. et al. “Can temporal fluctuation in spatial wall shear stress gradient initiate a cerebral aneurysm? A proposed novel hemodynamic index, the gradient oscillatory number (GON)”. In: *Journal of biomechanics* vol. 42, no. 4 (2009), pp. 550–554.
- [116] Singh, P. K. et al. “Effects of smoking and hypertension on wall shear stress and oscillatory shear index at the site of intracranial aneurysm formation”. In: *Clinical neurology and neurosurgery* vol. 112, no. 4 (2010), pp. 306–313.
- [117] Lauric, A. et al. “Curvature effect on hemodynamic conditions at the inner bend of the carotid siphon and its relation to aneurysm formation”. In: *Journal of biomechanics* vol. 47, no. 12 (2014), pp. 3018–3027.
- [118] Geers, A. et al. “Wall shear stress at the initiation site of cerebral aneurysms”. In: *Biomechanics and modeling in mechanobiology* vol. 16, no. 1 (2017), pp. 97–115.
- [119] Karmonik, C. et al. “A technique for improved quantitative characterization of intracranial aneurysms”. In: *American journal of neuroradiology* vol. 25, no. 7 (2004), pp. 1158–1161.
- [120] Ford, M. et al. “An objective approach to digital removal of saccular aneurysms: technique and applications”. In: *The British journal of radiology* vol. 82, no. special\_issue\_1 (2009), S55–S61.
- [121] Chen, H. et al. “Investigating the influence of haemodynamic stimuli on intracranial aneurysm inception”. In: *Annals of biomedical engineering* vol. 41, no. 7 (2013), pp. 1492–1504.
- [122] Sforza, D. et al. “Effects of perianeurysmal environment during the growth of cerebral aneurysms: a case study”. In: *American Journal of Neuroradiology* vol. 33, no. 6 (2012), pp. 1115–1120.
- [123] Ho, A. L. et al. “Intrinsic, transitional, and extrinsic morphological factors associated with rupture of intracranial aneurysms”. In: *Neurosurgery* vol. 77, no. 3 (2015), pp. 433–442.
- [124] Schimansky, S. et al. “Extradural internal carotid artery caliber dysregulation is associated with cerebral aneurysms”. In: *Stroke* vol. 44, no. 12 (2013), pp. 3561–3564.
- [125] Lauric, A., Hippelheuser, J. E., and Malek, A. M. “Induction of aneurysmogenic high positive wall shear stress gradient by wide angle at cerebral bifurcations, independent of flow rate”. In: *Journal of Neurosurgery* vol. 131, no. 2 (2018), pp. 442–452.
- [126] Lauric, A. et al. “Proximal parent vessel tapering is associated with aneurysm at the middle cerebral artery bifurcation”. In: *Neurosurgery* vol. 84, no. 5 (2019), pp. 1082–1089.
- [127] Collaboration, O. S. et al. “Estimating the reproducibility of psychological science”. In: *Science* vol. 349, no. 6251 (2015).

- 
- [128] Soto, C. J. “How replicable are links between personality traits and consequential life outcomes? The life outcomes of personality replication project”. In: *Psychological Science* vol. 30, no. 5 (2019), pp. 711–727.
- [129] Klein, R. A. et al. “Many Labs 2: Investigating variation in replicability across samples and settings”. In: *Advances in Methods and Practices in Psychological Science* vol. 1, no. 4 (2018), pp. 443–490.
- [130] Sciences, E. National Academies of, Medicine, et al. “Reproducibility and replicability in science”. In: (2019).
- [131] Medical Sciences, A. of. “Reproducibility and reliability of biomedical research: improving research practice”. In: *Symposium report*. 2015.
- [132] Errington, T. M. et al. “Reproducibility in cancer biology: challenges for assessing replicability in preclinical cancer biology”. In: *Elife* vol. 10 (2021), e67995.
- [133] Baker, M. “Reproducibility crisis”. In: *Nature* vol. 533, no. 26 (2016), pp. 353–66.
- [134] Bergersen, A. W. ‘Method and results reproducibility/information’ in medical imaged based CFD. <https://doi.org/10.6084/m9.figshare.13300061>.
- [135] *VaMPy - Vascular Modeling Pipeline*. <https://github.com/KVSlab/VaMPy>. Accessed: 2022-02-03.



# Papers





- I. **The FDA nozzle benchmark: "In theory there is no difference between theory and practice, but in practice there is"**





# The FDA nozzle benchmark: “In theory there is no difference between theory and practice, but in practice there is”

Aslak W. Bergersen<sup>1</sup> | Mikael Mortensen<sup>2</sup> | Kristian Valen-Sendstad<sup>1</sup>

<sup>1</sup>Department of Computational Physiology, Simula Research Laboratory AS, Fornebu, Norway

<sup>2</sup>Department of Mathematics, University of Oslo Mathematics and Natural Sciences, Oslo, Norway

## Correspondence

Kristian Valen-Sendstad, Department of Computational Physiology, Simula Research Laboratory AS, Fornebu, Norway.  
Email: kvs@simula.no

## Funding information

Center for Biomedical Computing, Grant/Award Number: 179578; Cardiological Innovation, and SIMMIS, Grant/Award Number: 262827; University of Oslo IT-department, Grant/Award Number: nn9316k

## Abstract

The utility of flow simulations relies on the robustness of computational fluid dynamics (CFD) solvers and reproducibility of results. The aim of this study was to validate the Oasis CFD solver against in vitro experimental measurements of jet breakdown location from the FDA nozzle benchmark at Reynolds number 3500, which is in the particularly challenging transitional regime. Simulations were performed on meshes consisting of 5, 10, 17, and 28 million (M) tetrahedra, with  $\Delta t = 10^{-5}$  seconds. The 5M and 10M simulation jets broke down in reasonable agreement with the experiments. However, the 17M and 28M simulation jets broke down further downstream. But which of our simulations are “correct”? From a theoretical point of view, they are all wrong because the jet should not break down in the absence of disturbances. The geometry is axisymmetric with no geometrical features that can generate angular velocities. A stable flow was supported by linear stability analysis. From a physical point of view, a finite amount of “noise” will always be present in experiments, which lowers transition point. To replicate noise numerically, we prescribed minor random angular velocities (approximately 0.31%), much smaller than the reported flow asymmetry (approximately 3%) and model accuracy (approximately 1%), at the inlet of the 17M simulation, which shifted the jet breakdown location closer to the measurements. Hence, the high-resolution simulations and “noise” experiment can potentially explain discrepancies in transition between sometimes “sterile” CFD and inherently noisy “ground truth” experiments. Thus, we have shown that numerical simulations can agree with experiments, but for the wrong reasons.

## KEYWORDS

computational fluid dynamics, FDA nozzle benchmark, noise, transitional flow, turbulence, validation

## 1 | INTRODUCTION

Cardiovascular diseases are burdening health care systems, and costs are expected to rise in the years to come.<sup>1</sup> Systemic risk factors have been associated with higher prevalence of cardiovascular diseases; however, eg, aneurysms<sup>2</sup> and atherosclerotic plaques<sup>3</sup> are focally distributed, highlighting the importance of blood flow-induced wall shear stress.<sup>4,5</sup> Medical image-based computational fluid dynamics (CFD)<sup>6</sup> has been extensively used retrospectively on large image

databases to correlate abnormal stresses with disease initiation and outcome,<sup>7,8</sup> with the ultimate aim of using CFD as a prospective clinical tool. However, the efficacy of CFD depends on the robustness of the methods and reproducibility of results. The US Food and Drug Administration (FDA) therefore devised a benchmark of a “generic medical device”<sup>9</sup> where the goal was to assess the state-of-the-art of CFD in biomechanics, comparing CFD solutions to in vitro experiments, and to provide reference solutions for future validation of CFD solvers.<sup>10</sup>

The interlaboratory comparison showed a relatively wide variability in the predicted breakdown location of the (possibly) turbulent jet.<sup>11</sup> Largest discrepancies were reported in the transitional flow regime, in contrast to the fully laminar and turbulent flows. Interestingly, none of the CFD benchmark participants obtained results in agreement with the in vitro measurements for Reynolds number ( $Re$ ) 3500, although good agreement and excellent CFD results have been reported by multiple authors retrospectively.<sup>12–15</sup> The FDA nozzle benchmark model remains highly relevant for biomedical problems and our aim was to further validate the open-source CFD solver *Oasis*<sup>16</sup> that we have extensively used to study turbulent-like cardiovascular flows.<sup>17–23</sup> We focus on the flow at  $Re = 3500$ , which is in the particularly challenging transitional flow regime, for which the in vitro experiments displayed the least variability.

## 2 | METHODOLOGY

A sketch of the idealized medical device used in the FDA nozzle benchmark is shown in Figure 1. The inlet pipe in the in vitro experimental setup was 2.661 m long with an outlet section of 1.146 m. The computational domain was chosen to be shorter than the in vitro one, in total 0.320 m long, from  $z = -0.120$  m to  $z = 0.200$  m relative to the sudden expansion located at  $z = 0$  m ( $x, y = 0$  m). To ease reproducibility of our results, unstructured volumetric meshes were created with constant node spacing and four boundary layers using ICEM-CFD (ANSYS Inc, Canonsburg, PA, USA). In total 4 meshes were created consisting of 5, 10, 17, and 28 million (M) tetrahedron cells, referred to as 5M, 10M, 17M, and 28M, respectively. The characteristic node spacing for these meshes were  $3.5 \cdot 10^{-4}$ ,  $2.8 \cdot 10^{-4}$ ,  $2.4 \cdot 10^{-4}$ , and  $2.0 \cdot 10^{-4}$  m. We specified a constant time step of  $\Delta t = 1 \cdot 10^{-5}$  seconds for all simulations, based on setting the maximum Courant number to 0.5, assuming a peak centerline velocity of 4 m/s and using the minimum cell length of the 28M mesh. The initial condition was set to zero for both velocity and pressure, and we specified a parabolic velocity profile at the inlet. The pressure was set to zero at the outlet, and we applied a no-slip condition at the walls. Simulations were performed using *Oasis*, where special care has been taken to ensure a kinetic-energy-preserving and minimally dissipative numerical solution. The solver and numerical implementation is described in detail elsewhere.<sup>16</sup> The instantaneous velocity,  $\mathbf{u}(\mathbf{x}, t)$ , was sampled at various points and cross sections along the  $z$ -axis, including at  $z = -0.016, 0, 0.04, 0.08, 0.12$ , and  $0.16$  m. Reynolds decomposition was used to separate the instantaneous velocity from the time averaged,  $\bar{\mathbf{u}}(\mathbf{x})$ , and the fluctuating,  $\mathbf{u}'(\mathbf{x}, t)$ , components, ie,  $\mathbf{u} = \bar{\mathbf{u}} + \mathbf{u}'$ . We also computed the turbulent kinetic energy (TKE) as  $k = \frac{1}{2}(\mathbf{u}' \cdot \mathbf{u}')$ , and power spectral density (PSD) of the fluctuating velocity magnitude,  $|\mathbf{u}'|$ , at various locations along the centerline. For the latter, we used Welch’s method<sup>24</sup> with eight segments, and a Hanning windowing function with 50% overlap.

## 3 | RESULTS

We focus first on time-averaged cross-sectional and centerline velocities sampled between  $t = 1.4 - 1.6$  seconds, when the jet breakdown locations had stabilized, shown in Figure 2, left and right, respectively. Relative to the 5M simulation, the 10M simulation appears to converge towards the in vitro measurements. However, the 17M and 28M simulations broke down approximately 10 and 15 inlet diameters further downstream.

To investigate the apparent discrepancies in time-averaged jet breakdown location, Figure 3 (top) shows the instantaneous velocity fields for the four different mesh densities at  $t = 1.0$  second. Figure 3 (bottom) shows the instantaneous

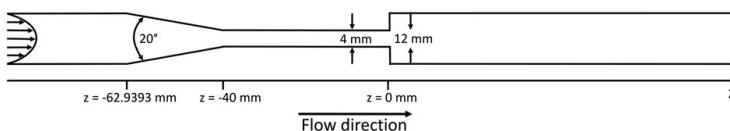


**FIGURE 1** Sketch of the generic medical device, consisting of a nozzle with a conical change in diameter at one end of the throat, and a sudden change at the other

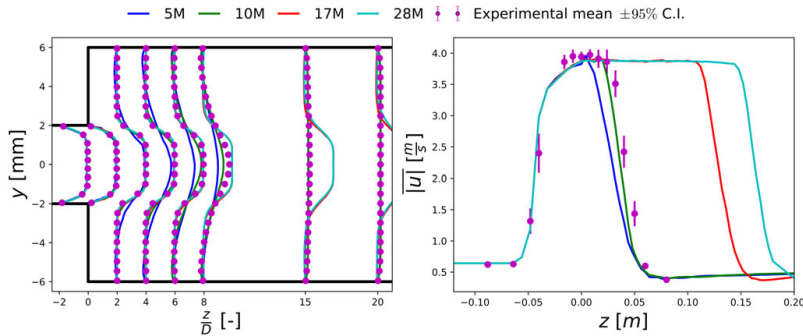


**FIGURE 2** Time-averaged cross-sectional (left) and centerline (right) velocities obtained from the simulations at mesh sizes of 5M to 28M compared against in vitro experimental measurements. The ordinate in the left figure is normalized with respect to the diameter. The 5M and 10M simulation jets broke down in reasonable agreement with the experiments, whereas the 17M and 28M simulation jets broke down further downstream

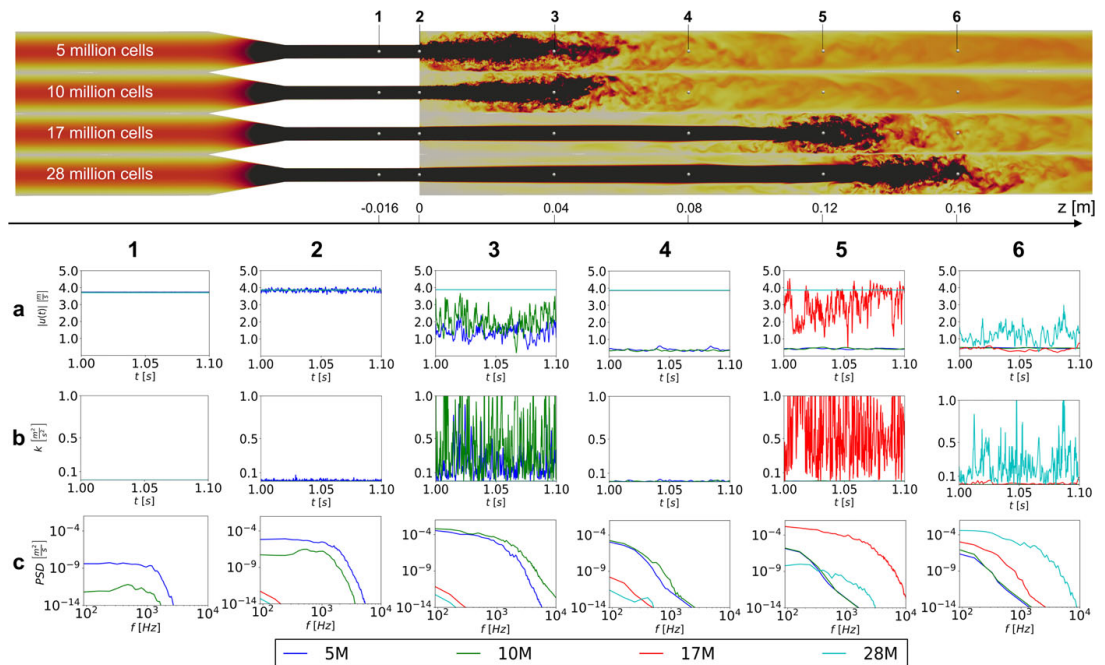


**FIGURE 3** Top: Instantaneous velocity fields in a slice of the computational domain at  $t = 1.0$  second for the four different meshes. Bottom subplot: a) velocity traces, b) turbulent kinetic energy, and c) power spectral density of  $|u'|$ , sampled at the point locations indicated in the top figure

velocity magnitude, TKE, and PSD of the fluctuating velocity component for  $t = 1.0 - 1.1$  seconds in subplots a, b, and c, respectively, where the prefix corresponds to the probe locations in Figure 3 (top). Focusing now on subplots 1a and 1b, just upstream of the sudden expansion, there are no apparent velocity fluctuations. In contrast, at the sudden expansion, the fluctuations are clearly visible in plots 2a and 2b for the 5M and 10M simulations. This is also reflected by 2c, displaying fluctuations that contained additional energy, compared with 1c. However, the 17M and 28M simulations only contained low energy and low frequency flow instabilities. Further downstream, in plot 3a, the centerline velocity magnitude is reduced for the 5M and 10M simulations, and the  $|u'|$  has more energy in the higher frequencies in 3b, also

reflected by 3c. On the other hand, the 17M and 28M simulations are at location 3 practically identical to location 2. Further downstream, in plots 4a and 4b, both the 5M and 10M simulations developed similarly; the centerline velocity was relatively stable and only contained low amplitude and low frequency fluctuations. Subplot 4c reveals that flow instabilities in the 17M and 28M simulations grew, whereas the 5M and 10M flows were further dissipated. Approximately 10 diameters downstream of the sudden expansion, the 17M jet broke down as reflected by plots 5a to 5c. The energy spectra in plot 5c shows that the 28M simulation instabilities increased relative to location 4. In the last column of Figure 3, we can see that the centerline velocity of 5M, 10M, and 17M had close to the same magnitude, although 17M exhibit larger fluctuations. Furthermore, the jet in the 28M simulation had at this location broken down, as shown in plots 6a to 6c, whereas the flow in the 17M simulation had lost much of its high frequency components, as reflected by the PSD, indicative of further flow stabilization.

## 4 | DISCUSSION

The aim of this study was to validate the CFD solver *Oasis* against the in vitro measurements presented in the FDA nozzle benchmark. However, our results would seem to suggest that we have refuted the validity of our solver instead. But, before concluding that our solver is erroneous, let us consider a few aspects of the FDA nozzle benchmark and our approach. From a purely *computational point of view*, we would intuitively put more faith in the more resolved simulations, but the 5M and 10M simulation results were closer to the in vitro experimental measurements. This apparent contradiction led to the obvious question: which, if any, of our simulations are “correct”?

The consistent correlation between increased mesh resolution and jet breakdown location reminded us that the geometry is fully axisymmetric, so there should not be any 3D structures as observed in the abrupt jet breakdown. Said in other words, all our results are actually wrong. From a purely *theoretical point of view*, it is established that fully axisymmetric flows are known to not transition to turbulence, because there are no geometrical features that can introduce asymmetries. This is conceptually easy to comprehend by rewriting the Navier-Stokes equations into cylindrical coordinates. With the prescribed boundary conditions, the solution becomes independent of the angular direction and thereby just a collection of identical 2D planes. This has also been shown computationally that fully axisymmetric flows only break down to turbulence if the numerical solution is perturbed, eg, numerically<sup>25</sup> or geometrically.<sup>26,27</sup>

To investigate our results from an *analytical point of view*, we used linear stability analysis. In short, we decomposed the flow variables into the sum of a stable laminar base flow and a perturbation  $(\mathbf{u}, p) = (\mathbf{U}, P) + (\mathbf{u}', p')$ . The decomposition was inserted into the Navier-Stokes equations that were linearized after eliminating the pressure using the continuity condition.<sup>28</sup> We then obtained a linear operator equation for the evolution of the velocity perturbation

$$\frac{\partial \mathbf{u}'}{\partial t} = L(\mathbf{u}'), \quad (1)$$

where  $L$  is the linearized operator. The eigensystem of  $L$  is given by the eigenvalues  $\lambda_\alpha$  and eigenmodes  $\tilde{\mathbf{u}}'_\alpha$  as  $L\tilde{\mathbf{u}}'_\alpha = \lambda_\alpha \tilde{\mathbf{u}}'_\alpha$  (no summation on  $\alpha$ ). Given the eigensystem, the perturbed velocity vector may be obtained as

$$\mathbf{u}' = \sum_{\alpha=0}^{\infty} \exp(\lambda_\alpha t) \tilde{\mathbf{u}}'_\alpha. \quad (2)$$

A linear stability analysis amounts to computing the leading eigenvalues of the linearized Navier-Stokes operator  $L$ , as well as the corresponding eigenmodes  $\tilde{\mathbf{u}}'_\alpha$ , representing the perturbations to the laminar base flow. The growth rate of the perturbations (ie, the eigenvalues) are indicative of whether or not the flow is linearly stable; a negative eigenvalue represents a stable mode and a positive eigenvalue represents an unstable mode. If perturbing a numerical simulation with an unstable mode, and allowed to grow sufficiently in time, the mode will eventually trigger turbulence in the numerical simulations.<sup>25</sup>

It is evident that the flow regime upstream of the sudden expansion ( $z = 0$ ) will have a profound effect on the flow in the main pipe and jet breakdown location. We therefore split the domain in Figure 1 at  $z = 0$  m and computed two analyses, one upstream and one downstream of the sudden expansion, using the open source spectral element code Semtex<sup>29</sup> together with its accompanying Dog<sup>28</sup> for the linear stability analyses.

The analyses revealed that all eigenvalues for the flow in the upstream section were negative, indicative of a stable and laminar flow. In contrast, the outlet section contained positive eigenvalues and thus unstable eigenmodes, which

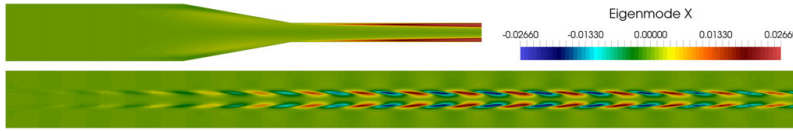


**FIGURE 4** The computational domain is split into two parts, the throat section (upper) and sudden expansion (lower). For the throat section, the eigenvalue is  $-0.0382 + 0.0115i$ , and is thus stable, whereas the sudden expansion has an unstable eigenvalue of  $0.218 + 1.45i$ . Showing only the x-component of the eigenmode allows us to observe the oscillating nature of the eigenmode corresponding to the unstable eigenvalue

are visualized in Figure 4. Of note from the analyses is: First, the flow in the throat section should be laminar, and second, linear stability analysis supports the experimental observations that potential instabilities should grow and cause jet breakdown. The predicted laminar flow in the throat section is of utmost importance to explain our numerical results, since flow instabilities at the sudden expansion dictate jet breakdown location. That being said, linear stability theory cannot provide definite proof and is often conservative compared to in vitro experiments, not to mention the unphysical prediction of laminar pipe flow even at infinite  $Re$ .<sup>30</sup> Alternatively, quoting Carstensen et al.,<sup>31</sup> “when comparing experimental values for transitional and critical Reynolds number obtained through theoretical stability analysis (i.e. when linear disturbances start to grow), any correspondence in the values is usually just a coincidence.”

Since linear stability analysis predicted a laminar and stable flow, our natural follow-up question was “what caused asymmetrical flow components in our simulations?” To understand our results from a *numerical point of view*, the first clue was found in subplot 1c of Figure 3. We observed that the two coarsest simulations exhibit low amplitude, but high frequency, “noise” in the approximately 0- to 3000-Hz range, upstream of the sudden expansion, that were absent in the two finer ones. It is rather intuitive that the Cartesian tetrahedral mesh is the source of the noise, as all other simulation parameters were kept fixed. By approximating a cylindrical geometry with an increasing number of linear elements, the geometry is more accurately represented, and the numerical accuracy is improved. The former is rather intuitive and the latter is elementary knowledge,<sup>32</sup> but the mesh quality is generally also improved.

To isolate and investigate the effect of mesh quality on numerical accuracy, and hence accurately predict transitional flows, we compared numerical solutions on meshes with optimal versus suboptimal aspect ratio, respectively. We chose the 3D Taylor-Green vortex benchmark<sup>33</sup> where the boundary conditions are periodic on the domain  $\Omega \in [-2\pi, 2\pi]^3$ , which makes the problem conceptually unbounded and independent of geometrical features. The initial conditions are analytical vortices<sup>34</sup> that break down to consecutively smaller ones until dissipation dominates at the smaller scales. The evolution of the vortices is symmetrical and deterministic, but the flow has an energy cascade and other features commonly associated with truly turbulent flows.<sup>35</sup> We set  $Re = 1000$ ,  $\Delta t = 1 \cdot 10^{-3}$  seconds, and computed the solution on meshes consisting of  $6 \cdot 32^3$ ,  $6 \cdot 64^3$ , and  $6 \cdot 128^3$  tetrahedral cells, where the interior node locations were perturbed by a vector drawn from a normal distribution with standard deviation of 18% and 36% of the tetrahedron node spacing, respectively, reflecting mesh quality observed in the 28M and 10M element meshes.

The results of our simple and controlled numerical experiment is presented in Figure 5, showing temporal evolution of the rate of dissipation,  $\epsilon = -\partial k / \partial t$ . The solutions on the three unperturbed meshes are shown in Figure 5A, where we can observe that the numerical solutions evolves equally up until  $t \sim 3$  seconds on all meshes. However, after  $t \geq 3$  seconds, the coarse mesh resolution leads to a premature elevation of  $\epsilon$ , as vortices breaking down below the mesh resolution are not dissipated. Figure 5B-D shows a systematic shift in point of transition caused by flow asymmetries introduced by the perturbed node locations. These effects are more pronounced on the coarse meshes that are underresolved, and the flow reaches a complex and chaotic state sooner. We can also observe that distorted elements have less of an effect on the better resolved mesh, as, eg, 18% distortion is equivalent to 36% on the  $6 \cdot 64^3$  versus  $6 \cdot 128^3$  cell mesh, respectively. We here observe in isolation the same effects as in our FDA nozzle benchmark results, namely, that transition occurs earlier on the lower quality and coarser meshes, but here in the absence of geometrical features.

From a *physical point of view*, it is difficult to completely exclude minor imperfections in in vitro laboratory experiments, stemming from either minor pulsations in the flow rate caused by a pump, deflected pipes, transitions between pipes, minor surface irregularities in the geometry etc, here, collectively referred to as *experimental noise*. That experimental noise might affect the critical  $Re$ , ie, for which  $Re$  the flow deviates from a laminar regime, was reported by Reynolds already in 1883.<sup>36</sup> Reynolds observed a turbulent flow regime down to  $Re \sim 2000$ , but also laminar flow up to  $Re \sim 13000$ , solely dependent on the level of experimental noise. On the high side, conceptually similar in vitro experiments have

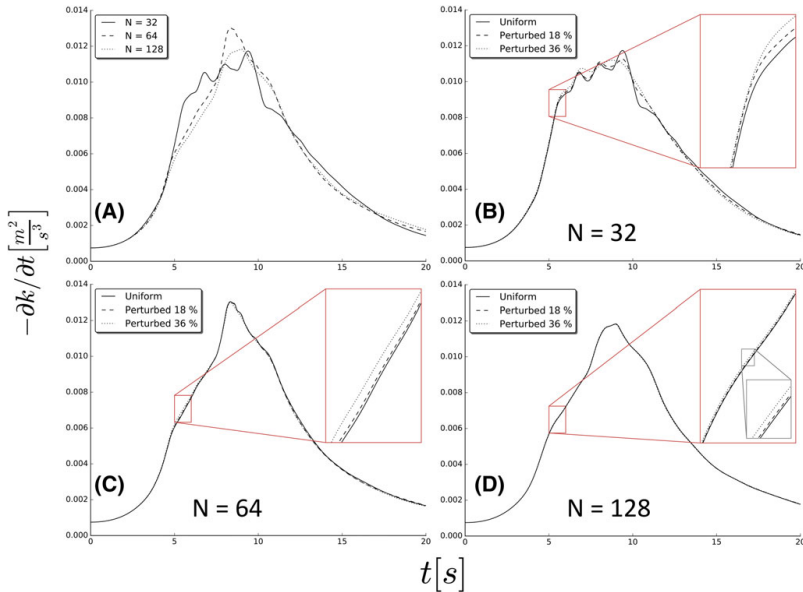


**FIGURE 5** A, Rate of dissipation of the kinetic energy for the 3D Taylor-Green vortex benchmark on three different meshes consisting of  $6 \cdot 32^3$ ,  $6 \cdot 64^3$ , and  $6 \cdot 128^3$  cells, respectively. B-D, Effects of interior node location shifted randomly by 0%, 18%, and 36%, on the  $6 \cdot 32^3$ ,  $6 \cdot 64^3$ , and  $6 \cdot 128^3$  cell meshes, respectively

shown laminar pipe flow for  $Re$  up to 100 000 by taking extreme care to reduce asymmetries and noise.<sup>37</sup> On the low side, flow instabilities due to asymmetries as small as model manufacturing precision has been studied in both idealized<sup>38,39</sup> and patient-specific<sup>40</sup> stenosed artery models. For comparison, the physical model uncertainty in the FDA nozzle benchmark was reported to be within 1%, flow rate fluctuation less than 1%, and that the particle-image-velocimetry-measured time-averaged flow asymmetry was within 3%<sup>10</sup> at the entrance of the nozzle for  $Re = 3500$ . Furthermore, using laser Doppler velocimetry with the same experimental setup and standard operating procedure as in Hariharan et al.,<sup>10</sup> Taylor et al reported that small perturbations were present in the throat section in vitro at  $Re = 2000$ .<sup>41</sup>

As noted in the previous paragraph, determining the point of transition can be very challenging. Therefore, the in vitro results are excellent from an *experimental point of view*, with good interlaboratory agreement. However, experiments intended for validation of numerical solvers have to provide measured, not idealized, boundary conditions of the experiment to ensure “numerical reproducibility.”<sup>42</sup> In the context of the FDA nozzle benchmark, modelers might not have been provided with precise enough information to replicate the observed deviations from a laminar profile and therefore simulated an idealized version of the experiment instead, which might not have occurred experimentally. It is fully possible that the latter can explain the observed differences between the in vitro and in silico results, also supported by Zmijanovic et al.<sup>15</sup>

One way to numerically mimic potential experimental noise is to perturb the numerical simulation with a finite level of noise to break the aforementioned symmetry. We therefore added white noise at the inlet of the 17M element mesh, which was the computationally least expensive mesh where the simulation results showed discrepancies with in vitro measurements. More specifically, we prescribed random velocity components in the angular direction only, drawn from a normal distribution with mean of zero, and a standard deviation of 0.001 m/s. Relative to the FDA nozzle benchmark, this standard deviation was 0.31% of the cross-sectional mean axial inlet velocity at  $Re = 3500$ , and one order of magnitude less than the experimentally measured left/right time-averaged flow asymmetry. The interesting feature is whether this noise decays or grows, ie, if the noise is over or under the critical level of noise.<sup>43</sup> We therefore performed simulations of flows in the laminar ( $Re = 500$ ), transitional ( $Re = 3500$ ), and turbulent ( $Re = 6500$ ) regimes, both with and without noise, referred to as noise and no-noise, respectively.

Figure 6 shows the time-averaged centerline velocities for  $Re = 500$ , 3500, and 6500, with noise and no-noise compared against the in vitro experiment measurements.<sup>10</sup> We observe that both the  $Re = 500$  and  $Re = 6500$  flow simulations



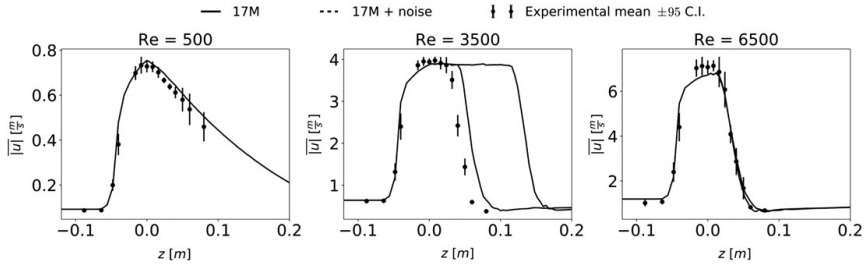


**FIGURE 6** Effects of adding noise at the inlet, with no-noise, noise, and in vitro measurements in solid lines, dotted lines, and bars, respectively, for  $Re = 500, 3500, 6500$  left to right. The  $Re = 500$  and  $Re = 6500$  centerline velocities are unaffected by noise, but for  $Re = 3500$ , jet breakdown location shifted approximately 9 diameters upstream, closer to the in vitro experimental measurements

were unaffected by noise, as the noise/no-noise results are indistinguishable and show excellent agreement with the experiments. On the other hand, the  $Re = 3500$  flow results were “strongly” affected by noise, as the jet breakdown location shifted approximately 9 diameters upstream. Comparing against in vitro and in silico pipe flow experiments, the changes in  $Re = 3500$  simulation were expected, since critical threshold of noise typically scales with  $\frac{1}{Re}$ .<sup>44</sup> Therefore, neither of the “extreme”  $Re$  simulations should be affected by noise, only those in the transitional regime. Admittedly, the  $Re = 3500$  simulation with noise did not show a perfect agreement with the in vitro measurements. In contrast to the laboratory experiments, the random noise we added did not a priori satisfy the Navier-Stokes equations and was only introduced at one location. Furthermore, the noise was largely dissipated before reaching the sudden expansion for  $Re = 3500$ , consistent with the linear stability analysis results. However, this nonexhaustive ad hoc numerical experiment was only intended as a proof of concept that noise might lower the critical Reynolds number for transitional flows. Further investigation of how different types of noise can affect transition is a scientifically important and interesting topic, but beyond the scope of this study, cf Hof<sup>44</sup> et al and Peixinho and Mullin.<sup>45</sup>

Quoting Oberkampf and Roy, “knowing the correct answer beforehand is extremely seductive, even to a saint.”<sup>42</sup> In this context, and relative to other groups, we are aware of a handful of studies where the authors, like us, had access to the in vitro “ground truth” experimental results prior to simulating the flows, which allows for tweaking and tuning of parameters to match the experiments. Solution strategies include direct numerical simulation,<sup>12</sup> large eddy simulation (LES),<sup>13–15</sup> or a dynamic hybrid Reynolds-averaged Navier-Stokes (RANS)/LES model.<sup>46</sup> The fact that RANS<sup>47</sup> and LES<sup>48</sup> models are generally too dissipative, and not suitable to studying flows in the transitional regime, is beyond the point; all studies where the authors were nonblinded to the in vitro results showed reasonable agreement with the measurements.

Passerini et al<sup>12</sup> used a locally refined mesh with approximately 3M cells and quadratic Taylor-Hood elements ( $\mathbb{P}_2 - \mathbb{P}_1$ ), which is equivalent of 24M linear ( $\mathbb{P}_1 - \mathbb{P}_1$ ) elements. Passerini et al assessed the spatially varying relative mesh resolution computing  $I^+$ <sup>49</sup> and reported  $I^+_{max} = 4$ , indicative of a spatially well-resolved simulation. We also ran our 10M element simulation using quadratic Taylor-Hood elements ( $\mathbb{P}_2 - \mathbb{P}_1$ ), which is equivalent of 80M linear ( $\mathbb{P}_1 - \mathbb{P}_1$ ) elements at a time step size of  $\Delta t = 5 \cdot 10^{-6}$  seconds.<sup>50</sup> The jet breakdown location shifted continuously downstream of the sudden expansion and eventually reached the end of the computational domain, which caused backflow at the outlet and a diverged numerical solution. The latter is well known<sup>40,51</sup>; however, Passerini et al still reported a lower  $I^+_{max}$  compared with our  $I^+_{max} = 11.0$  ( $I^+_{average} = 1.3$ ) obtained on the 80M linear ( $\mathbb{P}_1 - \mathbb{P}_1$ ) element equivalent mesh with constant node spacing. This comparison may indicate that the mesh used by Passerini et al was rather refined in the high shear rate regions, and consequently equally coarser elsewhere. This might suggest that numerical noise might have been introduced by a locally coarse mesh, which resulted in overall good agreement with the experimental measurements. That being said, a head-to-head comparison is not easy due to mesh reproducibility issues.

Delorme et al<sup>14</sup> performed a refinement study for  $Re = 2000$ , where the most resolved mesh had the equivalent to approximately 42M linear elements. Although the mesh resolution does not differ much from ours, the results still do. That being said, it is difficult searching for meaningful sources of discrepancies as they used a structured staggered mesh, the finite volume method, and an LES model, all different from our modeling choices.

Zmijanovic et al<sup>15</sup> made an excellent point assessing the numerical robustness of the nozzle benchmark by investigating the sensitivity of spatial and temporal resolution, temporal discretization schemes, and turbulent intensity (TI) injection on jet breakdown location. Regarding the latter, TI injection was found to produce robust numerical results relative to the experiments, regardless of intensity. Focusing now exclusively on simulations without TI injection, Zmijanovic et al

also compared the jet breakdown location between an explicit fourth order Runge-Kutta (RK4) scheme, and a linear combination of a two-step time-explicit Taylor-Galerkin scheme (20 %) and the RK4 scheme (80 %), referred to as TFV4A, for various time step sizes with a 5M and 15M-element mesh. When improving the temporal resolution, they reported no or a downstream shift for RK4, versus an upstream shift for TFV4A, relative to the in vitro experiments. In their spatial refinement study, Zmijanovic et al reported an excellent agreement with the in vitro experiments for the 50M-element simulation, although accidental, whereas an upstream and downstream shift for the 5M and 15M-element simulations, respectively, using the TFV4A scheme. In contrast to our results, Zmijanovic et al report an inconsistent effect of the spatial and temporal resolution on jet breakdown location, and it is therefore unclear what breaks the axis symmetry in their simulations without TI injection. That being said, our studies are largely complimentary, both investigating the impact of numerical noise and solver settings on jet breakdown location.

A teaching moment from the current study may be that our high resolution simulations and numerical noise experiments can potentially shed light on the observed discrepancies in transition to turbulence between sometimes “sterile” CFD and “ground truth” in vitro experiments that are inherently “noisy.”<sup>52</sup> Secondly, although symmetric models are convenient to manufacture, warnings about the use of such have been put forward as one is literally “dancing on the knife-edge of symmetry.”<sup>53</sup> Finally, our original aim was to validate our solver against in vitro measurements. As shown in Figure 6, we demonstrate excellent agreement with the measurement for the fully laminar and turbulent flow regimes. On the other hand, the transitional regime is surprisingly sensitive to minor perturbations, as discussed above. However, having provided new insight into the source of numerical noise, we would still not refute the validity of our solver in the transitional regime.

## 5 | CONCLUSIONS

We have performed CFD simulations of the FDA nozzle benchmark for various Reynolds numbers and mesh resolutions. The coarse simulation results showed an overall acceptable agreement with the experimental measurements, whereas the finer ones broke down much further downstream. The discrepancies were attributed to numerical noise introduced by mesh artifacts, which were more profound in the coarse meshes. We conclude that the jet in the FDA nozzle benchmark should in the absence of disturbances not transition to turbulence from a *theoretical point of view*, although from a *practical point of view*, the jet breaks down both in vitro and in silico, depending on the type and level of noise. We can conclude that the onset of transition remains challenging to predict, including how mesh artifacts affects the critical  $Re$  in simulations. Hence, our results can potentially shed light on the observed discrepancies in transition between CFD that can be sterile and in vitro “ground truth” experiments that are inherently noisy, or that “in theory there is no difference between theory and practice, but in practice there is.”<sup>54</sup> In other words, we have shown that numerical simulation results can agree with experiments, but for the wrong reasons.

## ACKNOWLEDGMENTS

The study was supported by The Research Council of Norway through a Centres of Excellence grant to the Center for Biomedical Computing at Simula Research Laboratory, project number 179578. This work was also carried out as a part of the Centre for Cardiological Innovation, and SIMMIS, project number 262827, funded by the Research Council of Norway. Simulations were performed on the Abel Cluster, owned by the University of Oslo and the Norwegian metacenter for High Performance Computing (NOTUR) and operated by the Department for Research Computing at USIT, the University of Oslo IT-department, grant number nn9316k.

## ORCID

Mikael Mortensen  <http://orcid.org/0000-0002-3293-7573>

Kristian Valen-Sendstad  <http://orcid.org/0000-0002-2907-0171>

## REFERENCES

1. Murray CJL, Lopez AD. Alternative projections of mortality and disability by cause 1990-2020: global burden of disease study. *The Lancet*. 1997;349(9064):1498-1504.
2. Weir B. Unruptured intracranial aneurysms: a review. *J Neurosurg*. 2002;96(1):3-42.

3. Lee S-W, Antiga L, Spence JD, Steinman DA. Geometry of the carotid bifurcation predicts its exposure to disturbed flow. *Stroke*. 2008;39(8):2341-2347.
4. Malek AM, Alper SL, Izumo S. Hemodynamic shear stress and its role in atherosclerosis. *JAMA*. 1999;282(21):2035-2042.
5. Morbiducci U, Kok AM, Kwak BR, et al. Atherosclerosis at arterial bifurcations: evidence for the role of haemodynamics and geometry. *Thromb Haemost*. 2016;115(3):484-492.
6. Taylor CA, Steinman DA. Image-based modeling of blood flow and vessel wall dynamics: applications, methods and future directions. *Ann Biomed Eng*. 2010;38(3):1188-203.
7. Chen H, Selimovic A, Thompson H, et al. Investigating the influence of haemodynamic stimuli on intracranial aneurysm inception. *Ann Biomed Eng*. 2013;41:1492-1504.
8. Cebal JR, Raschi M. Suggested connections between risk factors of intracranial aneurysms: a review. *Ann Biomed Eng*. 2013;41(7):1366-1383.
9. Website. U.S. Food and Drug Administration. <https://fdacfd.nci.nih.gov>. Accessed June 20, 2018.
10. Hariharan P, Giarra M, Reddy V, et al. Multilaboratory particle image velocimetry analysis of the FDA benchmark nozzle model to support validation of computational fluid dynamics simulations. *J Biomed Eng*. 2011;133(4):041002.
11. Stewart SFC, Paterson EG, Burgreen GW, et al. Assessment of CFD performance in simulations of an idealized medical device: results of FDA's first computational interlaboratory study. *Cardiovasc Eng Technol*. 2012;3(2):139-160.
12. Passerini T, Quaini A, Villa U, Veneziani A, Canic S. Validation of an open source framework for the simulation of blood flow in rigid and deformable vessels. *Int J Numer Methods Biomed Eng*. 2013;29(11):1192-1213.
13. Janiga G. Large eddy simulation of the FDA benchmark nozzle for a Reynolds number of 6500. *Comput Biol Med*. 2014;47:113-119.
14. Delorme YT, Anupindi K, Frankel SH. Large eddy simulation of FDA's idealized medical device. *Cardiovasc Eng Technol*. 2013;4(4):392-407.
15. Zmijanovic V, Mendez S, Moureau V, Nicoud F. About the numerical robustness of biomedical benchmark cases: interlaboratory FDA's idealized medical device. *Int J Numer Methods Biomed Eng*. 2017;33(1).
16. Mortensen M, Valen-Sendstad K. Oasis: a high-level/high-performance open source Navier-Stokes solver. *Comput Phys Commun*. 2015;188:177-188.
17. Valen-Sendstad K, Mardal K-A, Steinman DA. High-resolution CFD detects high-frequency velocity fluctuations in bifurcation, but not sidewall, aneurysms. *J Biomech*. 2013;46(2):402-407.
18. Valen-Sendstad K, Steinman DA. Mind the gap: impact of computational fluid dynamics solution strategy on prediction of intracranial aneurysm hemodynamics and rupture status indicators. *Am J Neuroradiol*. 2014;35(3):536-543.
19. Valen-Sendstad K, Piccinelli M, Steinman DA. High-resolution computational fluid dynamics detects flow instabilities in the carotid siphon: implications for aneurysm initiation and rupture? *J Biomech*. 2014;47(12):3210-3216.
20. Khan MO, Valen-Sendstad K, Steinman DA. Narrowing the expertise gap for predicting intracranial aneurysm hemodynamics: impact of solver numerics versus mesh and time-step resolution. *Am J Neuroradiol*. 2015;36(7):1310-1316.
21. Mynard JP, Valen-Sendstad K. A unified method for estimating pressure losses at vascular junctions. *Int J Numer Methods Biomed Eng*. 2015;31(7).
22. Khan MO, Steinman DA, Valen-Sendstad K. Non-Newtonian versus numerical rheology: practical impact of shear-thinning on the prediction of stable and unstable flows in intracranial aneurysms. *Int J Numer Methods Biomed Eng*. 2017;33(7).
23. Khan MO, Chnafa C, Gallo D, et al. On the quantification and visualization of transient periodic instabilities in pulsatile flows. *J Biomech*. 2017;52:179-182.
24. Welch P. The use of fast Fourier transform for the estimation of power spectra: a method based on time averaging over short, modified periodograms. *IEEE Trans Audio Electroacoust*. 1967;AU-15:70-73.
25. Sherwin SJ, Blackburn HM. Three-dimensional instabilities and transition of steady and pulsatile axisymmetric stenotic flows. *J Fluid Mech*. 2005;533:297-327.
26. Varghese SS, Frankel SH, Fischer PF. Direct numerical simulation of stenotic flows. Part 1. Steady flow. *J Fluid Mech*. 2007;582:253-280.
27. Varghese Sonu S., Frankel Steven H., Fischer Paul F.. Direct numerical simulation of stenotic flows. Part 2. Pulsatile flow. *J Fluid Mech*. 2007;582:281-318.
28. Blackburn H.. Working Dog. <http://users.monash.edu.au/~bburn/pdf/guidedog.pdf>. Accessed: June 20, 2018.
29. Blackburn HM, Sherwin SJ. Formulation of a Galerkin spectral element-Fourier method for three-dimensional incompressible flows in cylindrical geometries. *J Comput Phys*. 2004;197(2):759-778.
30. Drazin PG, Reid WH. *Hydrodynamic Stability*. Cambridge: Cambridge university press; 2004.
31. Carstensen S, Sumer BM, Fredsøe J. Coherent structures in wave boundary layers. Part 1. Oscillatory motion. *J Fluid Mech*. 2010;646:169-206.
32. Brenner S, Scott R. *The Mathematical Theory of Finite Element Methods*, Vol. 15. New York: Springer Science & Business Media; 2007.
33. Brachet ME, Meiron DI, Orszag SA, Nickel BG, Morf RH, Frisch U. Small-scale structure of the Taylor-Green vortex. *J Fluid Mech*. 1983;130:411-452.
34. Taylor GI, Green AE. Mechanism of the production of small eddies from large ones. *Proc R Soc Lond A Math Phys Sci*. 1937;158(895):499-521.
35. Brachet ME. Direct simulation of three-dimensional turbulence in the Taylor-Green vortex. *Fluid Dyn Res*. 1991;8(1):1-8.

36. Reynolds O. An experimental investigation of the circumstances which determine whether the motion of water shall be direct or sinuous, and of the law of resistance in parallel channels. *Proc R Soc Lond.* 1883;35(224-226):84-99.
37. Pfenninger W. Boundary layer suction experiments with laminar flow at high reynolds numbers in the inlet length of a tube by various suction methods. In: Lachmann GV, ed. *Boundary Layer and Flow Control.* Pergamon; 1961:961-980. <https://doi.org/10.1016/B978-1-4832-1323-1.50013-0>
38. Cassanova RA, Giddens DP. Disorder distal to modeled stenoses in steady and pulsatile flow. *J Biomech.* 1978;11(10-12):441-453.
39. Vétel J, Garon A, Pelletier D, Farinas M-I. Asymmetry and transition to turbulence in a smooth axisymmetric constriction. *J Fluid Mech.* 2008;607:351-386.
40. Fischer PF, Loth F, Lee SE, Lee S-W, Smith DS, Bassiouny HS. Simulation of high-Reynolds number vascular flows. *Comput Methods Appl Mech Eng.* 2007;196(31):3049-3060.
41. Taylor JO, Good BC, Paterno AV, et al. Analysis of transitional and turbulent flow through the FDA benchmark nozzle model using laser Doppler velocimetry. *Cardiovasc Eng Technol.* 2016;7(3):191-209.
42. Oberkampf WL, Roy CJ. *Verification and Validation in Scientific Computing.* Cambridge CB2 8BS, United Kingdom: Cambridge University Press; 2010.
43. Mullin Thomas. Experimental studies of transition to turbulence in a pipe. *Annu Rev Fluid Mech.* 2011;43:1-24.
44. Hof B, Juel A, Mullin T. Scaling of the turbulence transition threshold in a pipe. *Phys Rev Lett.* 2003;91(24):244502.
45. Peixinho J, Mullin T. Finite-amplitude thresholds for transition in pipe flow. *J Fluid Mech.* 2007;582:169-178.
46. Bhushan S, Walters DK, Burgreen GW. Laminar, turbulent, and transitional simulations in benchmark cases with cardiovascular device features. *Cardiovasc Eng Technol.* 2013;4(4):408-426.
47. Varghese SS, Frankel SH. Numerical modeling of pulsatile turbulent flow in stenotic vessels. *J Biomech Eng.* 2003;125(4):445-460.
48. Ducros F, Comte P, Lesieur M. Large-eddy simulation of transition to turbulence in a boundary layer developing spatially over a flat plate. *J Fluid Mech.* 1996;326:1-36.
49. Valen-Sendstad K, Mardal K-A, Mortensen M, Reif BAP, Langtangen HP. Direct numerical simulation of transitional flow in a patient-specific intracranial aneurysm. *J biomech.* 2011;44(16):2826-2832.
50. Bergersen AW. Investigating the link between patient-specific morphology and hemodynamics: Implications for aneurysm initiation? <https://www.duo.uio.no/bitstream/handle/10852/50515/master-bergersen.pdf>, Master's Thesis, University of Oslo, Norway; 2016.
51. Bertoglio C, Caiazzo A, Bazilevs Y, et al. Benchmark problems for numerical treatment of backflow at open boundaries. *Int J Numer Methods Biomed Eng.* 2018;34(2):e2918.
52. Griffith MD, Leweke T, Thompson MC, Hourigan K. Effect of small asymmetries on axisymmetric stenotic flow. *J Fluid Mech.* 2013;721:R1.
53. Steinman DA, Kehoe SC, Ford MD, Nikolov HN, Holdsworth DW. Dancing on the knife-edge of symmetry: On the misuse of symmetric models for studying blood flow dynamics. In: Proceedings of ASME 2003 Summer Bioengineering Conference. New York:ASME; 2003:25-29.
54. Ordsmith RJ. Pascal-an introduction to the art and science of programming. *Univ Comput.* 1988;10(3):164-164.


**How to cite this article:** Bergersen A, Mortensen M, Valen-Sendstad K. The FDA nozzle benchmark: “In theory there is no difference between theory and practice, but in practice there is”. *Int J Numer Meth Biomed Engng.* 2019;35:e3150. <https://doi.org/10.1002/cnm.3150>

## **II. Real-world variability in the prediction of intracranial aneurysm wall shear stress: The 2015 international aneurysm CFD challenge**





# Real-World Variability in the Prediction of Intracranial Aneurysm Wall Shear Stress: The 2015 International Aneurysm CFD Challenge

KRISTIAN VALEN-SENDSTAD,<sup>1</sup> ASLAK W. BERGERSEN,<sup>1,2</sup> YUJI SHIMOGONYA,<sup>3</sup> LEONID GOUBERGRITS,<sup>4</sup> JAN BRUENING,<sup>4</sup> JORDI PALLARES,<sup>5</sup> SALVATORE CITO,<sup>5</sup> SENOL PISKIN,<sup>6</sup> KEREM PEKKAN,<sup>7</sup> ARJAN J. GEERS,<sup>8</sup> IGNACIO LARRABIDE,<sup>9</sup> SAIKIRAN RAPAKA,<sup>10</sup> VIOREL MIHALEF,<sup>10</sup> WENYU FU,<sup>11</sup> AIKE QIAO,<sup>12</sup> KARTIK JAIN,<sup>1,13,14</sup> SABINE ROLLER,<sup>13</sup> KENT-ANDRE MARDAL,<sup>1,2</sup> RAMJI KAMAKOTI,<sup>15</sup> THOMAS SPIRKA,<sup>16</sup> NEIL ASHTON,<sup>17</sup> ALISTAIR REVELL,<sup>18</sup> NICOLAS ARISTOKLEOUS,<sup>19</sup> J. GRAEME HOUSTON,<sup>20</sup> MASANORI TSUJI,<sup>21</sup> FUJIMARO ISHIDA,<sup>21</sup> PRAHLAD G. MENON,<sup>22</sup> LEONARD D. BROWNE,<sup>19</sup> STEPHEN BRODERICK,<sup>19</sup> MASAOKI SHOJIMA,<sup>23</sup> SATOSHI KOIZUMI,<sup>23</sup> MICHAEL BARBOUR,<sup>24</sup> ALBERTO ALISEDA,<sup>24</sup> HERNÁN G. MORALES,<sup>25</sup> THIERRY LEFÈVRE,<sup>25</sup> SIMONA HODIS,<sup>26</sup> YAHIA M. AL-SMADI,<sup>27</sup> JUSTIN S. TRAN,<sup>28</sup> ALISON L. MARSDEN,<sup>28</sup> SREEJA VAIPPMADHOM,<sup>29</sup> G. ALBERT EINSTEIN,<sup>29</sup> ALISTAIR G. BROWN,<sup>30</sup> KRISTIAN DEBUS,<sup>30</sup> KUNYASU NIIZUMA,<sup>31</sup> SHERIF RASHAD,<sup>31</sup> SHIN-ICHIRO SUGIYAMA,<sup>32</sup> M. OWAIS KHAN,<sup>33</sup> ADAM R. UPDEGROVE,<sup>34</sup> SHAWN C. SHADDEN,<sup>34</sup> BART M. W. CORNELISSEN,<sup>35</sup> CHARLES B. L. M. MAJOIE,<sup>35</sup> PHILIPP BERG,<sup>36</sup> SYLVIA SAALFIELD,<sup>36</sup> KENICHI KONO,<sup>37</sup> and DAVID A. STEINMAN <sup>33</sup>

<sup>1</sup>Simula Research Laboratory and Center for Cardiological Innovation, Lysaker, Norway; <sup>2</sup>University of Oslo, Oslo, Norway; <sup>3</sup>Nihon University, Tokyo, Japan; <sup>4</sup>Charité – Universitätsmedizin Berlin, Berlin, Germany; <sup>5</sup>Universität Rovira i Virgili, Tarragona, Spain; <sup>6</sup>University of Texas at San Antonio, San Antonio, TX, USA; <sup>7</sup>Koc University, Istanbul, Turkey; <sup>8</sup>Universitat Pompeu Fabra, Barcelona, Spain; <sup>9</sup>Universidad Nacional del Centro de la Provincia de Buenos Aires, Buenos Aires, Argentina; <sup>10</sup>Siemens Medical Solutions USA Inc., Malvern, PA, USA; <sup>11</sup>Beijing Union University, Beijing, China; <sup>12</sup>Beijing University of Technology, Beijing, China; <sup>13</sup>University of Siegen, Siegen, Germany; <sup>14</sup>University of Zürich, Zurich, Switzerland; <sup>15</sup>Dassault Systemes, Paris, France; <sup>16</sup>Simpleware Software Solutions, Exeter, UK; <sup>17</sup>University of Oxford, Oxford, UK; <sup>18</sup>University of Manchester, Manchester, UK; <sup>19</sup>University of Limerick, Limerick, Ireland; <sup>20</sup>University of Dundee, Dundee, UK; <sup>21</sup>Mie Chuo Medical Center, Tsu, Japan; <sup>22</sup>University of Pittsburgh, Pittsburgh, PA, USA; <sup>23</sup>University of Tokyo, Tokyo, Japan; <sup>24</sup>University of Washington, Seattle, USA; <sup>25</sup>Medisys - Philips Research Paris, Paris, France; <sup>26</sup>Texas A&M University - Kingsville, Kingsville, TX, USA; <sup>27</sup>Jordan University of Science and Technology, Irbid, Jordan; <sup>28</sup>Stanford University, Stanford, CA, USA; <sup>29</sup>EinNel Technologies, Chennai, India; <sup>30</sup>Siemens PLM Software, Plano, TX, USA; <sup>31</sup>Tohoku University, Sendai, Japan; <sup>32</sup>Kohnan Hospital, Sendai, Japan; <sup>33</sup>University of Toronto, Toronto, ON, Canada; <sup>34</sup>University of California, Berkeley, Berkeley, CA, USA; <sup>35</sup>Academic Medical Center, Amsterdam, The Netherlands; <sup>36</sup>University of Magdeburg, Magdeburg, Germany; and <sup>37</sup>Wakayama Rosai Hospital, Wakayama, Japan

(Received 17 June 2018; accepted 11 August 2018; published online 10 September 2018)

Associate Editors Francesco Migliavacca and Ajit P. Yoganathan oversaw the review of this article.

## Abstract

**Purpose**—Image-based computational fluid dynamics (CFD) is widely used to predict intracranial aneurysm wall shear stress (WSS), particularly with the goal of improving rupture risk assessment. Nevertheless, concern has been expressed over the variability of predicted WSS and inconsistent associations with rupture. Previous challenges, and studies from individual groups, have focused on individual aspects of the image-based CFD pipeline. The aim of this Challenge was to quantify the total variability of the whole pipeline. **Methods**—3D rotational angiography image volumes of five middle cerebral artery aneurysms were provided to participants, who were free to choose their segmentation methods,

boundary conditions, and CFD solver and settings. Participants were asked to fill out a questionnaire about their solution strategies and experience with aneurysm CFD, and provide surface distributions of WSS magnitude, from which we objectively derived a variety of hemodynamic parameters. **Results**—A total of 28 datasets were submitted, from 26 teams with varying levels of self-assessed experience. Wide variability of segmentations, CFD model extents, and inflow rates resulted in interquartile ranges of sac average WSS up to 56%, which reduced to < 30% after normalizing by parent artery WSS. Sac-maximum WSS and low shear area were more variable, while rank-ordering of cases by low or high shear showed only modest consensus among teams. Experience was not a significant predictor of variability. **Conclusions**—Wide variability exists in the prediction of intracranial aneurysm WSS. While segmentation and CFD solver techniques may be difficult to standardize across groups, our findings suggest that some of the variability in image-based CFD could be reduced by establishing guideli-

Address correspondence to David A. Steinman, University of Toronto, Toronto, ON, Canada. Electronic mail: steinman@mie.toronto.ca

Kristian Valen-Sendstad and Aslak W. Bergersen have contributed equally to this work.

nes for model extents, inflow rates, and blood properties, and by encouraging the reporting of normalized hemodynamic parameters.

**Keywords**—Intracranial aneurysm, Patient-specific modelling, Wall shear stress, Rupture risk, Uncertainty quantification.

## INTRODUCTION

Since the first individual case studies were published more than 15 years ago,<sup>18,22,42</sup> medical image-based computational fluid dynamics (CFD) of intracranial aneurysms has become a widely-used tool for elucidating the role of hemodynamic forces in aneurysm development and rupture.<sup>39</sup> Large retrospective studies (~ 200 cases) have shown associations between both low<sup>47</sup> and high<sup>9</sup> wall shear stress (WSS) and aneurysm rupture status, a seeming contradiction that may simply reflect a Janus-faced nature of aneurysm wall remodelling.<sup>31</sup> On the other hand, it may also reflect the variability in the assumptions and compromises of aneurysm CFD studies, as well as inconsistent definitions of these (e.g., absolute vs. normalized) and other hemodynamic parameters associated with rupture.<sup>5,31,36</sup>

Image-based CFD is subject to numerous sources of uncertainty along its pipeline: the clinical modality used to image the aneurysm<sup>4,16,17</sup>; digital segmentation of the lumen, often requiring subjective decisions about thresholds, filtering, smoothing, *etc.*<sup>15,34,38</sup>; truncation of the domain and attendant assumptions about velocity boundary conditions<sup>7,19,30</sup>; the need to assume flow rates,<sup>21,25,32</sup> since patient-specific measurements are rarely available; the pragmatic assumption of rigid walls<sup>2,12,46</sup> and simple blood rheologies<sup>6,27,48</sup> when, similarly, patient-specific properties are difficult or impossible to obtain; and the choice of mesh and time-step resolutions, as well as other CFD solver settings.<sup>13,44,45</sup> Common to the above-cited studies is that they were performed by individual research teams and focused on a single source of variability, all other factors being equal.

Triggered by a controversy in the clinical literature regarding a CFD-driven hypothesis about aneurysm treatment failures,<sup>40</sup> a first International Aneurysm CFD Challenge was launched in 2012,<sup>41</sup> focusing on a single giant internal carotid artery (ICA) side-wall aneurysm case. Participants were provided with the segmented lumen geometry, pulsatile flow rates, and blood properties, leaving the CFD solver and settings the only potential source of variability. Peak-systolic pressure drops were found to be predicted to within 8%, but peak-systolic velocity jetting into the sac

turned out to be highly variable among the 27 CFD solutions submitted, including several that predicted flow instabilities where the rest did not. Closer, but not perfect, agreement was found for cycle-averaged velocity patterns.

A second Challenge was launched in 2013, to test whether, given two middle cerebral artery (MCA) bifurcation aneurysm cases, participants could identify the ruptured aneurysm, and also the site of rupture. In the first phase,<sup>20</sup> 26 participating teams were provided with the segmented lumen geometry, requiring them to choose flow boundary conditions and blood properties. Despite a wide range of mesh densities, velocity boundary conditions and flow rates employed, all but five of the teams correctly identified the ruptured case, typically (but not exclusively) with low WSS as a determining factor; however, only one team correctly identified the rupture site. The organizers noted that the submitted WSS distributions had widely different magnitudes, so chose to display them normalized by their respective maximum WSS. Qualitative agreement was seen among most cases, but no quantification was provided. The organizers also noted, “[a]lthough some groups were highly experienced in other fields of engineering, the survey of the abstracts revealed that unrealistic inflow rates or velocities were applied. For instance, one group defined an inflow velocity of 10 m/s”.

In the second phase of the 2013 Challenge,<sup>3</sup> participants were provided with flow rates and blood properties in order to narrow the source of variability to the CFD solution strategy alone. Centerline pressures and velocities showed generally good agreement, albeit with a handful of outliers, similar to what was seen in the first CFD Challenge.<sup>41</sup> Velocity magnitudes on selected planes through the two models were also compared, showing that most groups captured the same flow patterns, and agreed to within about 20%.

In 2015, we (K.V.-S., K.K., and D.A.S.) decided to launch a third Challenge that would not only include more cases (five), but provide *no* information to participants beyond the source medical image volumes. The goal was twofold: (i) to test the ability to identify the ruptured cases, where the chances of guessing correctly was low, rather than 50% as in the previous Challenge; and (ii) to understand, for the first time, the total or “real-world” variability of aneurysm CFD. The results of the rupture prediction will be reported separately. The aim of the present study was to quantify the variability of image-based CFD predictions of aneurysm WSS when teams are left to choose their own segmentation methods, boundary conditions, blood properties, and CFD solution strategies.



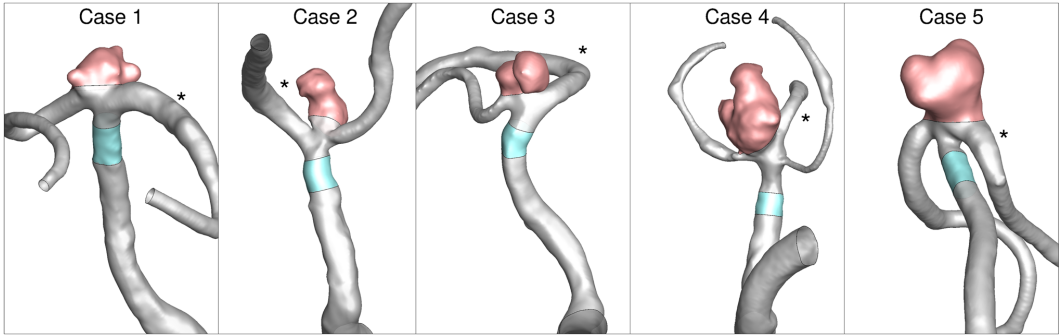


**FIGURE 1.** Representative segmentations of the five MCA aneurysm cases, showing the sac (pink) and parent artery (cyan) segments over which WSS was objectively averaged as described in the Methods. The \* in each panel identifies dominant outflow branch, used to define the outflow division for all teams.

## METHODS

### Challenge Study Design

As shown in Fig. 1, five MCA bifurcation aneurysms were selected by one of the authors (K.K.) for having good 3D rotational angiography (3DRA) image quality, irregular shape, and similar size (~ 8 mm). The cases included a mix of ruptured and unruptured aneurysms; however, participants were blinded to rupture status. Challenge organizers confirmed that the five cases could be segmented and that CFD simulations could be carried out on the segmented models (those datasets were not included in the present study).

Teams were provided only with the DICOM image volumes, which included the ICA and the proximal and distal MCAs. Participants were free to choose their own segmentation methods, CFD solution strategies, flow rate and/or pressure boundary conditions, and material properties, mimicking real-world conditions for aneurysm CFD collaborations between clinicians and engineers. Among other relevant information, teams were asked to fill out a questionnaire with details on their solution strategy, and their self-assessed experience based on the number of aneurysm cases they had segmented and simulated: high (> 100 cases); medium (11–100 cases); low (1–10 cases); or none (0 cases). The questionnaire and the instructions sent to the teams are included in an online data repository.<sup>1</sup> Teams were also asked to provide velocity and WSS fields (time-averaged and peak systolic for pulsatile simulations) for all five aneurysm cases. (Additionally, teams were asked to provide predictions of rupture status, and the geometric/hemodynamic parameters on which they were based; those results will be reported separately.)

### Response to the Challenge

A total of 45 teams registered for the Challenge, of which 26 provided CFD datasets including WSS fields. Two of these teams provided CFD datasets from two different segmentations; as discussed later, there were non-negligible intra-team differences, and so we treated these as independent submissions, resulting in 28 CFD datasets. Datasets from three teams were incomplete: Team 20 did not provide WSS or velocity fields for Case 5; Team 21 did not provide any velocity fields; and Team 24 provided the velocity field only for Case 1. Most teams provided velocity data as vector fields; however three teams (10, 13, 17) provided velocity magnitudes only.

### Centralized Data Analysis

Despite being derived from the same DICOM image volumes, the lumen geometries provided by the participating teams were in different scales, coordinate systems, rotations, and even mirrored. These were therefore first scaled to consistent units (mm) and mirrored if necessary. Centerlines were computed automatically from the lumen surfaces using the Vascular Modelling ToolKit (VMTK; [www.vmtk.org](http://www.vmtk.org)), albeit with manual correction for some non-manifold surfaces. These were then initially registered automatically *via* the origin of the bifurcation hosting the aneurysm.<sup>33</sup> Owing to the wide variability of the segmentations, surfaces were further manually rotated and translated to best match each other. The original and registered lumen surfaces, and the registered velocity and WSS fields are provided in the online data repository.<sup>1</sup>

Besides simplifying the visualisation of the multiple datasets, an advantage of registering the fields is that we could delineate a consistent segment of the parent

artery (MCA) and the aneurysm sac using the same clipping planes for all teams. From the velocity datasets, lumen areas and mean through-plane velocities were calculated and averaged from five transverse slices (one slice for Case 4) through the MCA segment (c.f., cyan regions in Fig. 1). For the three teams that did not provide velocity *vectors*, we used their provided velocity magnitudes instead, after confirming that there was high correlation and no appreciable bias between velocities calculated from vectors vs. magnitudes from the other teams ( $R^2 = 0.998$ , slope = 1.02).

#### Parent Artery and Sac Hemodynamic Parameters

From the above areas and mean velocities we derived the parent artery diameters (assuming circular cross-sections), flow rates (area  $\times$  velocity), Reynolds numbers (velocity  $\times$  diameter  $\times$  blood density/dynamic viscosity) and Poiseuille wall shear stress ( $32 \times$  dynamic viscosity  $\times$  flow rate/diameter<sup>3</sup>). Slices were also placed at a consistent location for each of the outlet branches in order to compute the flow rates, from which outflow divisions were determined. Again, it was confirmed that outflow divisions derived from velocity magnitudes were consistent with those from vector velocities ( $R^2 = 0.985$ , slope = 0.97).

After clipping and isolating the aneurysm sac from the steady or time-averaged pulsatile WSS fields (c.f., pink regions in Fig. 1), we computed a trio of the simplest and arguably most-commonly-reported hemodynamic parameters<sup>5</sup>: AWSS, the sac-averaged WSS magnitude, in Pa; MWSS, the sac-maximum WSS magnitude,<sup>9</sup> in Pa; and LSA, here defined as the surface area of the aneurysm sac exposed to WSS  $< 0.4$  Pa and divided by the total sac area.<sup>23</sup> A number of groups have also proposed normalizing these parameters to the parent artery WSS. After computing the average WSS magnitude over the clipped MCA segment, the following normalized hemodynamic parameters were computed: AWSS\* = AWSS normalized by parent artery WSS<sup>47</sup>; MWSS\* = MWSS normalized by the parent artery WSS<sup>47</sup>; and LSA\*, the surface area of the aneurysm sac exposed to WSS  $< 0.1 \times$  parent artery WSS, divided by the total sac area.<sup>47</sup>

Team characteristics and derived parent artery and sac hemodynamic parameters are provided in spreadsheet form in the online data repository.<sup>1</sup> Teams are identified by their assigned ID number; however, certain information (country of origin, segmentation and CFD details) has been omitted in order to preserve team anonymity.

#### Statistical Analysis

Almost all of the derived hemodynamic parameters did not have normal distributions according to D'Agostino & Pearson omnibus tests, and so are reported as median and interquartile range (IQR, the first ( $Q_1$ ) to third ( $Q_3$ ) quartile), with percent variability reported as the quartile coefficient of dispersion [ $\text{CoD} = (Q_3 - Q_1)/(Q_3 + Q_1)$ ]. While most input parameters (flow rates, *etc.*) were found to be normally distributed, we chose to report them also using medians, IQR and CoD to be consistent with the statistics of the output hemodynamic parameters.

These descriptive statistics were calculated for each case individually, but also based on teams' averages across the five cases, referred to as the "case-average" statistics. Where there might be missing data for one or more cases from a given team for a particular parameter, that team's case-average value was not included. Kruskal-Wallis with *post hoc* Dunn's tests were performed to determine whether significant differences in medians could be detected across aneurysm cases or experience levels, in light of variability. All statistical analyses were performed using Prism 6.0 (Graphpad Software, La Jolla CA), and significance was assumed at  $p < 0.05$ .

## RESULTS

#### Team, Solver, and Segmentation Variability

Per Table 1, there was a representative distribution of experience among the teams: 5 self-identified as highly experienced ( $> 100$  cases) for both segmentation and CFD of cerebral aneurysms; 8 teams reported low or no experience (10 or fewer cases) with aneurysm segmentation or CFD; and the remaining 13 teams were somewhere in between. There was a good international distribution of teams, including high-experience teams from three continents.

For CFD, more than half of the teams used a commercial solver, the rest using open-source or in-house codes. Interestingly, however, all high-experience groups used commercial (Ansys) solvers. The mesh resolution, distribution of cells in the domain, and local refinement, as well as solver settings, varied widely among teams, to the extent that objective comparisons were not attempted for the present study. All teams assumed rigid walls with no slip boundary conditions. Almost all teams assumed a Newtonian rheology, with blood density typically between 1.05 and 1.06 g/cm<sup>3</sup>, and viscosity almost equally divided between 3.5 and 4.0 cPoise (N.B., a 13% difference).

A wide variety of software tools was used for segmentation, and these and other tools were also used for

**TABLE 1. Summary of team/simulation characteristics.**

	Experience <sup>a</sup>			All
	High	Medium	Low	
Number of teams	5	13	8	26
Continent <sup>b</sup>				
Europe	1.5	6.5	3	11
North or South America	1.5	3.5	4	9
Asia	2	3	1	6
Segmentation software <sup>c</sup>				
Mimics	2	2	1	5
VMTK	1	4	0	5
ITK-Snap	1	1	2	4
3D Slicer	0	1	2	3
Simvascular	0	0	2	2
Other	2	5	2	9
CFD software				
Fluent	3	4	1	8
CFX	2	2	0	4
Star-CCM+	0	0	3	3
OpenFOAM	0	2	0	2
Simvascular	0	0	2	2
Other	0	5	2	7
Rheology model				
Newtonian	4	13	6	23
Non-Newtonian	1	0	2	3
Viscosity (cPoise)				
3.5	3	5	4	12
3.7	0	1	1	2
4.0	2	7	3	12
Density (g/cm <sup>3</sup> )				
1.05–1.06	4	11	7	22
Other (1.0–1.05)	1	2	1	4
Temporal scheme				
Steady	4	7	4	15
Pulsatile	1	6	4	11
Inlet location				
MCA	0	11	6	17
ICA	5	2	2	9
Inflow scaling <sup>d</sup>				
Same flow rate ( $n = 0$ )	2	3	1	6
Same Re ( $n = 1$ )	0	1	1	2
Same velocity ( $n = 2$ )	1	6	3	10
Same WSS ( $n = 3$ )	2	1	1	4
Other	0	2	2	4
Inflow BC				
Plug	2	7	4	13
Poiseuille	3	3	2	8
Womersley	0	2	2	4
Other	0	1	0	1
Outflow BC				
Zero pressure	4	10	4	18
Cube (Murray's) law	1	1	2	4
Other	0	2	2	4

<sup>a</sup>High: > 100 cases; Medium: 11–100 cases; Low: 10 or fewer cases.

<sup>b</sup>Fractional values reflect teams split across continents.

<sup>c</sup>Total = 28 since two teams used different software used for their two segmentations.

<sup>d</sup>Power law relating flow rate to diameter, i.e.,  $Q \sim D^n$ .

editing (smoothing, clipping, *etc.*) of the models. There was no obvious software preference based on experience level. Figure 2 shows the wide variability in segmentation and model extents, e.g., truncation of inlet at MCA vs. ICA, number and length of outflow and side branches, length of cylindrical flow extensions, *etc.* Notably, two-thirds of teams truncated their models at the MCA, and with varying lengths, while all high-experience teams included the ICA. The number of outlets (side or distal braches) also varied widely among teams.

Taking a closer look at the aneurysms and parent arteries, Fig. 3 shows that, qualitatively and depending on the case, there could be wide variability in sac morphology and smoothness, neck size and location, and number and size of branches. For example, in Case 1 the number and size of the blebs was inconsistent, and there were clear differences in the diameters of the parent arteries (e.g., Team 3 vs. 5). For Case 2, the shape of the dome was highly variable, as were the neck location and width (e.g., Team 8 vs. 13). For Case 3 the width of the neck was also variable (e.g., Team 2 vs. 37), and although not visible in this view, so was the bottlenecking of the sac between two main lobes. For Case 4 the sac morphology and neck were more consistent, but the number and size of daughter branches was highly variable (e.g., Team 17 vs. 19a). For Case 5 the neck also appeared to be consistent among teams, but the degree of the stenosis proximal to the sac did not (e.g., Team 39 vs. 42).

Table 2 and Fig. 4a show that, despite the variety of segmentation tools and techniques, and segmentation variability noted above, the MCA diameter, measured at a consistent location across teams, had a case-average CoD of only 3.4%, albeit up to 9% for Case 1 (N.B., which translates to CoD of 18% for cross-sectional area.). Significant differences in diameters for some of the cases could be detected ( $p < 0.0001$ ), notably Cases 1–3 vs. Case 4 and 5. On average, variability was higher for low experience vs. medium or high experience teams; however, this was not true for individual aneurysm cases.

#### *Inflow and Outflow Variability*

Since teams were challenged to carry out the CFD that *they* would require to predict rupture status, they were not obligated to assume pulsatile flows. In fact, just over half of the teams assumed steady flow conditions, including all but one of the high-experience teams. Of the 11 teams that used pulsatile simulations, waveforms were derived from a variety of sources (published vs. measured in-house vs. reduced-order

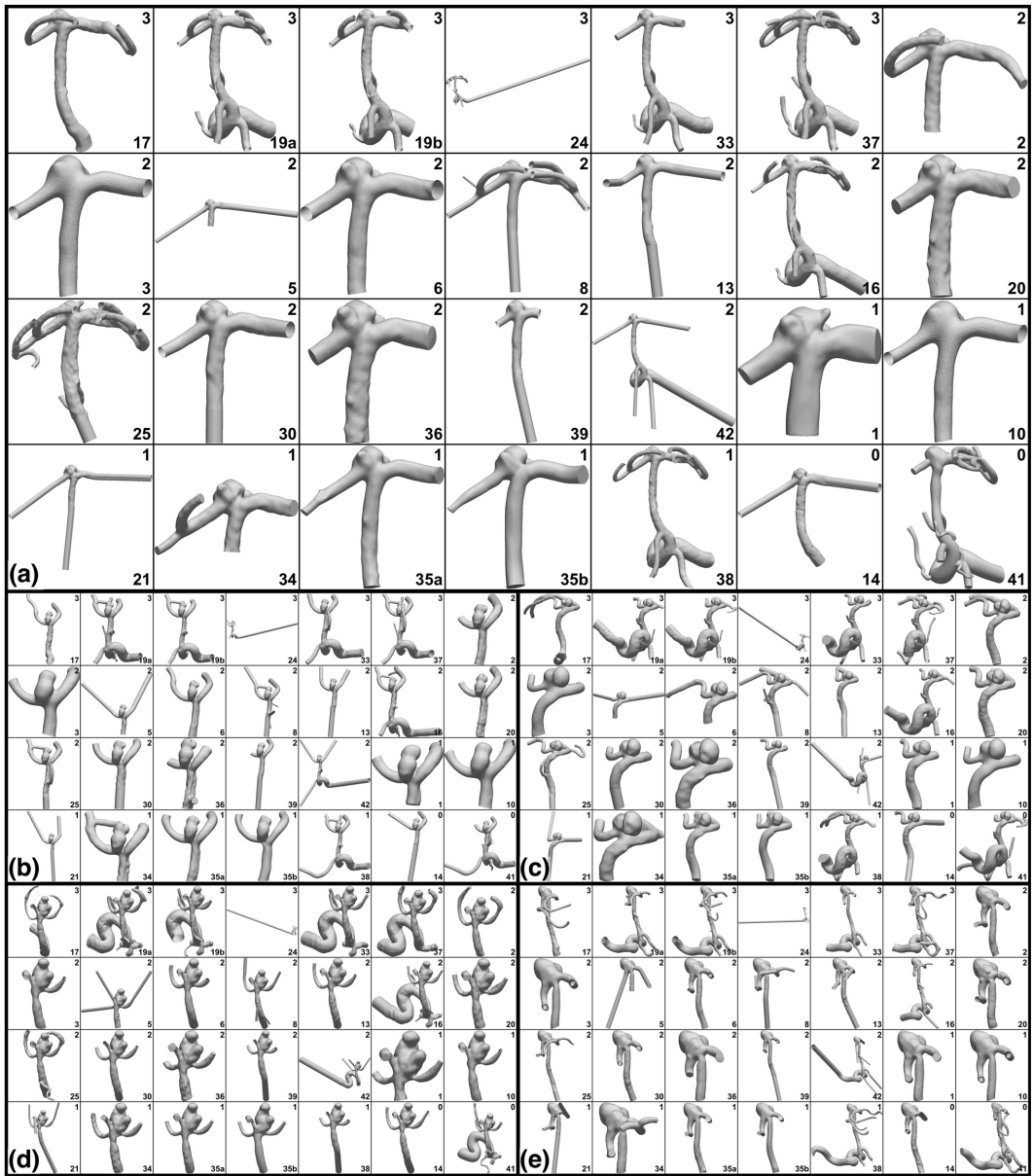


**FIGURE 2. Variability of CFD model domains.** (a) shows Case 1 at full size, while (b–e) show Cases 2–5 at reduced size in the interest of space. For each case, models are shown from top left to bottom right in descending order of team experience indicated in the top right corner of each panel: 3 = high; 2 = medium; 1/0 = low. Team number is shown at bottom right of each panel. For each case, models are all shown in the same view, but obviously not to the same scale.

model), vessels (common carotid artery vs. ICA vs. MCA), or cohorts (young adult vs. older adult vs. aneurysm patient).

The way in which steady or cycle-averaged flow rates were assigned by teams to the five aneurysm cases was also highly variable. Per Table 1, a plurality of

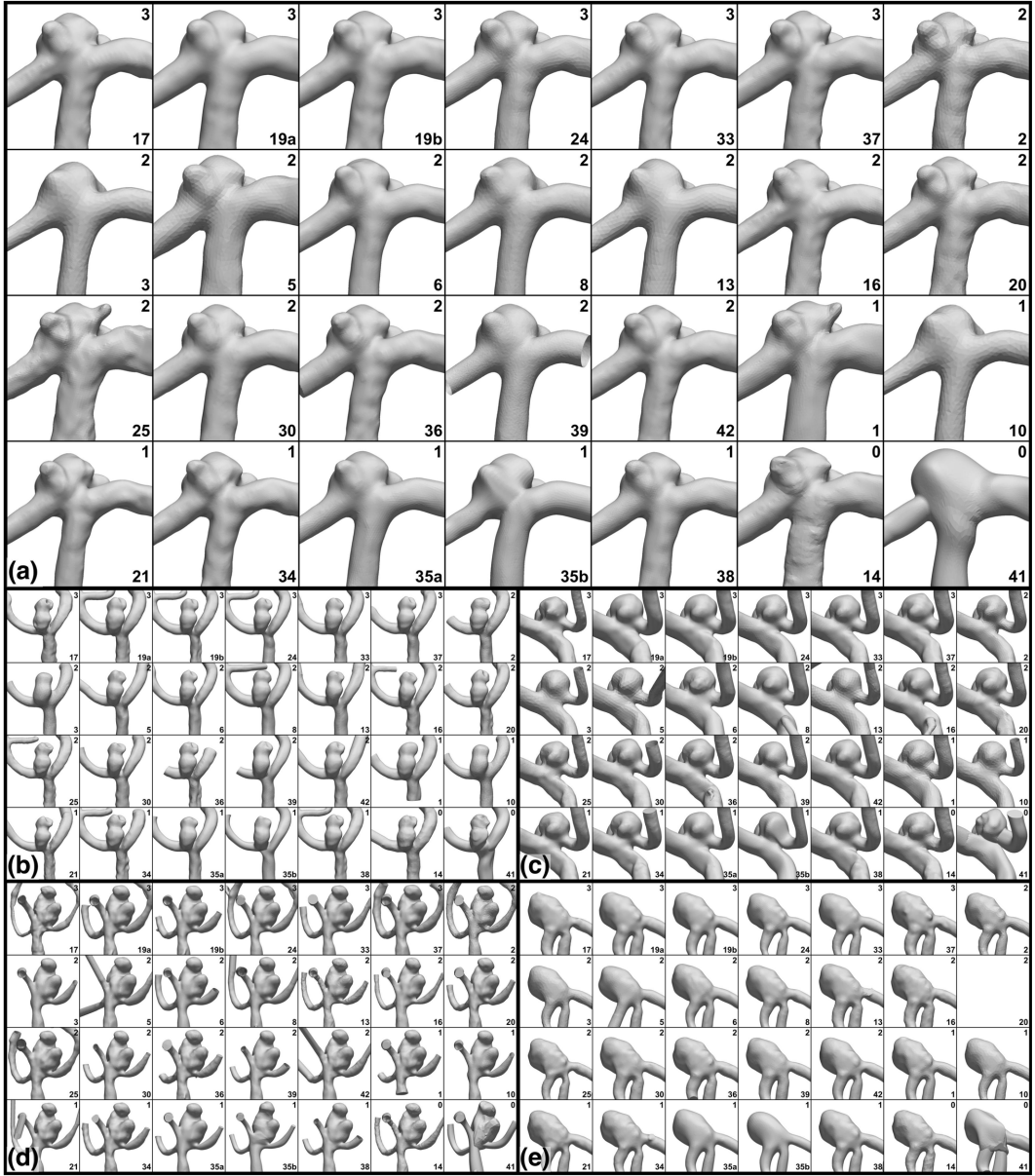


**FIGURE 3.** Variability of segmentations, focusing on the aneurysm and parent artery, with (a–e) showing Cases 1–5. Unlike Fig. 2, models are now zoomed in and, for each case, shown to the same scale in order to appreciate qualitative differences in sac and neck morphology, parent artery dimensions, and smoothness. As the surfaces are derived from the team-contributed WSS fields, mesh density may also be inferred from the faceting of the shaded surface. Experience levels and team numbers are shown in each panel, as explained in the caption of Fig. 2.

**TABLE 2. Descriptive statistics for parent artery (MCA) inflow and outflow parameters, based on team case-average data.**

Experience	N	Median	IQR	CoD (%)
<b>Diameter (mm)</b>				
All	27	2.45	2.40–2.56	3.4
High	6	2.50	2.39–2.56	3.5
Medium	12	2.47	2.40–2.58	3.4
Low	9	2.41	2.32–2.62	6.0
<b>Flow rate (mL/s)</b>				
All	25	2.40	1.82–2.91	23
High	5	1.99	1.63–2.81	27
Medium	12	2.30	1.88–2.95	22
Low	8	2.67	2.00–3.65	29
<b>Velocity (cm/s)</b>				
All	25	49.0	38.0–63.2	25
High	5	42.3	32.8–59.3	29
Medium	12	50.9	36.7–62.6	26
Low	8	59.0	40.1–76.8	31
<b>Reynolds number (-)</b>				
All	25	345	266–450	26
High	5	282	227–424	30
Medium	12	334	270–451	25
Low	8	376	288–535	30
<b>Poiseuille WSS (Pa)</b>				
All	25	6.19	4.48–8.31	30
High	5	4.91	3.91–7.16	29
Medium	12	6.48	4.11–7.61	30
Low	8	7.94	4.72–9.32	33
<b>Calculated WSS (Pa)</b>				
All	27	8.29	4.50–12.2	46
High	6	7.04	4.64–10.0	37
Medium	12	9.44	5.41–13.2	42
Low	9	6.51	4.05–12.9	52
<b>WSS ratio<sup>a</sup> (-)</b>				
All	25	1.51	1.20–1.67	16
High	5	1.45	1.23–1.55	11
Medium	12	1.60	1.26–1.80	18
Low	8	1.37	1.03–1.64	23
<b>Flow division (-)</b>				
All	25	0.65	0.62–0.69	5
High	5	0.64	0.56–0.67	9
Medium	12	0.65	0.63–0.69	4
Low	8	0.65	0.62–0.70	6

<sup>a</sup>Ratio of Calculated:Poiseuille WSS.

teams (10/38%) assumed the same inlet velocity for all cases, which is tantamount to assuming that flow rate scales with inlet diameter squared (i.e.,  $Q \sim D^2$ ). The next most common assumption (6/23%) was the same flow rate for all cases ( $Q \sim D^0$ ) followed by same WSS ( $Q \sim D^3$ ) and same Re ( $Q \sim D^1$ ). Even among the high-experience teams there was no consistency in the inflow scaling approach: two teams each assumed same WSS or flow rate, and one assumed same velocity. All but one of the 26 teams imposed their assigned inflow *via* Dirichlet (velocity profile) boundary conditions, the other team imposing pressure at both inlet and outlets. Inlet velocity profile shapes were almost equally dis-

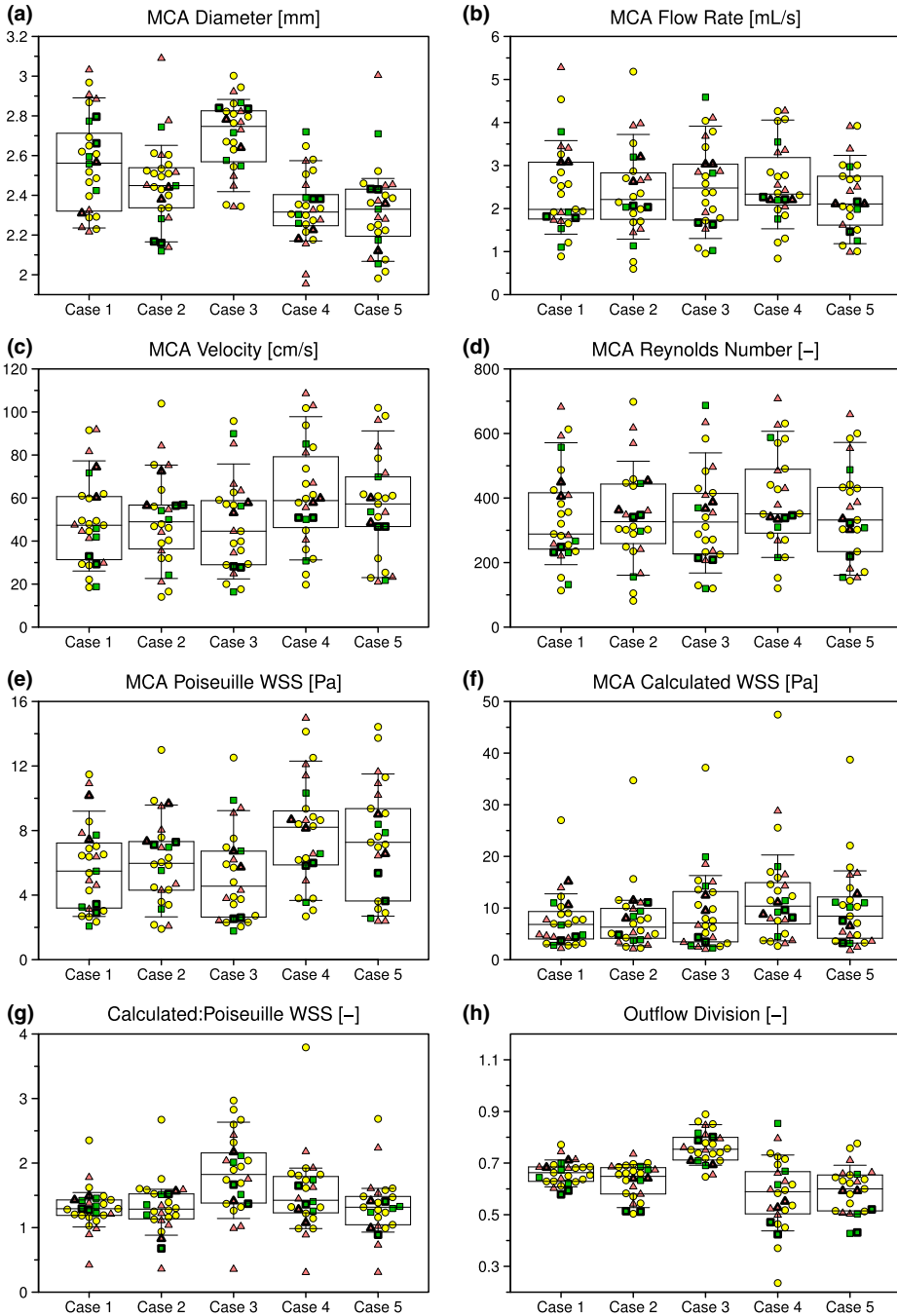
**FIGURE 4. Variability of selected inflow/outflow parameters derived as described in the Methods. Green squares, yellow circles and red triangles identify data from teams with high, medium and low experience, respectively. Thicker symbols highlight the teams that contributed CFD datasets from two different segmentations. Superimposed horizontal lines, boxes, and whiskers identify median, IQR, and 90th percentile ranges for each case.**

tributed between plug and fully-developed (Poiseuille or Womersley), irrespective of experience level.

Per Table 2 and Figs. 4b–4g, the above variability in inflow strategies resulted in relatively wide variability in parent artery inflow characteristics. Flow rates varied by CoD = 23% on average, but up to CoD = 29% for Cases 3 and 5. As a result, there was no significant difference in median flow rates across the cases, nor was there a significant difference in medians due to experience level. This was also true for MCA velocities, which had case-average CoD = 25%, but up to 38% for Case 3; and for Reynolds number (Re), which had case-average CoD = 26%, and a maximum of 32% for Case 5.

The nominal (Poiseuille) inflow WSS, calculated from each team's MCA diameter, flow rate, and blood viscosity/density, had a median value of 6.2 Pa (N.B., more than 4× the “normal” arterial WSS of 1.5 Pa<sup>29</sup>). The CFD-calculated inflow WSS, based on circumferentially averaging each CFD model over consistent parent artery segments (shown in Fig. 1), was higher at 8.3 Pa. Indeed, the median ratio of calculated:Poiseuille WSS was 1.5, and varied significantly ( $p = 0.007$ ) from 1.3 (Cases 1, 2 and 5) to 1.8 (Case 3). Variability for calculated WSS, at CoD = 46%, was also higher than variability for Poiseuille WSS, at 30%. As such, while a significant difference in Poiseuille WSS between Cases 3 and 4 could be detected ( $p = 0.014$ ), differences in calculated WSS could not. Variabilities for the ratio of Calculated:Poiseuille WSS ratio were lower (case-average CoD = 16%), suggesting that variability of calculated WSS among teams was driven more by differences in velocity *magnitudes* than velocity profile *shapes*. At the same time, among teams whose CFD models included the ICA siphon, the median ratio ranged from 1.3 to 1.7 among the cases, indicating that velocity profiles in the MCA cannot be assumed to be fully developed.

At the outlets, the majority of teams (18/69%), including all but one of the most experienced teams, assumed traction free conditions with zero pressure at all outlets. The second most popular approach (4/15%) was to divide outflows according to the cube of the diameter (i.e., Murray's law), although it was not clear whether this was done explicitly with velocity profile (Dirichlet) or flux/pressure (Neumann) boundary conditions. The rest used either different scaling



laws, reduced-order models, or did not specify. Despite the variability in outflow schemes, however, the division of outflow to the dominant branch was remarkably consistent (case-average CoD = 5%), with Case 4 having the highest variability (CoD = 16%) owing to the presence of three similarly-sized daughter branches (c.f., two branches for the other cases). As a result, there were significant differences ( $p < 0.0001$ ) in median outflow divisions among some cases, notably Case 3.

### Wall Shear Stress Variability

A qualitative overview of the variability of the computed WSS fields is presented in Fig. 5, demonstrating the wide differences in the magnitudes and spatial distribution of WSS, even among the most experienced teams. Indeed, the only consistency appears to be inconsistency among the teams. Figure 6 shows that a more consistent pattern of WSS emerges after normalizing by the parent artery (MCA) WSS, albeit still with sometimes appreciable differences in the location and extent of WSS extrema among teams, including among the most experienced teams.

A more quantitative view of these results is presented in Table 3 and Fig. 7. Compared to the MCA inflow and outflow parameters shown in Table 2 and Fig. 4, there was, not surprisingly, more variability in hemodynamic parameters derived from the aneurysm sac. The most commonly reported parameter in the aneurysm CFD literature, sac-averaged WSS magnitude (here denoted AWSS), varied by CoD = 48% on average, but with CoD up to 60% for Case 1. There was no significant difference in case-averaged medians across aneurysm cases or experience levels. Case-average variability was reduced substantially after normalizing (i.e., AWSS\*) to CoD = 18%, with a maximum CoD = 32% for Case 4 owing to its low median value. As a result, differences in medians across cases could be detected ( $p < 0.0001$ ), notably between Cases 1 and 5 vs. 2–4.

Sac-maximum WSS (MWSS), being based on a point-wise rather than sac-averaged quantity, had  $\sim 10\times$  higher IQR than AWSS; however, since the median MWSS was also  $\sim 10\times$  higher, case-average CoD was identical to that of AWSS at 48%, albeit with three cases (2, 3 and 5) having individual CoD  $> 60\%$  for MWSS. Case-average CoD for MWSS\* was 22%, only slightly higher than 18% for AWSS\*. Whereas for MWSS medians were only significantly different between Cases 2 and 4 ( $p = 0.003$ ), for MWSS\* Cases 1, 4, and 5 had significantly higher medians than Cases 2 and 3 ( $p < 0.0001$ ).

Per Figs. 7e and 7f, LSA and LSA\* both appeared to have similar variabilities to the other hemodynamic

parameters, but as discussed later, had more apparent outliers. Case-average variabilities for LSA and LSA\* were CoD = 63% and 30%, respectively, reflecting that, although both are dimensionless parameters, the threshold for low WSS is absolute for LSA, but relative to the parent artery for LSA\*. CoD for individual cases were  $> 90\%$  for both LSA (Cases 1, 3, and 5) and LSA\* (Case 1), reflecting that the lowest quartile ( $Q_1$ ) value was close to 0. Nevertheless, despite these differences in case-average CoD between LSA and LSA\*, and the high case-specific CoD, median LSA and LSA\* were both significantly higher for Cases 2–4 vs. Cases 1 and 5 ( $p < 0.0001$ ).

Finally, it could be imagined that, irrespective of differences in absolute values of a given hemodynamic parameter *between* teams, teams might be more consistent in terms of *rank-ordering* cases from low to high WSS. As shown in Fig. 8, rank-ordering did not eliminate variability, but it did seem to mitigate it. For dimensional hemodynamic parameters, consensus (i.e., more than half of teams) was reached only for Case 1 as having the highest-ranked AWSS and lowest-ranked LSA, and Case 4 having the highest-ranked MWSS. This could be seen as an improvement over absolute AWSS and MWSS as shown in Fig. 7, which because of the variability could not significantly discriminate a single case as having the highest value. Focusing on the normalized hemodynamic parameters, whereas AWSS\* values shown in Fig. 7b could only significantly differentiate Cases 2–4 as low from Cases 1 and 5 as high, Fig. 8b shows that the majority of teams ranked Case 4 as having the lowest AWSS\*, and nearly all teams ranked Case 1 as having the highest. Similarly, whereas MWSS\* values in Fig. 7d could only identify significantly higher values for Cases 1, 4, and 5 vs. Cases 2 and 3, Fig. 8d showed that more teams ranked Case 4 as having the highest MWSS\*. Finally, whereas LSA and LSA\* could only significantly differentiate Cases 2–4 as high from Cases 1 and 5 as low in Figs. 7e, 7f, and 8e, 8f shows that the majority clearly identified Cases 3 and 4 as having the highest LSA and LSA\* and Case 1 followed by Case 5 having the lowest.

## DISCUSSION

### Summary of Key Findings

To the best of our knowledge, this Challenge presents the first report of the total (“real-world”) variability in aneurysm WSS as predicted by image-based aneurysm CFD, at least as practiced ca. 2015. It shows that there was appreciable variability in the prediction of aneurysm WSS, driven by the broad variety of strategies employed among participating teams for



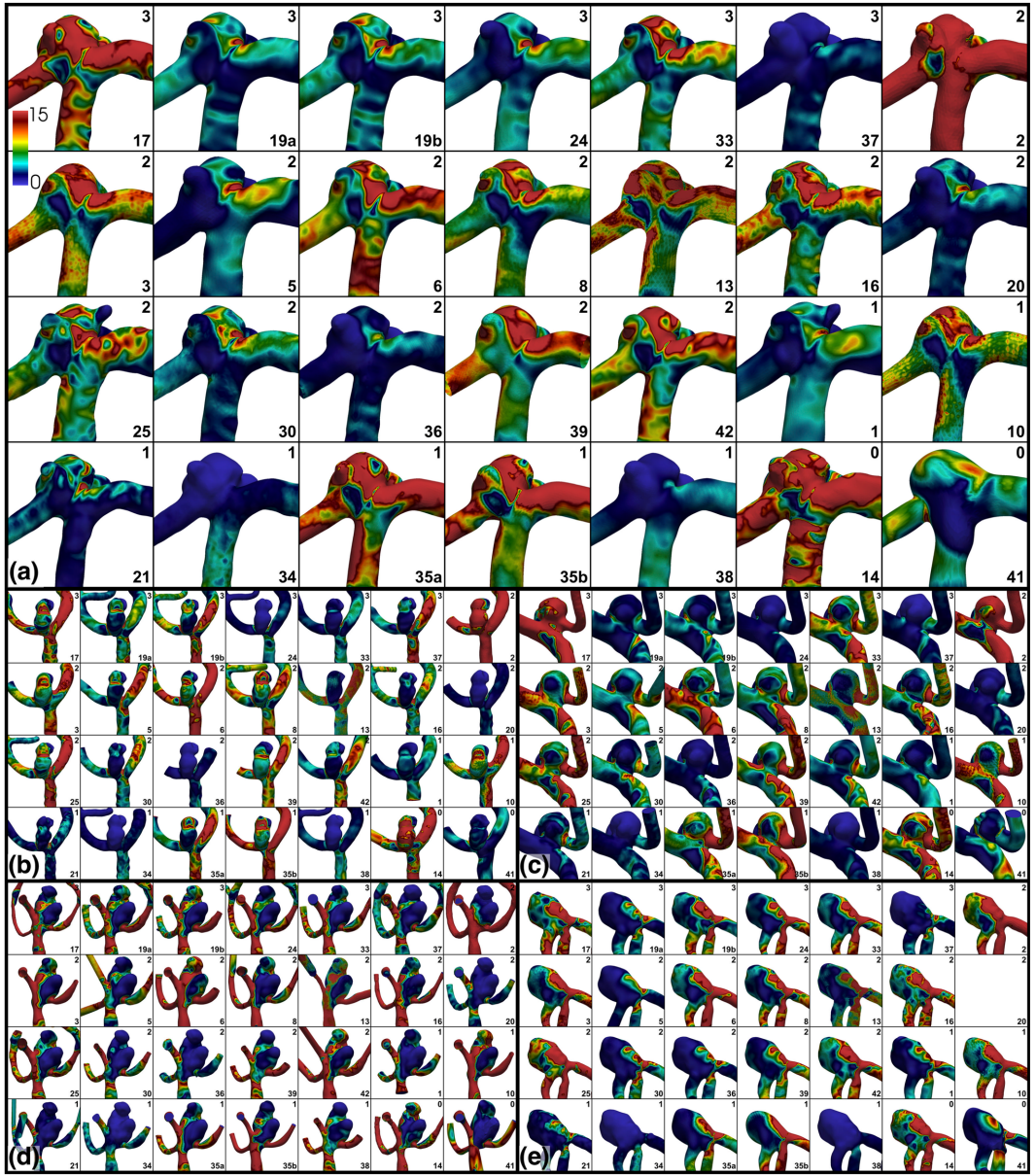


FIGURE 5. Variability of absolute WSS, with (a–e) showing Cases 1–5. WSS values are plotted from 0 to 15 Pa using the colour scale shown in the top left panels. Experience levels and team numbers are shown in each panel, as explained in the caption of Fig. 2.

segmentation, boundary conditions, and CFD. Lumen geometries were highly variable in their morphology, extents and degrees of smoothing, yet while sac WSS magnitudes did vary substantially among teams

(sometimes by orders of magnitude) there appeared to be more consensus regarding sac WSS patterns and relative ranking of cases after normalizing to the parent artery WSS.



FIGURE 6. Variability of normalized WSS\*, with (a–e) showing Cases 1–5. WSS\* values are plotted from 0 to 2 using the colour scale shown in the top left panels, where WSS\* = 1 corresponds to the nominal parent artery value. Experience levels and team numbers are shown in each panel, as explained in the caption of Fig. 2.

Among the factors we could quantify objectively from the submitted data, input parameters like parent artery inflow rates and Reynolds numbers showed non-negligible case-average variabilities (23 and 26%,

respectively), which resulted in variabilities of output hemodynamic parameters that could be higher (e.g., AWSS, 48%) or lower (e.g., AWSS\*, 18%). The former is consistent with that fact that sac WSS should be

**TABLE 3. Descriptive statistics for aneurysm sac WSS parameters, based on team case-average data.**

Experience	<i>N</i>	Median	IQR	CoD (%)
<b>AWSS (Pa)</b>				
All	27	4.57	2.24–6.31	48
High	6	3.26	1.83–5.40	49
Medium	12	5.63	2.91–6.44	38
Low	9	2.77	1.43–6.83	65
<b>AWSS* (–)</b>				
All	27	0.561	0.405–0.583	18
High	6	0.519	0.258–0.634	42
Medium	12	0.561	0.427–0.579	15
Low	9	0.559	0.271–0.649	41
<b>MWSS (Pa)</b>				
All	27	53.9	22.8–64.6	48
High	6	38.0	23.3–53.7	39
Medium	12	59.2	32.3–64.8	33
Low	9	34.5	16.2–69.4	62
<b>MWSS* (–)</b>				
All	27	5.41	3.83–5.94	22
High	6	5.21	4.09–5.53	15
Medium	12	5.58	3.99–6.37	23
Low	9	5.58	2.98–6.74	39
<b>LSA (–)</b>				
All	27	0.083	0.030–0.132	63
High	6	0.091	0.073–0.384	68
Medium	12	0.060	0.026–0.099	58
Low	9	0.052	0.022–0.431	90
<b>LSA* (–)</b>				
All	27	0.145	0.121–0.221	29
High	6	0.166	0.125–0.425	55
Medium	12	0.138	0.120–0.213	28
Low	9	0.153	0.097–0.475	66

proportional to flow rate, which is why normalizing to parent artery WSS, i.e., the latter AWSS\*, typically reduces variability.

Since normalizing essentially renders the WSS *patterns* a function of the parent artery Reynolds number, it is interesting that high variability of Re resulted in lower overall variability of AWSS\*. This echoes a point made at least as early as 2005,<sup>8</sup> namely, that aneurysm flow *patterns* are relatively robust to variations in flow rate (i.e., Re). (However, see “Looking Beyond IQR and CoD” section below for further discussion of this point.) This is encouraging in light of the fact that even good-faith estimations of inflow rates are probably in error relative to the actual—and usually unknown—patient-specific flow rates.<sup>10</sup> With that said, we feel obliged to remind the reader that sac WSS dynamics, and especially high-frequency WSS fluctuations, may be more susceptible to variability in Re.<sup>26</sup>

Visually, there did not seem to be much difference in the variabilities of high vs. medium vs. low experience teams, which was reflected in the lack of significant differences in medians across experience levels. With the exception of the choice of solver (Ansys) and inlet location (ICA), high-experience teams did not show

any more consensus about their image-based CFD pipelines than among other, less experienced teams.

#### *Intra-team Variability*

Although the present study was not designed to systematically separate the influence of segmentation variability from boundary condition or solver variability, we note that two teams (19 and 35) each submitted two CFD datasets which differed only in terms of segmentation and/or smoothing, i.e., the inflow/outflow schemes and CFD solution strategies were the same within each team. For (high-experience) Team 19, automated vs. more intensive manual segmentations were performed, also with differences in the number and lengths of outflow branches. For (low experience) Team 35, two different segmentation software tools were used.

As reported in Table 4, segmentation generally had small influence on case-average MCA diameter, although for Team 35 differences could be as high as 11% for individual cases. Differences in case-average inflow characteristics were less than 10%; however, for individual cases, the imposed flow rate or Re could differ by as much as 38% (Team 19, Case 5). For Team

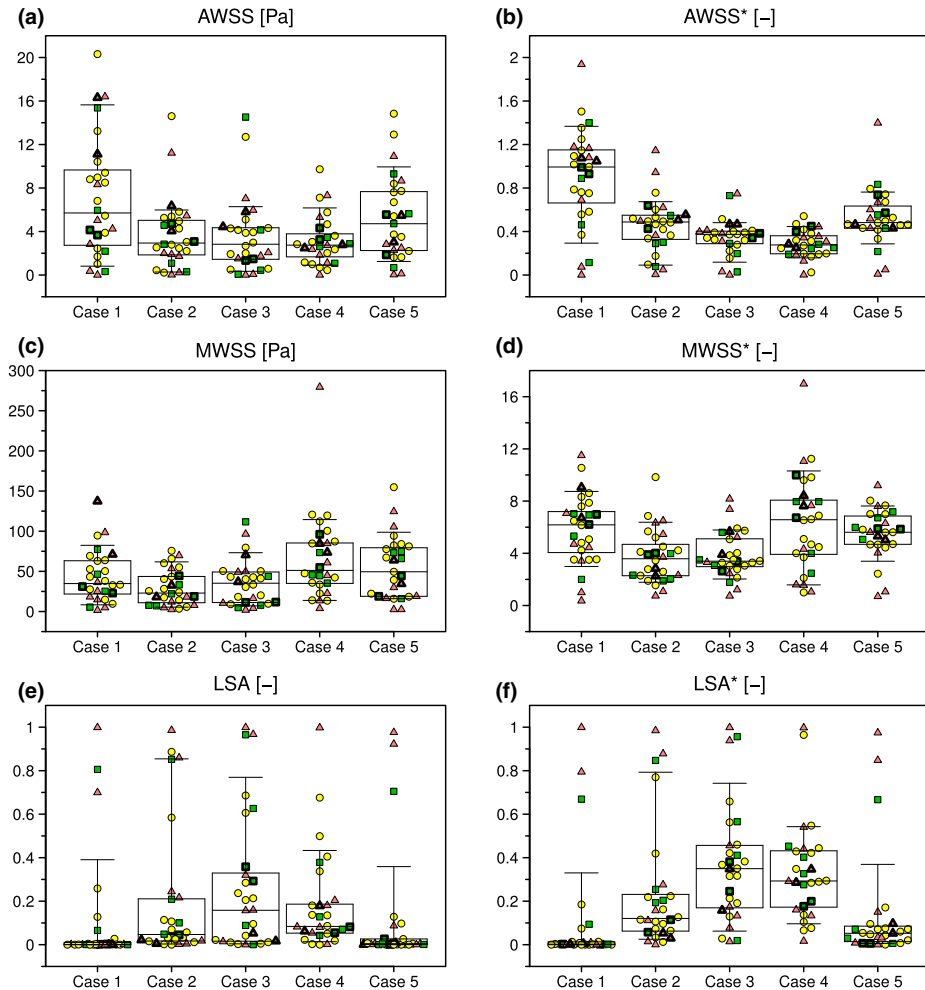


**FIGURE 7.** Variability of selected sac hemodynamic parameters derived as described in the Methods. See caption of Fig. 4 for explanation of symbols and box/whisker plots.

19, there was a 45% difference in case-average calculated MCA WSS between the two segmentations (driven by nearly 80% differences for Case 2 and 5), which is comparable to the *inter-team* CoD = 46% reported in Table 2. For Team 35, however, segmentation had a less dramatic, albeit still non-negligible (20%), effect on MCA WSS. Nevertheless, again for individual cases, MCA WSS could differ between segmentations by up to 65% (Case 5).

Absolute values of sac WSS differed appreciably between the two segmentations for Team 19 (42% for

AWSS, 56% for MWSS, both driven largely by differences for Cases 2 and 5), but these were reduced to 4% and 12% by normalization, suggesting that much of this difference could be attributed to differences in parent artery (inflow) characteristics. For Team 35, sac WSS hardly differed between the two segmentations, except for a 60% difference in LSA, which could be attributed to its already-near-zero values. Taken together, these results indicate that even minor differences in segmentation may non-negligibly affect the commonly reported hemodynamic parameters, espe-

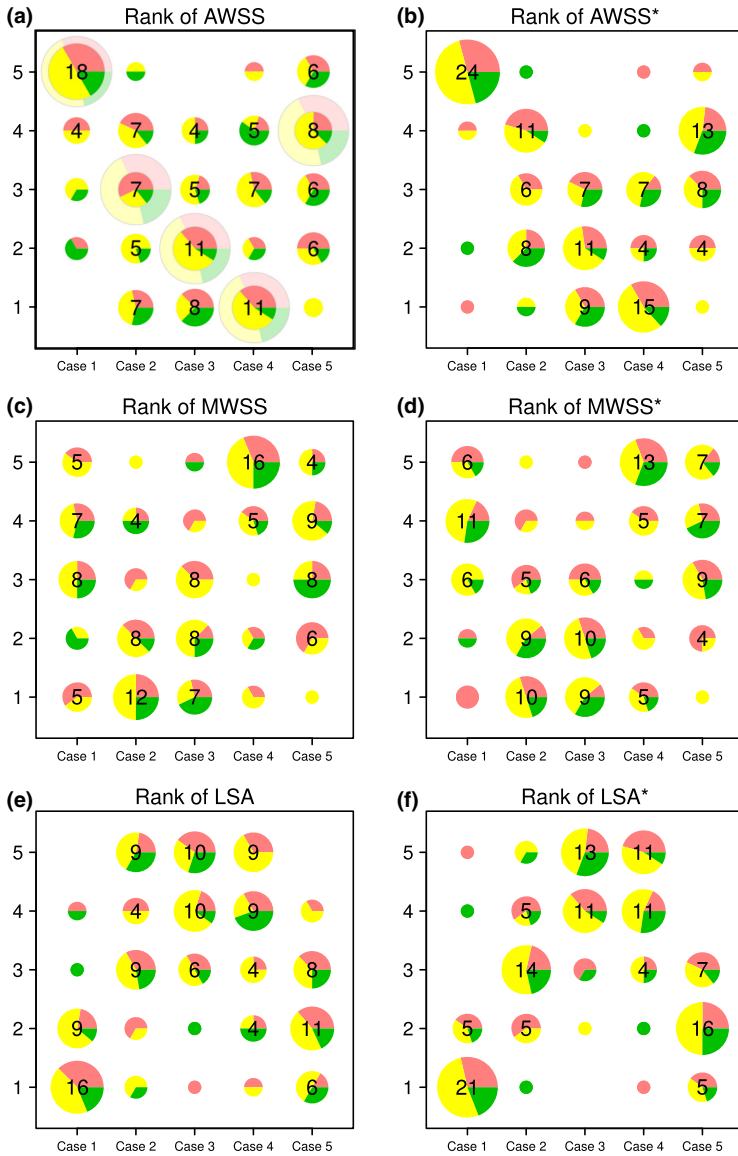


**FIGURE 8.** Variability of team rank-ordering of cases according to the various hemodynamic parameters. In this bubble chart, the number of teams at each rank is proportional to the bubble area, while the proportion of high, medium and low experience teams at each rank is indicated by the green, yellow and red slices. The large, fainter bubbles in the top left panel indicate what one of these charts would look like for perfect agreement among all teams.

cially those based on absolute WSS, and thus *intra-team* variability may appreciably contribute to the *inter-team* variability.

*Reported Vs. Computed Quantities*

As part of the Challenge, teams were asked to report their prescribed inflow rates and sac-averaged WSS for all five cases. Since some teams imposed inflow at the

**TABLE 4. Intra-team variability for input and output parameters, based on team case-average data.**

Parameter	19a	19b	%diff <sup>a</sup>	35a	35b	%diff <sup>a</sup>
MCA diameter (mm)	2.52	2.49	1	2.38	2.42	2
MCA flow rate (mL/s)	1.84	1.99	8	2.72	2.61	4
MCA velocity (cm/s)	38.5	42.3	10	61.1	56.8	7
MCA Reynolds # (-)	270	294	9	385	362	6
MCA Poiseuille WSS (Pa)	4.44	4.91	10	8.25	7.63	8
MCA calculated WSS (Pa)	4.68	7.41	45	9.59	11.7	20
MCA WSS ratio (-)	1.11	1.51	30	1.16	1.57	30
MCA outflow division (-)	0.57	0.55	4	0.63	0.64	< 1
AWSS (Pa)	2.64	4.05	42	6.06	6.31	4
AWSS* (-)	0.597	0.577	4	0.559	0.550	2
MWSS (Pa)	25.5	45.5	56	60.2	64.6	7
MWSS* (-)	5.21	5.90	12	5.79	5.57	4
LSA (-)	0.090	0.091	1	0.045	0.024	60
LSA* (-)	0.103	0.136	28	0.122	0.153	22

$$^a\%diff = |b - a|/avg(b + a).$$

ICA, we were required to calculate parent artery (MCA) flow rates from their submitted velocity field data, as described in the Methods. For teams with MCA inlets, we also calculated their MCA flow rates from their CFD velocity fields, for quality control purposes.

As Fig. 9a shows, there was generally excellent agreement between the reported and calculated MCA flow rates although, for 5 of the 16 teams that reported MCA flow rates, the calculated flow rates disagreed by more than 10%. For Team 8 this could be attributed to outflow from side branches included between the MCA inlet (where their reported flow rates were imposed) and the distal MCA (where our flow rates were calculated). Team 2 imposed plug velocity profiles on what turned out to be the coarsest tetrahedral meshes of any team, and without any boundary layer elements,

so it is possible that the flow rates actually imposed may have been less than the nominal ones reported. Team 5 reported 2 mL/s for all five cases, but appear to have imposed 1 mL/s for Case 5. Regarding Teams 10 and 17, we note that they were among a handful of teams that did not submit vector velocity fields, requiring us to estimate flow rates from their provided velocity magnitudes rather than through-plane velocities we did for other teams; however, as noted in the Methods, this should not have introduced any significant bias.

Figure 9b shows that, for the 22 teams that reported their own AWSS values, there was generally good agreement with the AWSS that we calculated based on a consistent sac clipping plane, suggesting that the impact of sac delineation was generally negligible, at least for AWSS. Nevertheless, for a few teams (3, 24,

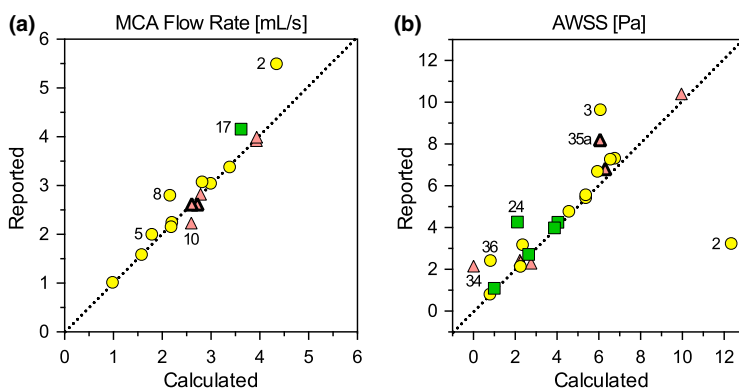


**FIGURE 9. Comparison of calculated vs. reported quantities for (a) MCA flow rate and (b) sac-averaged WSS magnitude, i.e., AWSS. Data points are based on each team's average across the five cases, and team numbers are shown for apparent outliers. See caption of Fig. 4 for explanation of symbols.**

35a, 36) the reported AWSS averaged  $1.5\text{--}3\times$  higher than our calculated value. (Interestingly, Team 35's other submission (35b) showed no such discrepancy). Conversely, Team 2 reported AWSS values that averaged about  $4\times$  lower than what we calculated from their WSS data. The largest discrepancy, however, was for Team 34, which reported AWSS averaging 2.2 Pa, but for which we calculated AWSS averaging 0.012 Pa from their WSS data, a nearly  $200\times$  difference. We initially suspected that this might be a discrepancy in the units of the WSS field provided, but their MCA WSS (calculated from the same WSS surface data) averaged 3.7 Pa, well within what other teams reported.

#### *Outlier and/or Inconsistent Data*

According to published phase-contrast MRI measurements of nearly 100 adults, cycle-averaged blood flow rates in the MCA are  $2.43 \pm 0.52$  mL/s,<sup>50</sup> suggesting a 95th percentile range (i.e., roughly  $\pm 2$  SD) of 1.39–3.47 mL/s. Four teams (2, 14, 17, and 34) were up to 25% above this range, and one team (36) was 30% below. This may not, however, reflect a lack of experience—these teams had a mix of experience levels, from high to low—or knowledge of cerebrovascular flow rates. Three of the teams (2, 14, and 36) provided no specific rationale for their choice of flow rates; however, one team (34) did note that they chose to perform steady flow simulations corresponding to peak-systolic velocity conditions, which was not unreasonable in light of the focus of the Challenge on WSS variability in the context of predicting rupture status. On the other hand, for (high-experience) Team 17, CFD models were segmented proximal to the ICA terminus, but anterior cerebral artery (ACA) branches were not included. This team appeared to impose inflow rates consistent with those for the ICA, meaning that the one third of flow typically directed to the ACA<sup>50</sup> was instead directed into the MCA.

These teams with outlier flow rates also tended to be outliers for hemodynamic parameters. Looking first at MCA WSS (Fig. 4f), Team 2 had values averaging 37 Pa, which was  $\sim 5\times$  the median and  $\sim 2\times$  higher than any other team. While this team did have the highest case-average MCA flow rates (4.34 mL/s), their predicted Poiseuille WSS of 12.8 Pa was not nearly as much of an outlier according to Fig. 4e. Instead, the high MCA WSS appears to have been due to this team's use of plug velocity profile with a relatively short MCA inlet length, whereas most other teams with short MCA segments imposed fully-developed velocity profiles. On the other hand, Team 34, which similarly imposed plug velocity profiles onto CFD models with relatively short MCA inlet lengths, had

comparable Poiseuille WSS (10.7 Pa), but, counter-intuitively, had lower MCA WSS values of only 3.7 Pa (in fact the only team for which this happened), further hinting at a possible inconsistency in the provided WSS surface data (more about this below).

Turning attention to Fig. 7, the highest AWSS was consistently provided by (medium experience) Team 2; however, their AWSS\* values were comparable to those of other teams, which, as noted in the previous section, could be explained by Team 2's high MCA WSS. At the other extreme, (low experience) Team 34 had AWSS averaging 0.012 Pa,  $\sim 400\times$  lower than the median case-average AWSS. (This is not inconsistent with a recent meta-analysis, which reported  $\sim 100\times$  differences in WSS levels across the aneurysm CFD literature.<sup>5</sup>) Consequently, this team's LSA and LSA\* values were also consistently outliers, close to 1.0. This would seem to suggest a possible inconsistency in the units of the provided WSS surface data, yet case-average MWSS for this team was 2.9 Pa, "only"  $\sim 20\times$  lower than the median MWSS value.

This is not to say that only inexperienced teams contributed outlier results. Per Fig. 7a, one high-experience team (17) contributed some of the highest AWSS values for Cases 1 and 3, well in excess of any of the other high-experience team, likely due to their outlier high flow rates as discussed above. At the other end of the scale, Teams 37 (high experience) and 38 (medium experience) had AWSS values at least  $5\times$  lower than the median case-average AWSS, likely due to their flow rates (1.42 and 1.62 mL/s, respectively), which were at the low end of the spectrum. As a result, these teams were consistently among the outliers for LSA and LSA\*. That rank-ordering of cases by the hemodynamic parameters (i.e., Fig. 8) improved consensus suggests that, even if a team over- or underestimated flow rates or WSS, as long as it was being done consistently, the relative ordering of cases by some WSS parameter could be more robust.

Finally, we do not mean to single out some of the above teams as the *only* outliers. Considering the 5 aneurysm cases and 14 (inflow, outflow, and sac) parameters investigated in the present study, every team had data points outside of the 10th–90th percentile range (i.e., "outliers") for at least one of those 70 comparisons, and all teams were outside the IQR for at least 14 of those 70 comparisons. We do note, however, that low-experience teams contributed 43% of the "outlier" data points, compared to 40 and 17% from medium- and high-experience teams, respectively. This is out of proportion to the respective 32, 47 and 21% of all data points contributed by low-, medium- and high-experience teams, and would seem to suggest that, while we found no significant difference in the

data across experience levels, low-experience teams were more likely to contribute outlier data.

### Looking Beyond IQR and CoD

In this study, we focused on IQR and CoD as standard descriptive statistics for datasets having non-parametric distributions. This however, makes it more difficult to compare against the standard deviations (SD) and coefficients of variation (i.e.,  $CoV = SD/mean$ ) typically reported in the literature (albeit often without testing for normality). To give some context, CoD was 23% for case-averaged MCA flow rates, which could be considered negligible or at least tolerable in light of an early report that  $\pm 25\%$  variations in flow rate had only a modest impact of aneurysm flow patterns.<sup>8</sup> This, however, ignores that fact that IQR and CoD include, by definition, only half of the 28 datasets.

Expanding to the 10th and 90th percentiles (the “whiskers” in Figs. 4 and 7) brings in 22 of the 28 datasets. The resulting *inter-decile* range for MCA flow rates is  $2.2\times$ , greater, corresponding to a percent variability of 44%. Similarly, for case-averaged AWSS and AWSS\*, the inter-decile ranges were  $2.2\times$  and  $3.1\times$  wider than their respective IQRs, corresponding to percent variabilities of 85 and 63%, vs. their respective CoDs of 48 and 18%. We therefore recommend some caution in relying solely on IQR and CoD as measures of variability, since they will tend to paint a more optimistic picture of the breadth of the variability. A good rule of thumb for our data would seem to be that  $2 \times IQR$  or  $2 \times CoD$  encompass the variability of most teams.

### Caveats

As noted in the Introduction, the aim of this Challenge was decidedly *not* to separate the impact of the various (and often interacting) input variabilities on output hemodynamic parameters. We attempted this only where we could objectively characterize input parameters like inflow rates or outflow divisions. Those findings seemed to suggest a prominent role for inflow variability on the variability of the chosen hemodynamic parameters, but we cannot say with authority to what extent segmentation or CFD solver/settings variability may have contributed. We also cannot say to what extent inlet location vs. choice of inflow power law may have impacted the variability in prescribed flow rates.<sup>43</sup> Finally, in choosing a consistent location for the parent artery segment, from which derived the MCA velocity, Re, and normalizing WSS, we obscured a potential contribution to the real-world

variability in those input parameters, and in the normalizing of absolute hemodynamic parameters.

Because of the underlying objective of understanding CFD variability in the context of rupture status/risk assessment, we did not require pulsatile simulations, and focused only on the most-common integrated or point-wise hemodynamic parameters, for which steady flow is anyway considered a good proxy for time-averaged pulsatile flow.<sup>35</sup> Thus, our findings cannot be extrapolated to applications where the spatiotemporal fluctuations of WSS may be of interest, e.g., oscillatory shear index (OSI),<sup>49</sup> spectral power index,<sup>26</sup> *etc.* In those cases, the impact of flow rate pulsatility (and CFD solver settings<sup>28</sup>) cannot be overlooked, especially since, as noted in the “Results”, teams that did perform pulsatile CFD employed a wide variety of flow waveform shapes.

We also remind the reader that the reported variabilities are predicated on medians derived from the submitted teams; however, it is not at all clear that the majority should rule. First, while the 26 teams span a wide range of expertises and strategies, their distribution may not be representative of the aneurysm CFD community or published studies as a whole. For example, our Challenge did not attract participants from some of the most well-published aneurysm CFD groups. Second, what constitutes “truth” in image-based aneurysm CFD remains an open question.<sup>24</sup> Even if we were to eliminate variability in segmentations, boundary conditions and CFD solutions, medical imaging can introduce its own distortions, and patient-specific input parameters like flow rates are usually not known, and are anyway subject to their own inherent physiological variations.

Finally, although this Challenge did involve a large amount of data, it was still based on “only” five aneurysms of bifurcation type from a particular cerebrovascular territory. Some caution must therefore be exercised before extrapolating these findings too broadly.

## CONCLUSIONS

Wide variability exists in the prediction of intracranial aneurysm WSS, irrespective of experience with image-based aneurysm CFD. This serves as an impediment to the integration of studies from different groups,<sup>5</sup> a step that may be required in order to achieve statistically significant findings in light of the many factors, other than hemodynamic forces, that influence aneurysm growth and rupture.<sup>37</sup>

Segmentation appears to introduce variability in two ways: (i) morphology and smoothness of the aneurysm sac, neck and parent artery region; and (ii)



inconsistent model extents, making the CFD models more sensitive to inflow and outflow boundary conditions. The impact of the former we can only speculate about, and we appreciate that consensus may be difficult to achieve regarding segmentation methods. (The Multiple Aneurysms Anatomy Challenge (MATCH), announced in early 2018, may help at least address the question of how segmentation variability affects output hemodynamic parameters, since the organizers intend to perform their own consistent CFD on segmentations of five aneurysms provided by the participating teams.) Regarding the latter, our study showed that fully-developed flow was not present in the MCA even when it was far downstream of the (ICA) inlet, suggesting that clipping of the parent artery to within a few diameters of the aneurysm should be strictly avoided. Instead, as previous studies have intimated,<sup>7,19</sup> segmentations should include as much of the proximal vasculature as possible in order to help minimize this unnecessary source of variability.

Inflow rates were demonstrably variable and appeared to drive at least some of the variability among the CFD solutions. While patient-specific flow rates are rarely known, and are anyway subject to normal physiological variability within a given patient, some unnecessary variability in aneurysm CFD may be introduced by the use of outlier flow rates. When patient-specific flow rates are not available, sanity checks on estimated inflow rates and Reynolds numbers can and should be performed against literature values and ranges. Outflow boundary conditions here appeared to have only a minor impact on the variability of outflow divisions, although it is hard to know whether and how these might impact flow and WSS patterns for individual aneurysms,<sup>11</sup> or for cases where more extensive outflow tracts may be included.

Blood properties were also likely a relatively minor source of variability, although differences in input parameters could, in principle, be up to 13% just by virtue of the almost even split between teams using blood viscosities of 3.5 and 4.0 cPoise. While blood properties do vary from patient to patient, and also within patients, this information is not always easily available clinically, especially for retrospective studies. Instead, when patient-specific properties are not available, we suggest that this source of variability, whatever its influence on aneurysm CFD, could easily be removed by standardizing values. We recommend a dynamic viscosity of 3.7 cPoise, which falls neatly between the values that teams typically used, and, with a recommended standard density of 1.06 g/cm<sup>3</sup>, yields a nice round number of 3.5 cStokes for kinematic viscosity.

In this study we did not attempt to separate the influence of CFD solution strategy in light of the many other uncontrolled sources of variability. While studies have shown that CFD solver and mesh/timestep resolutions can have a non-negligible impact on the values of hemodynamic parameters based on point-wise (e.g., MWSS) or time-dependent WSS (e.g., OSI),<sup>14,28</sup> stratification of cases by time-averaged and/or normalized hemodynamic parameters (e.g., AWSS\* or MWSS\*) may be more robust to CFD discretization or solver settings, all other factors being equal.<sup>44</sup> We may therefore speculate that CFD solution strategy was a relatively minor source of variability in the present study.

Finally, our findings show that, whatever the relative contribution of the above-noted individual sources of variability may be, hemodynamic parameters based on normalized rather than absolute WSS have lower variability as a whole. This would seem to suggest that such parameters should be standardized and adopted more widely, at least until we understand better the biological and clinical implications of absolute vs. relative WSS.

In closing, we note that we have only scratched the surface in terms of the analyses that could be done with the rich datasets collected by this Challenge, and so we encourage others to explore the interactions among solution strategies, geometry and hemodynamics using the raw data, surfaces, velocity fields and WSS fields provided in the online data repository.<sup>1</sup>

## FUNDING

This study was supported by grants from the Norges Forskningsråd (179578, 203489/O30, 262827) and the Heart and Stroke Foundation of Canada (MC7455).

## CONFLICTS OF INTEREST

All authors declare that they have no conflicts of interest.

## HUMAN OR ANIMAL STUDIES

No human or animal studies were carried out by the authors for this article. Institutional review board approval was obtained from Wakayama Rosai Hospital for sharing of the anonymized patient images.

## OPEN ACCESS

This article is distributed under the terms of the Creative Commons Attribution 4.0 International License (<http://creativecommons.org/licenses/by/4.0/>), which permits unrestricted use, distribution, and reproduction in any medium, provided you give appropriate credit to the original author(s) and the source, provide a link to the Creative Commons license, and indicate if changes were made.

## REFERENCES

- <sup>1</sup>Valen-Sendstad, K., A. W. Bergersen, K. Kono, and D. A. Steinman. Data for the 2015 International Aneurysm CFD Challenge. <https://doi.org/10.6084/m9.figshare.6383516.v2>. Accessed 30 August 2018.
- <sup>2</sup>Bazilevs, Y., M. C. Hsu, Y. Zhang, W. Wang, T. Kvamsdal, S. Hentschel, *et al.* Computational vascular fluid–structure interaction: methodology and application to cerebral aneurysms. *Biomech. Model. Mechanobiol.* 9:481–498, 2010.
- <sup>3</sup>Berg, P., C. Roloff, O. Beuing, S. Voss, S. Sugiyama, N. Aristokleous, *et al.* The computational fluid dynamics rupture challenge 2013—phase II: variability of hemodynamic simulations in two intracranial aneurysms. *J. Biomech. Eng.* 137(12):121008, 2015.
- <sup>4</sup>Berg, P., S. Saalfeld, S. Voss, T. Redel, B. Preim, G. Janiga, *et al.* Does the DSA reconstruction kernel affect hemodynamic predictions in intracranial aneurysms? An analysis of geometry and blood flow variations. *J. Neurointerv. Surg.* 10(3):290–296, 2018.
- <sup>5</sup>Can, A., and R. Du. Association of hemodynamic factors with intracranial aneurysm formation and rupture: systematic review and meta-analysis. *Neurosurgery* 78(4):510–520, 2016.
- <sup>6</sup>Castro, M. A., M. C. Ahumada Olivares, C. M. Putman, and J. R. Cebral. Unsteady wall shear stress analysis from image-based computational fluid dynamic aneurysm models under Newtonian and Casson rheological models. *Med. Biol. Eng. Comput.* 52(10):827–839, 2014.
- <sup>7</sup>Castro, M. A., C. M. Putman, and J. R. Cebral. Computational fluid dynamics modeling of intracranial aneurysms: effects of parent artery segmentation on intraneurysmal hemodynamics. *Am. J. Neuroradiol.* 27(8):1703–1709, 2006.
- <sup>8</sup>Cebral, J. R., M. A. Castro, S. Appanaboyina, C. M. Putman, D. Millan, and A. F. Frangi. Efficient pipeline for image-based patient-specific analysis of cerebral aneurysm hemodynamics: technique and sensitivity. *IEEE Trans. Med. Imaging* 24(4):457–467, 2005.
- <sup>9</sup>Cebral, J. R., F. Mut, J. Weir, and C. Putman. Quantitative characterization of the hemodynamic environment in ruptured and unruptured brain aneurysms. *Am. J. Neuroradiol.* 32(1):145–151, 2011.
- <sup>10</sup>Chnafa, C., P. Bouillot, O. Brina, B. M. A. Delattre, M. I. Vargas, K. O. Lovblad, *et al.* Vessel calibre and flow splitting relationships at the internal carotid artery terminal bifurcation. *Physiol. Meas.* 38(11):2044–2057, 2017.
- <sup>11</sup>Chnafa, C., O. Brina, V. M. Pereira, and D. A. Steinman. Better than nothing: a rational approach for minimizing the impact of outflow strategy on cerebrovascular simulations. *Am. J. Neuroradiol.* 39(2):337–343, 2018.
- <sup>12</sup>Dempere-Marco, L., E. Oubel, M. Castro, C. Putman, A. Frangi, and J. Cebral. CFD analysis incorporating the influence of wall motion: application to intracranial aneurysms. *Med. Image Comput. Assist. Interv.* 9(Pt 2):438–445, 2006.
- <sup>13</sup>Dennis, K. D., D. F. Kallmes, and D. Dragomir-Daescu. Cerebral aneurysm blood flow simulations are sensitive to basic solver settings. *J. Biomech.* 57:46–53, 2017.
- <sup>14</sup>Evju, O., J. M. Pozo, A. F. Frangi, and K. A. Mardal. Robustness of common hemodynamic indicators with respect to numerical resolution in 38 middle cerebral artery aneurysms. *PLoS ONE* 12(6):e0177566, 2017.
- <sup>15</sup>Firouzian, A., R. Manniesing, Z. H. Flach, R. Risselada, F. van Kooten, M. C. J. M. Sturkenboom, *et al.* Intracranial aneurysm segmentation in 3D CT angiography: method and quantitative validation with and without prior noise filtering. *Eur. J. Radiol.* 79(2):299–304, 2011.
- <sup>16</sup>Geers, A. J., I. Larrabide, A. G. Radaelli, H. Bogunovic, M. Kim, H. A. G. van Andel, *et al.* Patient-specific computational hemodynamics of intracranial aneurysms from 3D rotational angiography and CT angiography: an in vivo reproducibility study. *Am. J. Neuroradiol.* 32(3):581–586, 2011.
- <sup>17</sup>Goubergrits, L., J. Schaller, U. Kertzscher, C. Petz, H. C. Hege, and A. Spuler. Reproducibility of image-based analysis of cerebral aneurysm geometry and hemodynamics: an in vitro study of magnetic resonance imaging, computed tomography, and three-dimensional rotational angiography. *J. Neurol. Surg. A* 74(5):294–302, 2013.
- <sup>18</sup>Hassan, T., E. V. Timofeev, M. Ezura, T. Saito, A. Takahashi, K. Takayama, *et al.* Hemodynamic analysis of an adult vein of Galen aneurysm malformation by use of 3D image-based computational fluid dynamics. *Am. J. Neuroradiol.* 24(6):1075–1082, 2003.
- <sup>19</sup>Hodis, S., S. Kargar, D. F. Kallmes, and D. Dragomir-Daescu. Artery length sensitivity in patient-specific cerebral aneurysm simulations. *Am. J. Neuroradiol.* 36(4):737–743, 2015.
- <sup>20</sup>Janiga, G., P. Berg, S. Sugiyama, K. Kono, and D. A. Steinman. The computational fluid dynamics rupture challenge 2013-phase I: prediction of rupture status in intracranial aneurysms. *Am. J. Neuroradiol.* 36(3):530–536, 2015.
- <sup>21</sup>Jansen, I. G., J. J. Schneiders, W. V. Potters, P. van Ooij, R. van den Berg, E. van Bavel, *et al.* Generalized versus patient-specific inflow boundary conditions in computational fluid dynamics simulations of cerebral aneurysmal hemodynamics. *Am. J. Neuroradiol.* 35(8):1543–1548, 2014.
- <sup>22</sup>Jou, L. D., C. M. Quick, W. L. Young, M. T. Lawton, R. Higashida, A. Martin, *et al.* Computational approach to quantifying hemodynamic forces in giant cerebral aneurysms. *Am. J. Neuroradiol.* 24(9):1804–1810, 2003.
- <sup>23</sup>Kadasi, L. M., W. C. Dent, and A. M. Malek. Colocalization of thin-walled dome regions with low hemodynamic wall shear stress in unruptured cerebral aneurysms. *J. Neurosurg.* 119(1):172–179, 2013.
- <sup>24</sup>Kallmes, D. F. Identifying “truth” in computational fluid dynamics research. *Am. J. Neuroradiol.* 32(6):E122, 2011; (Author reply E3).
- <sup>25</sup>Karmonik, C., C. Yen, O. Diaz, R. Klucznik, R. G. Grossman, and G. Benndorf. Temporal variations of wall shear stress parameters in intracranial aneurysms—importance of patient-specific inflow waveforms for CFD calcu-

- lations. *Acta Neurochir.* 152(8):1391–1398, 2010; (Discussion 8).
- <sup>26</sup>Khan, M. O., C. Chnafa, D. Gallo, F. Molinari, U. Morbiducci, D. A. Steinman, *et al.* On the quantification and visualization of transient periodic instabilities in pulsatile flows. *J. Biomech.* 52:179–182, 2017.
- <sup>27</sup>Khan, M. O., D. A. Steinman, and K. Valen-Sendstad. Non-Newtonian versus numerical rheology: practical impact of shear-thinning on the prediction of stable and unstable flows in intracranial aneurysms. *Int. J. Numer. Method Biomed. Eng.* 33:e2836, 2016.
- <sup>28</sup>Khan, M. O., K. Valen-Sendstad, and D. A. Steinman. Narrowing the expertise gap for predicting intracranial aneurysm hemodynamics: Impact of solver numerics versus mesh and time-step resolution. *Am. J. Neuroradiol.* 36(7):1310–1316, 2015.
- <sup>29</sup>Malek, A. M., S. L. Alper, and S. Izumo. Hemodynamic shear stress and its role in atherosclerosis. *JAMA* 282(21):2035–2042, 1999.
- <sup>30</sup>Marzo, A., P. Singh, P. Reymond, N. Stergiopoulos, U. Patel, and R. Hose. Influence of inlet boundary conditions on the local haemodynamics of intracranial aneurysms. *Comput. Methods Biomech. Biomed. Eng.* 12(4):431–444, 2009.
- <sup>31</sup>Meng, H., V. M. Tutino, J. Xiang, and A. Siddiqui. High WSS or low WSS? Complex interactions of hemodynamics with intracranial aneurysm initiation, growth, and rupture: toward a unifying hypothesis. *Am. J. Neuroradiol.* 35(7):1254–1262, 2014.
- <sup>32</sup>Morales, H. G., and O. Bonnefous. Unraveling the relationship between arterial flow and intra-aneurysmal hemodynamics. *J. Biomech.* 48(4):585–591, 2015.
- <sup>33</sup>Piccinelli, M., A. Veneziani, D. A. Steinman, A. Remuzzi, and L. Antiga. A framework for geometric analysis of vascular structures: application to cerebral aneurysms. *IEEE Trans. Med. Imaging* 28(8):1141–1155, 2009.
- <sup>34</sup>Ren, Y., G. Z. Chen, Z. Liu, Y. Cai, G. M. Lu, and Z. Y. Li. Reproducibility of image-based computational models of intracranial aneurysm: a comparison between 3D rotational angiography, CT angiography and MR angiography. *Biomed. Eng. Online* 15(1):50, 2016.
- <sup>35</sup>Retarekar, R., M. Ramachandran, B. Berkowitz, R. E. Harbaugh, D. Hasan, R. H. Rosenwasser, *et al.* Stratification of a population of intracranial aneurysms using blood flow metrics. *Comput. Methods Biomech. Biomed. Eng.* 18(10):1072–1082, 2015.
- <sup>36</sup>Robertson, A. M., and P. N. Watton. Computational fluid dynamics in aneurysm research: critical reflections, future directions. *Am. J. Neuroradiol.* 33(6):992–995, 2012.
- <sup>37</sup>Schneiders, J. J., H. A. Marquering, P. van Ooij, R. van den Berg, A. J. Nederveen, D. Verbaan, *et al.* Additional value of intra-aneurysmal hemodynamics in discriminating ruptured versus unruptured intracranial aneurysms. *Am. J. Neuroradiol.* 36(10):1920–1926, 2015.
- <sup>38</sup>Sen, Y., Y. Qian, A. Avolio, and M. Morgan. Image segmentation methods for intracranial aneurysm hemodynamic research. *J. Biomech.* 47(5):1014–1019, 2014.
- <sup>39</sup>Sforza, D. M., C. M. Putman, and J. R. Cebral. Computational fluid dynamics in brain aneurysms. *Int. J. Numer. Methods Biomed. Eng.* 28(6–7):801–808, 2011.
- <sup>40</sup>Steinman, D. A. Computational modeling and flow diverters: a teaching moment. *Am. J. Neuroradiol.* 32(6):981–983, 2011.
- <sup>41</sup>Steinman, D. A., Y. Hoi, P. Fahy, L. Morris, M. T. Walsh, N. Aristokleous, *et al.* Variability of computational fluid dynamics solutions for pressure and flow in a giant aneurysm: the ASME 2012 Summer Bioengineering Conference CFD Challenge. *J. Biomech. Eng.* 135(2):021016, 2013.
- <sup>42</sup>Steinman, D. A., J. S. Milner, C. J. Norley, S. P. Lownie, and D. W. Holdsworth. Image-based computational simulation of flow dynamics in a giant intracranial aneurysm. *Am. J. Neuroradiol.* 24(4):559–566, 2003; (Commentary 3–4).
- <sup>43</sup>Valen-Sendstad, K., M. Piccinelli, R. Krishnankutty Rema, and D. A. Steinman. Estimation of inlet flow rates for image-based aneurysm CFD models: where and how to begin? *Ann. Biomed. Eng.* 43(6):1422–1431, 2015.
- <sup>44</sup>Valen-Sendstad, K., and D. A. Steinman. Mind the gap: impact of computational fluid dynamics solution strategy on prediction of intracranial aneurysm hemodynamics and rupture status indicators. *Am. J. Neuroradiol.* 35(3):536–543, 2014; (Commentary 44–45).
- <sup>45</sup>Varble, N., J. Xiang, N. Lin, E. Levy, and H. Meng. Flow instability detected by high-resolution computational fluid dynamics in fifty-six middle cerebral artery aneurysms. *J. Biomech. Eng.* 138(6):061009, 2016.
- <sup>46</sup>Voss, S., S. Glasser, T. Hoffmann, O. Beuing, S. Weigand, K. Jachau, *et al.* Fluid-structure simulations of a ruptured intracranial aneurysm: constant versus patient-specific wall thickness. *Comput. Math. Methods Med.* 2016:9854539, 2016.
- <sup>47</sup>Xiang, J., S. K. Natarajan, M. Tremmel, D. Ma, J. Mocco, L. N. Hopkins, *et al.* Hemodynamic-morphologic discriminants for intracranial aneurysm rupture. *Stroke* 42(1):144–152, 2011.
- <sup>48</sup>Xiang, J., M. Tremmel, J. Kolega, E. I. Levy, S. K. Natarajan, and H. Meng. Newtonian viscosity model could overestimate wall shear stress in intracranial aneurysm domes and underestimate rupture risk. *J. Neurointerv. Surg.* 4(5):351–357, 2012.
- <sup>49</sup>Xiang, J., J. Yu, K. V. Snyder, E. I. Levy, A. H. Siddiqui, and H. Meng. Hemodynamic-morphological discriminant models for intracranial aneurysm rupture remain stable with increasing sample size. *J. Neurointerv. Surg.* 8(1):104–110, 2014.
- <sup>50</sup>Zarrinkoob, L., K. Ambarki, A. Wahlin, R. Birgander, A. Eklund, and J. Malm. Blood flow distribution in cerebral arteries. *J. Cereb. Blood Flow Metab.* 35(4):648–654, 2015.



### **III. Automated and objective removal of bifurcation aneurysms: Incremental improvements, and validation against healthy controls**







Contents lists available at ScienceDirect

Journal of Biomechanics

journal homepage: [www.elsevier.com/locate/jbiomech](http://www.elsevier.com/locate/jbiomech)  
[www.JBimech.com](http://www.JBimech.com)

Short communication

## Automated and objective removal of bifurcation aneurysms: Incremental improvements, and validation against healthy controls



Aslak W. Bergersen<sup>a</sup>, Christophe Chnafa<sup>b</sup>, Diego Gallo<sup>c</sup>, Marina Piccinelli<sup>d</sup>, David A. Steinman<sup>b</sup>, Kristian Valen-Sendstad<sup>a,\*</sup>

<sup>a</sup> Department of Computational Physiology, Simula Research Laboratory, Lysaker, Norway<sup>b</sup> Department of Mechanical and Industrial Engineering, University of Toronto, Toronto, ON, Canada<sup>c</sup> Department of Mechanical and Aerospace Engineering, Politecnico di Torino, Torino, Italy<sup>d</sup> Department of Radiology and Imaging Sciences, Emory University, GA, USA

## ARTICLE INFO

## Article history:

Accepted 11 September 2019

## Keywords:

Mechanobiology  
Wall shear stress  
Wall shear stress gradients  
Aneurysm pathogenesis  
Subarachnoid hemorrhage

## ABSTRACT

Abnormal hemodynamic stresses are thought to correlate with aneurysm initiation, growth, and rupture. We have previously investigated the role of wall shear stress (WSS) and WSS gradients (WSSG) in search for a mechanistic link to formation of sidewall aneurysms using an automated and objective tool for aneurysm removal and arterial reconstruction in combination with computational fluid dynamics (CFD). However, we warned against the use of the tool for bifurcation type aneurysms because of a potential unrealistic reconstruction of the apex. We hypothesized that inclusion of additional morphological features from the surrounding vasculature could overcome these constraints. We extended the previously published method for removal and reconstruction of the bifurcation vasculature based on diverging and converging points of the parent and daughter artery centerlines, to also include two new centerlines between the daughter vessels, one of them passed through the bifurcation center. Validation was performed by comparing the efficacy of the two algorithms, using ten healthy models of the internal carotid artery terminus as ground truth. Qualitative results showed that the bifurcation apices became smoother relative to the original algorithm; more consistent with the reference models. This was reflected quantitatively by a reduced maximum distance between the reference and reconstructed surfaces, although not statistically significant. Furthermore, the modified algorithm also quantitatively improved CFD derived WSS and WSSG, especially the latter. In conclusion, the modified algorithm does not perfectly reconstruct the bifurcation apex, but provides an incremental improvement, especially important for the derived hemodynamic metrics of interest in vascular pathobiology.

© 2019 Elsevier Ltd. All rights reserved.

### 1. Introduction

Rupture of an intracranial aneurysm is the most common cause of subarachnoid hemorrhage (Wiebers et al., 2003). The vast majority of aneurysms are asymptomatic and incidentally detected when patients undergo neuroimaging for unrelated reasons. However, risk of clinical intervention can exceed the natural risk of rupture, which is as low as 1% annually (Rinkel et al., 1998) making optimal patient-specific treatment decisions difficult. Morphological indices have historically been used clinically for risk of rupture stratification (Raghavan et al., 2005), but aneurysm morphology and size are ultimately surrogates for hemodynamically induced wall shear stress (WSS) that contribute to vessel wall adaptation,

remodeling, and vascular pathogenesis (Malek et al., 1999; Morbiducci et al., 2016). Medical image-based computational fluid dynamics (CFD) (Taylor and Steinman, 2010) has been extensively used in the investigation of vascular pathology, e.g., retrospectively correlating flow phenotypes and stresses with aneurysm rupture status in search for prospective clinical use (Xiang et al., 2011; Cebal et al., 2011).

However, 'predicting' aneurysm rupture status in large databases with a retrospectively known clinical outcome can be problematic for a number of reasons. Aneurysm rupture is an event that may change both morphology and size (Schneiders et al., 2014; Skodvin et al., 2017), only certain aneurysms have endothelial cells (Frösen et al., 2004), and the aneurysm wall has a different structure compared to healthy arteries (Canham et al., 1999). Additionally, there are uncertainties related to modeling of aneurysm flows, like neck size overestimation with 3D rotational angiography

\* Corresponding author.

E-mail address: [kvs@simula.no](mailto:kvs@simula.no) (K. Valen-Sendstad).

(Schneiders et al., 2013), image segmentation, which is both laborious and operator-dependent (Valen-Sendstad et al., 2018), and numerical solution strategies (Valen-Sendstad and Steinman, 2014; Khan et al., 2015). Therefore, studying the fundamental role of hemodynamics in aneurysms might be more intricate than originally anticipated. However, since the same stimuli (WSS/WSSG) are believed to be involved in aneurysm initiation (Gao et al., 2008; Kulcsár et al., 2011), growth (Sugiyama et al., 2012; Francis et al., 2013), and rupture (Cebal et al., 2005; Xiang et al., 2011), one can investigate the hemodynamic stimulus and vascular response before aneurysms have formed, without the aforementioned limitations. Hence, studying aneurysm initiation can provide mechanistic links that are paramount for understanding fundamental vascular remodeling.

Ford et al. (Ford et al., 2009) developed a tool for objective aneurysm removal and arterial reconstruction for investigating the plausible hemodynamic stimulus prior to sidewall aneurysm formation. They also warned about the application to bifurcation aneurysms, and clearly stated that the tool 'remains to be verified'. The latter is difficult because medical images of the pre-aneurysmal vasculature are rarely available. Secondly, the high-resolution contrast-based computed tomography images needed to adequately reconstruct a bifurcation apex, can naturally not be obtained from healthy individuals to limit potentially harmful radiation (Hendee and O'Connor, 2012). From previous usage of the tool developed by Ford et al., for instance applied to sidewall aneurysms Valen-Sendstad et al. (2014) we hypothesized that

the bifurcation apex was occasionally reconstructed with an artificial "notch" at the apex. We, therefore, proposed a technical improvement to the original algorithm. We also acquired access to segmentation of intracranial blood vessels in ten patients that underwent neurointensive care where no vascular abnormalities were found, which enabled validation. The latter is indeed the only possible solution since the vasculature is unknown in the presence of an aneurysm, which the algorithm actually is independent of. The aim of the study was to reconstruct an artificially removed bifurcation, and compare the results of the two reconstruction algorithms to the reference and *a priori* known bifurcation surface, especially focusing on relevant CFD derived stresses. In the following, we will refer to the bifurcation surfaces as *reference*, *Ford*, and *modified* corresponding to the unmodified healthy surface, the reconstructed surface from Ford et al., and our modified algorithm, respectively.

## 2. Methods

### 2.1. Parent artery and bifurcation reconstruction

We acquired access to 3D angiograms from ten patients that underwent neurointensive care where no vascular abnormalities were found, originally collected for the open-source Aneurisk database, and subsequently made publicly available (Aneurisk-Team, 2012). Fig. 1 is adapted from Ford et al. and outlines the algorithm for intracranial aneurysm removal and parent artery

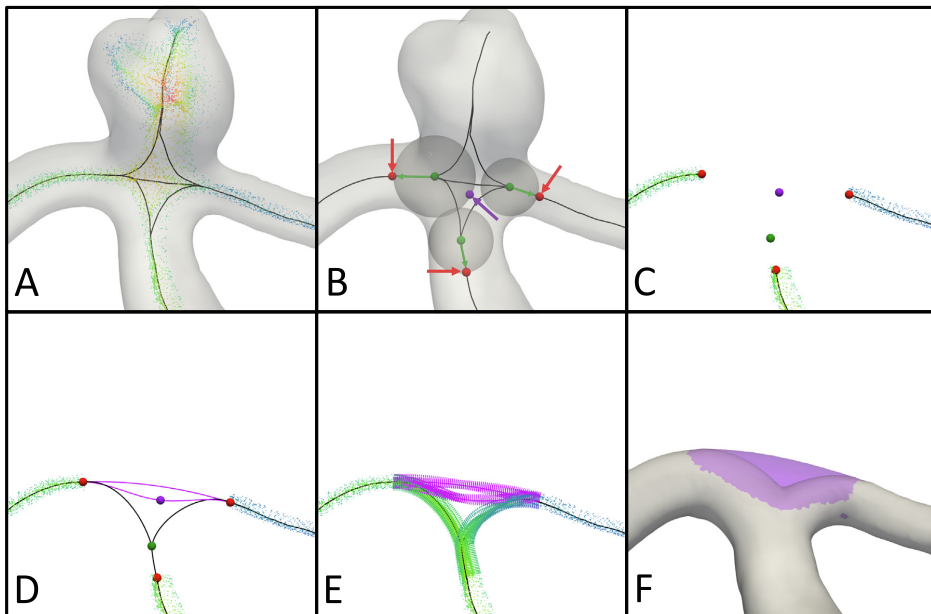


**Fig. 1.** Illustration of the algorithm for removing a bifurcation aneurysm. The additions to the algorithm, relative to Ford et al., is highlighted in purple. Note that to ease comparison with Ford et al. we here illustrate the algorithm on the same model, but for the remainder of the paper we are applying the algorithm to bifurcations without aneurysms for validation purposes. **Step A**, compute the Voronoi diagram and five centerlines; two from the parent artery to each daughter branch, two from each daughter branch to the aneurysm sac, and one between the two daughter branches. **Step B**, the green dots are located where the centerlines coordinates diverge; referred to as diverging points, and the arithmetic mean of the coordinates of these is defined as the bifurcation center location, shown in purple. The diverging points are then moved one radius of the local minimal inscribed sphere away from the bifurcation center along the centerlines, as indicated by the green arrows; now referred to as clipping points. **Step C**, subtract the centerlines and Voronoi diagram that are located in between the clipping points. **Step D**, create a total of four new centerlines, two of which are passed through the diverging point from the parent artery to the daughter branches using third order splines. The remaining two start and end at the daughter branches, where one of them is passed through the bifurcation center. **Step E**, extrapolate the old Voronoi diagram along the new centerlines. **Step F**, envelope the Voronoi diagram to create a new surface. (For interpretation of the references to colour in this figure legend, the reader is referred to the web version of this article.)



reconstruction. Note that we here illustrate the algorithm using the same model as in Ford et al., but that we here apply the algorithm to models without aneurysms only. Briefly, the algorithm is based on manipulating the Voronoi diagram, which is an alternative representation of a surface (Piccinelli et al., 2009), and associated centerlines, to both remove and reconstruct the bifurcation. Details are provided in the caption of Fig. 1. The main difference between the original and the modified algorithm is that the Voronoi diagram is interpolated onto two new centerlines between the daughter vessels, these changes are colored purple in Fig. 1.

## 2.2. CFD, wall shear stress, and wall shear stress gradients

CFD simulations were performed to investigate the effects of the reconstruction algorithms on hemodynamic stresses. The Vascular Modelling ToolKit (Antiga et al., 2008) was used to extend the inlet and outlets five times the local radius, and create meshes that on average consisted of three million tetrahedron cells with four boundary layers, previously demonstrated to be sufficient to resolve WSS (Khan et al., 2015). Pulsatile CFD simulations were performed assuming blood to behave as a Newtonian fluid (Khan et al., 2017) using the Oasis solver (Mortensen and Valen-Sendstad, 2015), designed to obtain a solution that preserves kinetic energy while minimizing numerical dispersion and diffusion errors, taking 10,000 time steps per cycle with a period of 0.951s using an older adult waveform (Hoi et al., 2010). We specified a fully developed Womersley velocity profile at the inlet and a time-averaged cross-sectional mean velocity of 0.27 m/s (Valen-Sendstad et al., 2015) with a flow splitting approach for the outflow boundary as detailed in (Chnafa et al., 2018).

The efficacy of the reconstruction algorithms was quantified with respect to the mean and maximum distance, curvature, WSS, and WSSG; measured relatively to the reference surface or

associated CFD simulations. All metrics were computed along the intersection between the objectively defined bifurcation plane (Piccinelli et al., 2011) and surface, see white lines in Fig. 3A, now referred to as *bifurcation lines*. To quantitatively measure the differences, we sampled WSS and WSSG along the normalized bifurcation line, and used a spline representation to compute the maximum curvature, a metric describing the bifurcation apex "notch". A one-sided paired t-test was used to check if the modified method performed significantly better, setting the level of significance to  $p$ -value < 0.05, not adjusting for multiple tests.

## 3. Results

### 3.1. Parent artery and bifurcation reconstruction

Fig. 2 shows models 1–5 of the reference surface in white with the results of the original and modified surface reconstruction algorithms colored in red in sub-plots A and B, respectively, all in opaque. We have zoomed into model 1 to better highlight the differences. These qualitative results arguably show that the modified algorithm produce reconstructed surfaces closer to the reference surface, most importantly at the apex of the bifurcation. That is, the modified algorithm does not produce the same artificial "notch", especially apparent in the models 1, 2, 4, and 5 shown in Fig. 2A. The remaining five models are shown in the Appendix with broadly consistent results.

### 3.2. Hemodynamic metrics: Wall shear stress and wall shear stress gradients

Focusing now on qualitative CFD derived results, Fig. 3A shows bifurcation WSS maps obtained on the modified, reference, and Ford surfaces, respectively. The WSS maps show largely similar

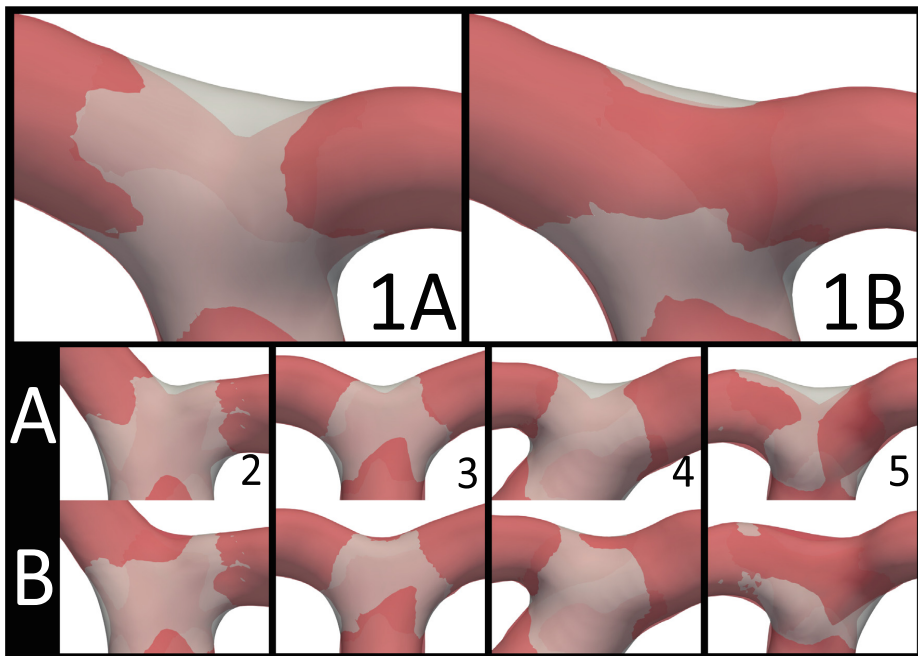
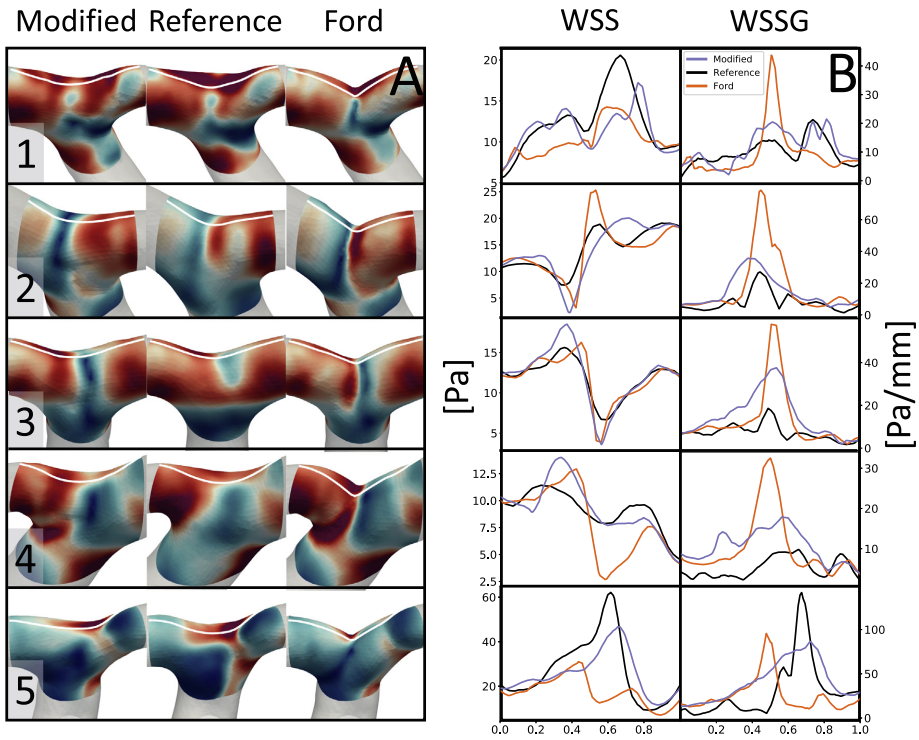


Fig. 2. The figure shows the reference surface in opaque, with the results from the original and modified surface reconstruction algorithms colored in red in sub-plots A and B, respectively. (For interpretation of the references to colour in this figure legend, the reader is referred to the web version of this article.)



**Fig. 3.** **A** Wall shear stress (WSS) maps from computational fluid dynamic simulations of the modified, reference, and Ford models, from left to right, respectively, and bifurcation lines shown in white. The absolute values of the WSS are indicated in the panel to the right. **B** WSS and WSSG along the bifurcation lines where the colors black, orange, and blue refers to the modified, reference, and Ford models, respectively. (For interpretation of the references to colour in this figure legend, the reader is referred to the web version of this article.)

global trends, but with clearly visible differences at the bifurcation apex. This is further highlighted by the corresponding WSS and WSSG values along the bifurcation lines shown in Fig. 3B; especially WSSG is overestimated by the original algorithm. The remaining five models are shown in the Appendix with broadly consistent result.

Table 1 shows quantitative results and demonstrates that both the curvature, WSS, and WSSG were significantly closer to the reference values, with *p*-values < 0.05 marked in bold. The maximum

distance between the reference and reconstructed surfaces was also reduced with the modified algorithm, although not statistically significant.

#### 4. Discussion

We have shown that a minor modification of Ford et al.'s algorithm can reconstruct arterial bifurcations that are more consistent with the reference bifurcation obtained from state-of-the-art med-

**Table 1**  
The table shows quantitative result based on the error measurements between the reference surface versus those obtained from the original and modified algorithms, respectively. *p*-values below 0.05 % are marked in bold.

Metric	Measure	Mean absolute error (SD)		<i>p</i> -value
		Ford	Modified	
Distance [mm]	Average	0.06 (0.03)	0.06 (0.04)	0.408
	Max	0.30 (0.15)	0.19 (0.11)	0.076
Curvature [ $\frac{1}{\text{mm}}$ ]	Max	2.03 (0.48)	0.24 (0.26)	<b>&lt;0.001</b>
WSS [Pa]	Average	7.27 (11.02)	5.63 (8.73)	<b>0.037</b>
	Max	17.57 (22.33)	12.90 (16.66)	0.081
WSSG [Pa/mm]	Average	12.54 (8.23)	9.41 (5.49)	<b>0.012</b>
	Max	50.22 (29.40)	26.82 (17.47)	<b>0.001</b>

ical images. As a result, the computed WSS and WSSG from the reconstructed surfaces are statistically and phenotypically improved compared to the original algorithm. Since the vast majority of aneurysms are located in bifurcations, the modified algorithm could increase the number of subjects, increase the rigor of aneurysm initiation research, and accelerate our understanding of fundamental vascular pathobiology. The latter can ultimately contribute to further advances in research on aneurysm risk of rupture.

We have previously shown that there is relatively high intra- and interlaboratory uncertainty in segmentation of intracranial arteries (Valen-Sendstad et al., 2018). To reduce the uncertainty in the segmentation we chose to focus on the ICA terminus since it is the largest intracranial artery, and is therefore the least sensitive to segmentation errors because of the high voxel-to-vessel ratio. However, we have also compared the geometrical metrics of middle- and anterior cerebral artery bifurcations and obtained equivalent results for the maximum curvature (average absolute errors of 2.09 and 0.52 [ $\frac{1}{mm}$ ] using the Ford and modified algorithm, respectively,  $p$ -value < 0.001). These results, however, are associated with higher uncertainties due to the smaller voxel-to-vessel ratio. Hence, a limitation is that validation has just been performed on ten models. Another “feature” associated with the current methods is namely that neither algorithms were designed or capable to reproduce a proximal stenosis, as observed in model 7, see Fig. 5 of the Appendix. Both algorithms produced a too wide arterial segment at the stenosis location, which resulted in a lower WSS/WSSG, relative to the reference model. The quantitative results are admittedly sensitive to the bifurcation plane, as is obvious from Figs. 3 and 5, however, they are objectively defined (Piccinelli et al., 2011).

Relative to previous studies, our WSS/WSSG figures/lines appear to be noisier since we used human “patient-specific” models instead of idealized (Kono et al., 2013; Lauric et al., 2018) or animal models (Meng et al., 2010). We do not consider this a limitation, but rather a result of controlling numerical viscosity, and the use of potentially “irregular” human models from the Aneurisk database. Smoothing the surfaces is indeed possible, but we consider the current approach the most sensitive, and consequently the most rigorous one.

Although we have shown that the modified algorithm better reconstructs the bifurcation, it still remains to quote Ford et al., namely that users must still “exercise their judgment if a particular

case is a good candidate for similar studies”. The code and associated tutorials are provided online, see <https://github.com/KVSlab/morphMan>, which also includes other methods for objectively altering additional morphological features of anatomically plausible vascular geometries.

## 5. Conclusion

We have shown that an incremental modification of Ford et al.’s aneurysm removal tools plausibly give better agreement with the reference surface and the corresponding stresses on the arterial wall. The modified algorithm can accelerate and broaden research on the hemodynamic stresses associated with aneurysm initiation, with the ultimate extrapolation to rupture prediction.

## Declaration of Competing Interest

The authors have no conflicts of interest to declare.

## Acknowledgment

The study was supported by The Research Council of Norway through a Center of Excellence grant to the Center for Biomedical Computing at Simula Research Laboratory, project number 179578. This work was also carried out as a part of the Centre for Cardiologial Innovation, and SIMMIS, project number 262827, funded by the Research Council of Norway. Computations were performed on the GPC supercomputer at the SciNet (Loken et al., 2010) HPC Consortium. SciNet is funded by: the Canada Foundation for Innovation under the auspices of Compute Canada; the Government of Ontario; Ontario Research Fund - Research Excellence; and the University of Toronto. Post processing was performed on the Abel Cluster, owned by the University of Oslo and the Norwegian metacenter for High Performance Computing (NOTUR), and operated by the Department for Research Computing at USIT, the University of Oslo IT-department, Grant No. nn9316k.

## Appendix

See Figs. 4 and 5.

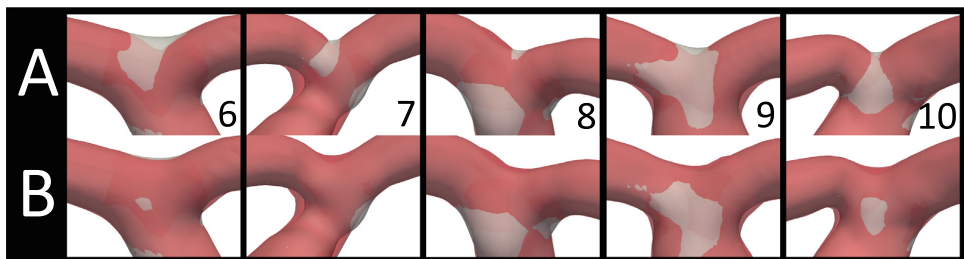
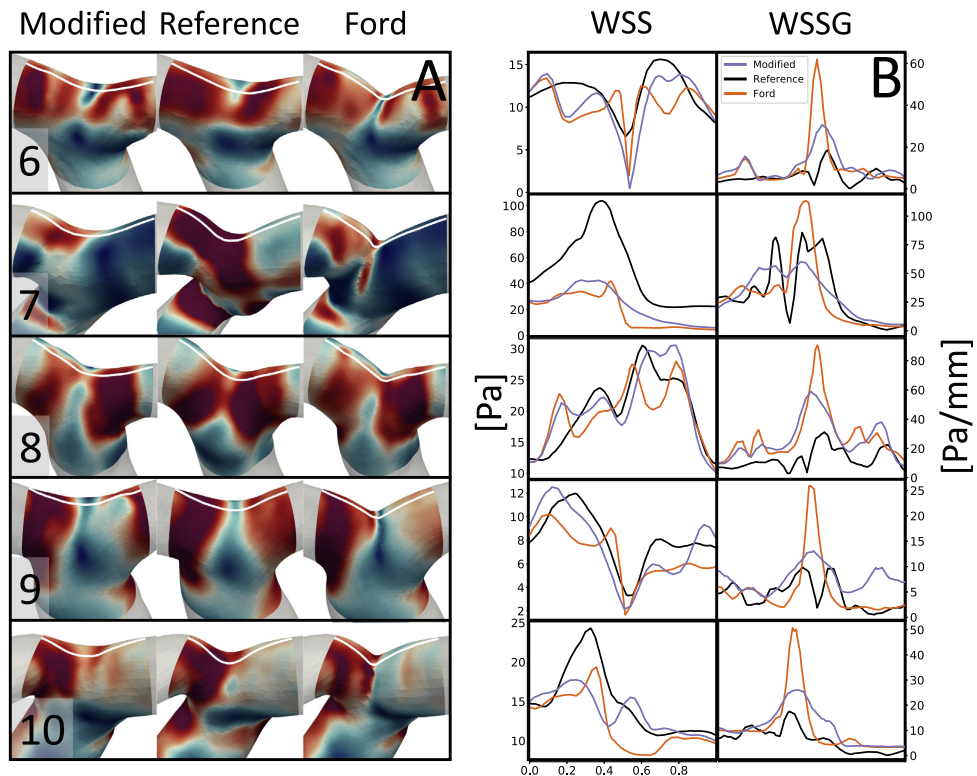


Fig. 4. The figure shows the reference surface in opaque, with the results of the original and modified surface reconstruction algorithms colored in red in sub-plots A and B, respectively.



**Fig. 5.** **A** Wall shear stress (WSS) maps from computational fluid dynamic simulations of the modified, reference, and Ford models, from left to right, respectively, and bifurcation lines shown in white. The absolute values of the WSS are indicated in the panel to the right. **B** WSS and WSS gradients along the bifurcation lines where the colors black, orange, and blue refers to the modified, reference, and Ford models, respectively. (For interpretation of the references to colour in this figure legend, the reader is referred to the web version of this article.)

## References

- Aneurisk-Team, 2012. AneuriskWeb project website, <http://ecm2.mathcs.emory.edu/aneuriskweb>. Web Site, accessed 01.08.2018.
- Antiga, L., Piccinelli, M., Botti, L., Ene-Iordache, B., Remuzzi, A., Steinman, D.A., 2008. An image-based modeling framework for patient-specific computational hemodynamics. *Med. Biol. Eng. Comput.* 46 (11), 1097–1112.
- Canham, P.B., Finlay, H.M., Kiernan, J.A., Ferguson, G.G., 1999. Layered structure of saccular aneurysms assessed by collagen birefringence. *Neurol. Res.* 21 (7), 618–626.
- Cebral, J.R., Castro, M.A., Burgess, J.E., Pergolizzi, R.S., Sheridan, M.J., Putman, C.M., 2005. Characterization of cerebral aneurysms for assessing risk of rupture by using patient-specific computational hemodynamics models. *Am. J. Neuroradiol.* 26 (10), 2550–2559.
- Cebral, J.R., Mut, F., Weir, J., Putman, C., 2011. Quantitative characterization of the hemodynamic environment in ruptured and unruptured brain aneurysms. *Am. J. Neuroradiol.* 32 (1), 145–151.
- Chnafa, C., Brina, O., Pereira, V., Steinman, D., 2018. Better than nothing: a rational approach for minimizing the impact of outflow strategy on cerebrovascular simulations. *Am. J. Neuroradiol.* 39 (2), 337–343.
- Ford, M.D., Hoi, Y., Piccinelli, M., Antiga, L., Steinman, D.A., 2009. An objective approach to digital removal of saccular aneurysms: technique and applications. *British J. Radiol.* 82 (Special Issue), S55–S61.
- Francis, S.E., Tu, J., Qian, Y., Avolio, A.P., 2013. A combination of genetic, molecular and haemodynamic risk factors contributes to the formation, enlargement and rupture of brain aneurysms. *J. Clin. Neurosci.* 20 (7), 912–918.
- Frösen, J., Piippo, A., Paetau, A., Kangasniemi, M., Niemelä, M., Hernesniemi, J., Jääskeläinen, J., 2004. Remodeling of saccular cerebral artery aneurysm wall is associated with rupture: histological analysis of 24 unruptured and 42 ruptured cases. *Stroke* 35 (10), 2287–2293.
- Gao, L., Hoi, Y., Swartz, D.D., Kolega, J., Siddiqui, A., Meng, H., 2008. Nascent aneurysm formation at the basilar terminus induced by hemodynamics. *Stroke* 39 (7), 2085–2090.
- Hendee, W.R., O'Connor, M.K., 2012. Radiation risks of medical imaging: separating fact from fantasy. *Radiology* 264 (2), 312–321.
- Hoi, Y., Wasserman, B.A., Xie, Y.J., Najjar, S.S., Ferruci, L., Lakatta, E.G., Gerstenblith, G., Steinman, D.A., 2010. Characterization of volumetric flow rate waveforms at the carotid bifurcations of older adults. *Physiol. Meas.* 31 (3), 291.
- Khan, M., Steinman, D.A., Valen-Sendstad, K., 2017. Non-Newtonian versus numerical rheology: Practical impact of shear-thinning on the prediction of stable and unstable flows in intracranial aneurysms. *Int. J. Num. Methods Biomed. Eng.* 33 (7), e2836.
- Khan, M., Valen-Sendstad, K., Steinman, D., 2015. Narrowing the expertise gap for predicting intracranial aneurysm hemodynamics: impact of solver numerics versus mesh and time-step resolution. *Am. J. Neuroradiol.* 36 (7), 1310–1316.
- Kono, K., Masuo, O., Nakao, N., Meng, H., 2013. De novo cerebral aneurysm formation associated with proximal stenosis. *Neurosurgery* 76 (6), E1080–E1090.
- Kulcsár, Z., Ugron, A., Marosfői, M., Berentei, Z., Paál, G., Szikora, I., 2011. Hemodynamics of cerebral aneurysm initiation: the role of wall shear stress and spatial wall shear stress gradient. *Am. J. Neuroradiol.* 32 (3), 587–594.
- Lauric, A., Greim-Kuczewski, K., Antonov, A., Dardik, G., Magida, J.K., Hippelheuser, J. E., Kono, K., Malek, A.M., 2018. Proximal parent vessel tapering is associated with aneurysm at the middle cerebral artery bifurcation. *Neurosurgery*.
- Loken, C., Gruner, D., Groer, L., Peltier, R., Bunn, N., Craig, M., Henriques, T., Dempsey, J., Yu, C.-H., Chen, J., et al., 2010. SciNet: lessons learned from building a power-efficient top-20 system and data centre. In: *Journal of Physics: Conference Series*, vol. 256(1). IOP Publishing, p. 012026.
- Malek, A.M., Alper, S., Izumo, S., 1999. Hemodynamic shear stress and its role in atherosclerosis. *JAMA* 282 (21), 2035–2042.
- Meng, H., Natarajan, S., Gao, L., Ionita, C., Kolega, J., Siddiqui, A., Mocco, J., 2010. Aneurysmal changes at the basilar terminus in the rabbit elastase aneurysm model. *Am. J. Neuroradiol.* 31 (3), E35–E36.
- Morbidiucci, U., Kok, A.M., Kwak, B.R., Stone, P.H., Steinman, D.A., Wentzel, J.J., et al., 2016. Atherosclerosis at arterial bifurcations: evidence for the role of hemodynamics and geometry. *Thrombosis Haemost.* 115 (3), 484–492.

- Mortensen, M., Valen-Sendstad, K., 2015. Oasis: A high-level/high-performance open source Navier-Stokes solver. *Comput. Phys. Commun.* 188, 177–188.
- Piccinelli, M., Bacigaluppi, S., Boccardi, E., Ene-îordache, B., Remuzzi, A., Veneziani, A., Antiga, L., 2011. Geometry of the internal carotid artery and recurrent patterns in location, orientation, and rupture status of lateral aneurysms: an image-based computational study. *Neurosurgery* 68 (5), 1270–1285.
- Piccinelli, M., Veneziani, A., Steinman, D.A., Remuzzi, A., Antiga, L., 2009. A framework for geometric analysis of vascular structures: application to cerebral aneurysms. *IEEE Trans. Med. Imaging* 28 (8), 1141–1155.
- Raghavan, M.L., Ma, B., Harbaugh, R.E., 2005. Quantified aneurysm shape and rupture risk. *J. Neurosurg.* 102 (2), 355–362.
- Rinkel, G.J.E., Djibuti, M., Algra, A., van Gijn, J., 1998. Prevalence and risk of rupture of intracranial aneurysms: a systematic review. *Stroke* 29 (1), 251–256.
- Schneiders, J., Marquering, H., Antiga, L., Van den Berg, R., VanBavel, E., Majoie, C., 2013. Intracranial aneurysm neck size overestimation with 3D rotational angiography: the impact on intra-aneurysmal hemodynamics simulated with computational fluid dynamics. *Am. J. Neuroradiol.* 34 (1), 121–128.
- Schneiders, J., Marquering, H., van den Berg, R., VanBavel, E., Velthuis, B., Rinkel, G., Majoie, C., 2014. Rupture-associated changes of cerebral aneurysm geometry: high-resolution 3d imaging before and after rupture. *Am. J. Neuroradiol.* 35 (7), 1358–1362.
- Skodvin, T.Ø., Johnsen, L.-H., Gjertsen, Ø., Isaksen, J.G., Sorteberg, A., 2017. Cerebral aneurysm morphology before and after rupture: nationwide case series of 29 aneurysms. *Stroke* 48 (4), 880–886.
- Sugiyama, S.-I., Meng, H., Funamoto, K., Inoue, T., Fujimura, M., Nakayama, T., Omodaka, S., Shimizu, H., Takahashi, A., Tominaga, T., 2012. Hemodynamic analysis of growing intracranial aneurysms arising from a posterior inferior cerebellar artery. *World Neurosurgery* 78 (5), 462–468.
- Taylor, C.A., Steinman, D.A., 2010. Image-based modeling of blood flow and vessel wall dynamics: applications, methods and future directions. *Ann. Biomed. Eng.* 38 (3), 1188–1203.
- Valen-Sendstad, K., Bergersen, A.W., Shimogonya, Y., Goubergrits, L., Bruening, J., Pallares, J., Cito, S., Piskin, S., Pekkan, K., Geers, A.J., et al., 2018. Real-world variability in the prediction of intracranial aneurysm wall shear stress: the 2015 International Aneurysm CFD Challenge. *Cardiovascular Eng. Technol.*, 1–21.
- Valen-Sendstad, K., Piccinelli, M., KrishnankuttyRema, R., Steinman, D.A., 2015. Estimation of inlet flow rates for image-based aneurysm CFD models: where and how to begin? *Ann. Biomed. Eng.* 43 (6), 1422–1431.
- Valen-Sendstad, K., Piccinelli, M., Steinman, D.A., 2014. High-resolution computational fluid dynamics detects flow instabilities in the carotid siphon: Implications for aneurysm initiation and rupture? *J. Biomech.* 47 (12), 3210–3216.
- Valen-Sendstad, K., Steinman, D.A., 2014. Mind the gap: impact of Computational Fluid Dynamics solution strategy on prediction of intracranial aneurysm hemodynamics and rupture status indicators. *Am. J. Neuroradiol.* 35 (3), 536–543.
- Wiebers et al., 2003. Unruptured intracranial aneurysms: natural history, clinical outcome, and risks of surgical and endovascular treatment. *Lancet* 362 (9378), 103–110.
- Xiang, J., Natarajan, S.K., Tremmel, M., Ma, D., Mocco, J., Hopkins, L.N., Siddiqui, A.H., Levy, E.I., Meng, H., 2011. Hemodynamic-morphologic discriminants for intracranial aneurysm rupture. *Stroke* 42 (1), 144–152.



**IV. A framework for automated and objective modification of tubular structures:  
Application to the internal carotid artery**







# A framework for automated and objective modification of tubular structures: Application to the internal carotid artery

Aslak W. Bergersen | Henrik A. Kjeldsberg | Kristian Valen-Sendstad

Department of Computational Physiology, Simula Research Laboratory, Fornebu, Akershus, Norway

## Correspondence

Kristian Valen-Sendstad, Department of Computational Physiology, Simula Research Laboratory, Fornebu, Akershus, Norway.

Email: kvs@simula.no

## Funding information

Norges Forskningsråd, Center for Cardiological Innovation, SIMMIS, Grant/Award Number: 262827

## Abstract

Patient-specific medical image-based computational fluid dynamics has been widely used to reveal fundamental insight into mechanisms of cardiovascular disease, for instance, correlating morphology to adverse vascular remodeling. However, segmentation of medical images is laborious, error-prone, and a bottleneck in the development of large databases that are needed to capture the natural variability in morphology. Instead, idealized models, where morphological features are parameterized, have been used to investigate the correlation with flow features, but at the cost of limited understanding of the complexity of cardiovascular flows. To combine the advantages of both approaches, we developed a tool that preserves the patient-specificity inherent in medical images while allowing for parametric alteration of the morphology. In our open-source framework *morphMan* we convert the segmented surface to a Voronoi diagram, modify the diagram to change the morphological features of interest, and then convert back to a new surface. In this paper, we present algorithms for modifying bifurcation angles, location of branches, cross-sectional area, vessel curvature, shape of bends, and surface roughness. We show qualitative and quantitative validation of the algorithms, performing with an accuracy exceeding 97% in general, and proof-of-concept on combining the tool with computational fluid dynamics. By combining *morphMan* with appropriate clinical measurements, one could explore the morphological parameter space and resulting hemodynamic response using only a handful of segmented surfaces, effectively minimizing the main bottleneck in image-based computational fluid dynamics.

## KEYWORDS

computational geometry, geometric modification, patient-specific modeling, synthetic data generation, uncertainty quantification, vascular morphology

## 1 | INTRODUCTION

Cardiovascular diseases present an enormous economic burden to society and accounted for 31.8% of all 55.9 million deaths worldwide in 2017.<sup>1</sup> Of equal importance are the individual psychological effects in stroke patients, for instance, reduction in quality of life and higher rates of depression.<sup>2,3</sup> Although systemic risk factors affect the entire

cardiovascular system, for instance, cerebral aneurysms and carotid stenoses are focally distributed.<sup>4,5</sup> The latter highlights the importance of blood flow-induced wall shear stresses, ultimately governed by morphology.<sup>6</sup>

Generally, there are two approaches to investigate the correlation between morphology and flow: (a) use patient-specific models and correlate morphological features with flow response,<sup>6-9</sup> or (b) use idealized models where morphological features are parameterized, often combined with one or two patient-specific geometries to confirm the results.<sup>10-13</sup> On the one hand, patient-specific models are realistic but would require an extensive database of segmented surfaces to isolate the effect of a single morphological feature in a multifactorial disease. Furthermore, segmentation has been shown to be a labor-intensive and error-prone process.<sup>14,15</sup> On the other hand, idealized models have the advantage of a parametric, objective, and isolated modification of morphological features. Therefore, creating a wide range of models is efficient and can be used to explore combinations of multiple morphological features simultaneously. However, the idealized models can be an over-simplified representation of the underlying patient-specific geometry, causing results to phenotypically differ from physiological flows. For example, turbulent-like flow features in the internal carotid artery (ICA)<sup>16</sup> is absent in idealized models<sup>13,17,18</sup> because the ICA, a tortuous vessel with area variation, is approximated by a straight tube.

We hypothesized that we could combine the two suboptimal approaches, and keep the advantages of both while minimizing the limitations, by altering morphological features parametrically in isolation on patient-specific geometries. To achieve this goal, we created the open-source framework *morphMan*,<sup>19</sup> where we implemented the six algorithms presented here for robust, objective, automatic, and reproducible modification. Four of the algorithms were motivated by morphological features that have been found to correlate with, or are the definition of, cardiovascular diseases: bifurcation angles,<sup>20,21</sup> cross-sectional area,<sup>22-24</sup> curvature and torsion,<sup>7,25,26</sup> and the shape of a bend.<sup>27</sup> The two remaining algorithms provide additional flexibility and robustness of the tools and can control the surface roughness, and location and angle of smaller branches. We here present the main steps in each algorithm and show qualitative and quantitative validation of the algorithms. We also exemplify the usage of the tool in combination with computational fluid dynamics (CFD) to investigate the flow response.

## 2 | METHOD

### 2.1 | Data acquisition

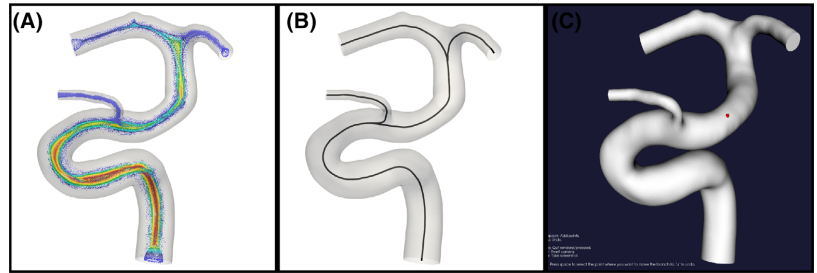
We identified two relevant cohorts in the open-source Aneurisk database.<sup>28</sup> The first was 10 segmented surfaces of the ICA from 3D angiograms without vascular abnormalities, and 65 ICA with saccular aneurysms. From the first cohort, we used one model for visualizing the algorithms in the Method section, and another for a proof-of-concept in combination with CFD. The former was carefully chosen such that all the six algorithms could easily be visualized, while the latter was the first model in the cohort. For the qualitative and quantitative results, we used the 15 first consecutive models from the second cohort, a trade-off between the limited space for visualization and capturing the variability of the models. Details of the image acquisition can be found in Sangalli et al.<sup>29</sup>

### 2.2 | Overview

A fundamental part of the algorithms is the Voronoi diagram (VD)<sup>30</sup> and associated centerlines, as defined in Antiga et al.<sup>31</sup> Briefly, a VD is an alternative representation of a surface by a union of spheres. In this context, we can colloquially describe a VD as a point cloud with associated radii corresponding to the minimal inscribed sphere radius of each point and can be converted back to a surface by enveloping the union of spheres.<sup>32</sup> As such, a VD can be used to represent any complex surface, even with sharp edges. The associated centerline is defined as minimizing the cost function  $1/R$ , where  $R$  is the radius of each sphere in the VD, from a given start and endpoint (see Figure 1A,B, for an example of a VD and centerline, respectively).

Inspired by Ford et al.,<sup>33</sup> we convert the surface to a VD, perform alterations to the diagram, and then envelope the latter back to a surface. The approach is analogous to performing a Fourier transformation of a signal, apply any filters to the modes, before performing an inverse operation to obtain the altered signal. In contrast to a surface, a clear advantage of a VD is that we can modify each point in isolation without connectivity to the surrounding points. We present the main features of each algorithm and show a step-by-step visualization, accompanied by a more detailed explanation

**FIGURE 1** Panel A shows a VD where each point is colored by the radius, and panel B shows the corresponding centerline of the ICA model. Panel C displays a screenshot of the interactive window for providing points on the surface interactively



in the caption. Although the algorithms are motivated by cardiovascular diseases, the step-by-step visualizations are slightly exaggerated to make easy-to-understand illustrations and are not necessarily physiologically relevant. The region of interest (ROI) should ideally be computed objectively with landmarking algorithms,<sup>7,34</sup> but the ROI can also be specified interactively, as shown in Figure 1C.

In the following, the terms upstream and downstream is relative to the direction of the blood flow. Furthermore, in the visualization of the algorithms, we have defined  $c_j$  and  $p_i$  as point  $j$  on the centerline and  $i$  in the VD,  $\theta$  and  $\psi$  are angles,  $\mathbf{v}$  are vectors, and  $\mathbf{t}$  and  $\mathbf{n}$  are tangents and normals.

For the algorithms to be easily extendable or modified, we created a framework *morphMan* with general methods for modifying the centerline, surface, and VDs used to implement the six algorithms. The framework is written in *Python*, using the visualization toolkit<sup>35</sup> and vascular modeling toolkit<sup>31</sup> packages. Our code is accompanied by online tutorials and demos (<https://morphman.readthedocs.io/>), but for completeness, we here briefly explain the two ways of executing the code: first, importing the functions in *Python* or second, execute the algorithms on the command line on the form *morphman-[algorithm-name]*. To see all the variables to change for each algorithm, the user can add the flag *-h*. The algorithms from this paper correspond to *morphMan v1.0*.

### 2.3 | Bifurcation angles

To adjust bifurcation angles, we build on our previously validated method for reconstructing bifurcations.<sup>36</sup> The main idea is to remove the VD and centerline from the bifurcation before rotating the branches around the points  $c_2$  and  $c_3$  in the plane spanned by the vectors  $\mathbf{v}_1 = \mathbf{d}_2 - \mathbf{d}_1$  and  $\mathbf{v}_2 = \mathbf{d}_3 - \mathbf{d}_1$  (Figure 2A,B). To rebuild the bifurcation with the rotated branches, we created new centerlines using splines and extrapolate the VD along with these (Figure 2C,D).

### 2.4 | Branch location and angle

The algorithm for rotating and moving a branch is visualized in Figure 3. Briefly, the main idea is to identify the section of the VD that constitutes the ROI, including any downstream branches (Figure 3A). The Voronoi ROI is then removed, and the surface is recreated to find the surface normal of the previous location (Figure 3B). The Voronoi ROI is then translated to the new point and rotated relative to the old and new surface normals and centerline tangents. The branch can then be rotated  $\psi$  and  $\theta$  degrees around the surface normal or tangent, respectively, giving the user full control over the branch angle (Figure 3C). The resulting surface is visualized in Figure 3D.

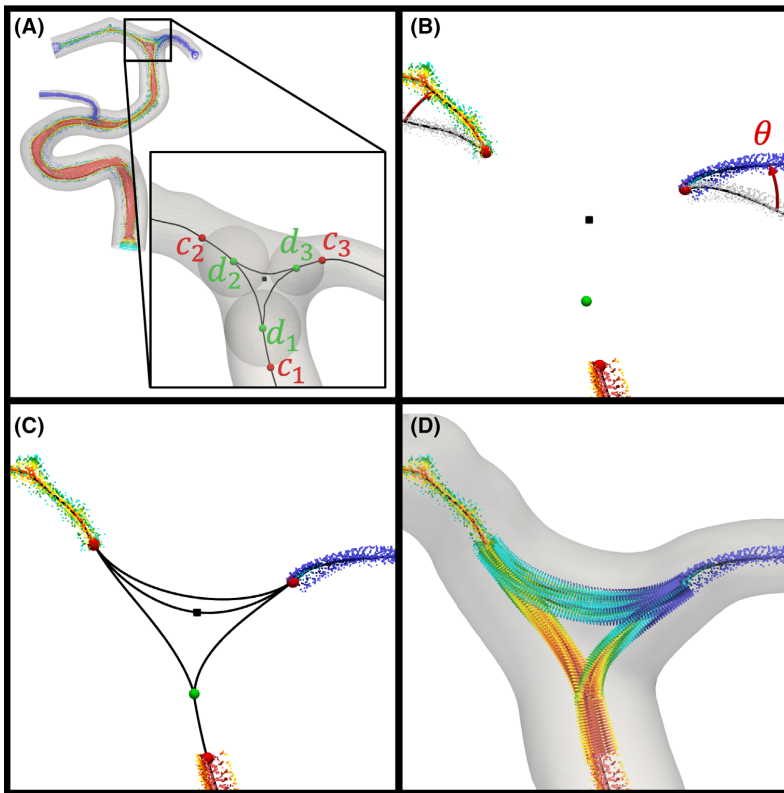
The algorithm can be used for three different purposes; *removal*, *translation*, or *rotation* of a branch. Additionally, the branch can also be clamped at the outlet, meaning that the outlet is kept fixed while there is a transitional rotation or translation of the rest of the branch. An illustration of the latter is shown in the Result section (Figure 8N).

### 2.5 | Cross-sectional area

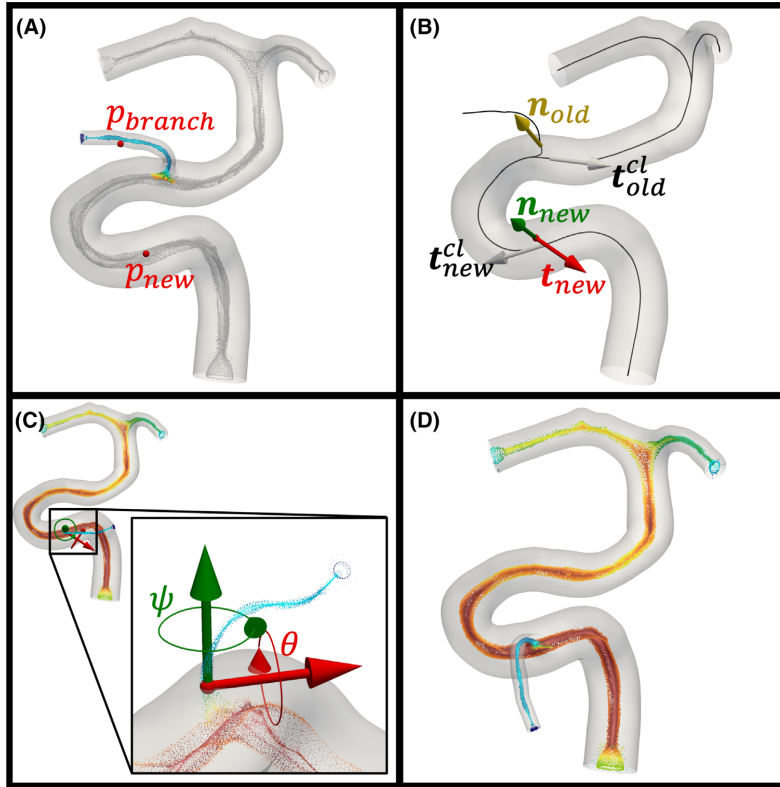
There is a wide range of vascular pathologies that are linked to abnormal cross-sectional area. Therefore, we present a general and flexible algorithm where the area can be modified according to a function  $F$ . The algorithm is presented in

Figure 4 where the panels A-C are generic, while the output shown in panel D is specific to  $F$ . The idea is to first measure the area along the ROI and define a variable  $F$  to control the cross-sectional area (Figure 4A,B). We then loop over each point in the VD ( $p_j$ ) and change the distance to the centerline and radius with a factor  $F_j$  (Figure 4C). The resulting modified VD is then enveloped to create a new surface (Figure 4D). Motivated by clinical observations, we present four functions to increase or decrease the area ( $F^{\text{area}}$ ),<sup>7</sup> create a symmetric or asymmetric stenosis or fusiform aneurysm ( $F^{\text{local}}$ ),<sup>22</sup> impose a linear change in area over a region ( $F^{\text{linear}}$ ),<sup>13</sup> and control the area variation ( $F^{\text{variation}}$ ).<sup>37</sup>

1. The first method is for increasing or decreasing the cross-sectional area in the ROI and corresponds to setting  $F^{\text{area}}$  equal to a constant. Of note is that the latter is related to the change in radius, to exemplify;  $F^{\text{area}} = 1.2$  results in a 20% increase in radius.



**FIGURE 2** A step-by-step outline of the algorithm for altering bifurcation angles. Panel A shows the full model in opaque with the VD colored according to the radius. The zoomed frame shows the bifurcation of interest, chosen by selecting one outlet at each side of the bifurcation, and a landmarking of the bifurcation; the green points mark where the centerlines diverge ( $d_{1, 2, 3}$ ), the red points mark the outer bound of the bifurcation ( $c_{1, 2, 3}$ ), and the black point is the center of the bifurcation. Although not visualized, we also define a bifurcation plane spanned by the vectors  $v_1 = d_2 - d_1$  and  $v_2 = d_3 - d_1$ , through the bifurcation center. Panel B shows the zoomed frame from panel A, where the VD and centerlines are removed between  $c_1, c_2$ , and  $c_3$ . Also, the original VD of the branches is shown in grey, while the new VD is rotated  $\theta = 30^\circ$  around  $c_2$  and  $c_3$  in the bifurcation plane, shown in color. The bifurcation center and point  $d_1$  are also visualized. Panel C shows a total of four new centerlines, two of which are passed from  $c_1$ , through the point  $d_1$ , and to the branches. The remaining two centerlines start and end at the branches, where one of them is passed through the bifurcation center. The new centerlines are created using Kochanek splines.<sup>55</sup> The lower centerline is included to avoid an artificial “dent” in the surface as described in Bergersen et al.<sup>36</sup> Panel D shows the new VD where we have extrapolated the old VD along the new centerlines. The new surface is shown in opaque



**FIGURE 3** A step-by-step visualization of the algorithm for altering a smaller branch. Panel A shows the original surface, where we have marked the branch of interest with the point  $p_{\text{branch}}$  and the new location to move the branch  $p_{\text{new}}$ . The VD of the ROI is marked in a rainbow color scheme while the diverging branch is marked grey. Note that any downstream branches of the segment marked with  $p_{\text{branch}}$  would also have been included in the ROI. Panel B shows the reconstructed surface, where we have removed the marked VD region. We then find the intersection between the centerline to the branch of interest and the reconstructed surface and compute the surface normal  $n_{\text{old}}$  at the intersection point, shown in yellow. The surface normal and tangents of the new location  $n_{\text{new}}$ ,  $t_{\text{new}}$  are shown in green and red, respectively. Additionally, we define the tangent along at the closest centerline point to both the old and new locations,  $t_{\text{old}}^{\text{cl}}$  and  $t_{\text{new}}^{\text{cl}}$ , shown in white. Panel C shows the VD of the branch translated to the new location  $p_{\text{new}}$  and rotated to adjust for the angle between  $n_{\text{old}}$  and  $n_{\text{new}}$ , and the centerline tangents  $t_{\text{old}}^{\text{cl}}$  and  $t_{\text{new}}^{\text{cl}}$ . We adjust for the centerline tangents because the base of the branch often is an ellipsoid, which gives rise artifacts if the long-axis is perpendicular to the centerline direction. We then allow for additional rotation  $\psi$  and  $\theta$  degrees around  $n_{\text{new}}$  and  $t_{\text{new}}$ , respectively. To avoid any artifacts from the rotation, we keep the “base” of the branch fixed, defined as any point with more than a  $90^\circ$  angle to  $n_{\text{new}}$  with  $p_{\text{new}}$  as the origin. Panel D shows the VD and the new surface. We have here set  $\theta = 30^\circ$  and  $\psi = 90^\circ$

2. We here define  $F^{\text{local}}$  to alter the local cross-sectional area by creating a narrowing or widening of the vessel, mimicking a stenosis or fusiform aneurysm. We have here defined  $F$  as

$$F_j^{\text{local}} = \begin{cases} 1 - C \sin\left(\pi \frac{\text{distance}_j}{L}\right), & \text{if } C \leq 1 \\ 1 + C \sin\left(\pi \frac{\text{distance}_j}{L}\right), & \text{if } C > 1 \end{cases}, \quad (1)$$

where  $C$  is the percentage of narrowing or increase in the center of the ROI,  $\text{distance}_j$  is the curvilinear distance from the start to point  $j$  on the centerline, and  $L$  is the total length of the centerline in the ROI. We have also included the option of skewing the local change in the area to be asymmetrical. Based on the angle to the normal of the Frenet frame,<sup>38</sup> we alter  $F^{\text{local}}$  and  $v_{ij}$  such that the change is only towards one side of the wall. An illustration of a symmetric and asymmetric modification is shown in the Result section (Figure 8B,C).

To remove a local narrowing or widening, we have added the option to create a linear change in the area between two points, achieved by  $F^{\text{variation}}$  defined as

$$F_j^{\text{linear}} = \left( A_{\text{start}} + (A_{\text{end}} - A_{\text{start}}) \frac{\text{distance}_j}{L} \right) / A_j, \quad (2)$$

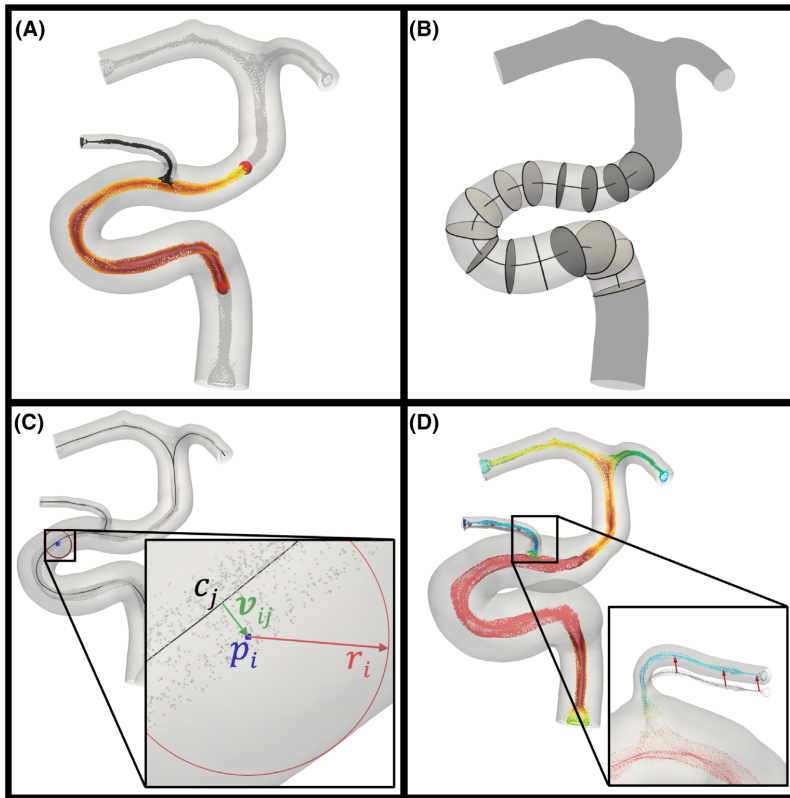


**FIGURE 4** A step-by-step visualization of the algorithm for altering the cross-sectional area. Panel A shows two points in red marking the ROI. The VD of the ROI is marked in a rainbow color scheme while the diverging branch and the remaining geometry are marked in black and grey, respectively. Panel B shows an enveloped surface from the VD shown in color in panel A. Of note is that the new surface does not include the diverging branch and is shown in opaque while the remaining model is shown in dark grey. With the new surface, we measure the area using slices, as shown with highlighted edges. We have here visualized every 30th slice. Using the measured area, we define the factor  $F_j$  for each point along the centerline, which determines how the area should change. Panel C focuses on one point in the VD ( $p_i$ ), marked in blue, and the associated minimal inscribed sphere radius ( $r_i$ ), shown in red. The zoomed frame also shows the closest centerline point ( $c_j$ ) computed using linear interpolation between the discrete points defining the centerline, and the vector  $v_{ij} = p_i - c_j$ . Each VD point in the ROI is moved  $v_{ij}(F_j - 1)$  and given a new radius defined as  $r_i^{\text{new}} = r_i^{\text{old}} F_j$ . We have here set  $F = 1.5$  to achieve a 50% increase in the cross-sectional area. Panel D shows the manipulated VD, where we have inserted the VD of the diverging branch again, adjusting for the local changes in the area where the branch diverged, as indicated by the red arrows in the zoomed frame. The new surface enveloped from the modified VD is shown in opaque

where  $A_{\text{start}}$ ,  $A_j$ , and  $A_{\text{end}}$  is the area at the start, centerline point  $j$ , and end of the ROI, respectively. The linear change of the cross-sectional area can be used to remove a fusiform aneurysm or a stenosis.  $F_j^{\text{variation}}$  is defined such that we can control the ratio between the largest and smallest cross-sectional area in the ROI. Let the area ratio be defined as  $A_{\text{ratio}} = A_{\text{max}}/A_{\text{min}}$ . We can then increase or decrease the ratio by setting

$$F_j^{\text{variation}} = \left( \frac{A_j}{A_{\text{mean}}} \right)^\beta, \quad (3)$$

where  $A_j$  is the area at point  $j$  along the centerline,  $A_{\text{mean}}$  is the average cross-sectional area, and  $\beta$  is the factor controlling the change. The fraction is  $<1$ , and  $>1$  when  $A_j$  is below and above average, respectively. Alternatively, one can specify the new area ratio, and not  $\beta$ , by inserting  $A_j^{\text{new}} = \pi (r_j F_j^{\text{variation}})^2$  and Equation (3) into the expression for  $A_{\text{ratio}}$  and rearrange, to obtain

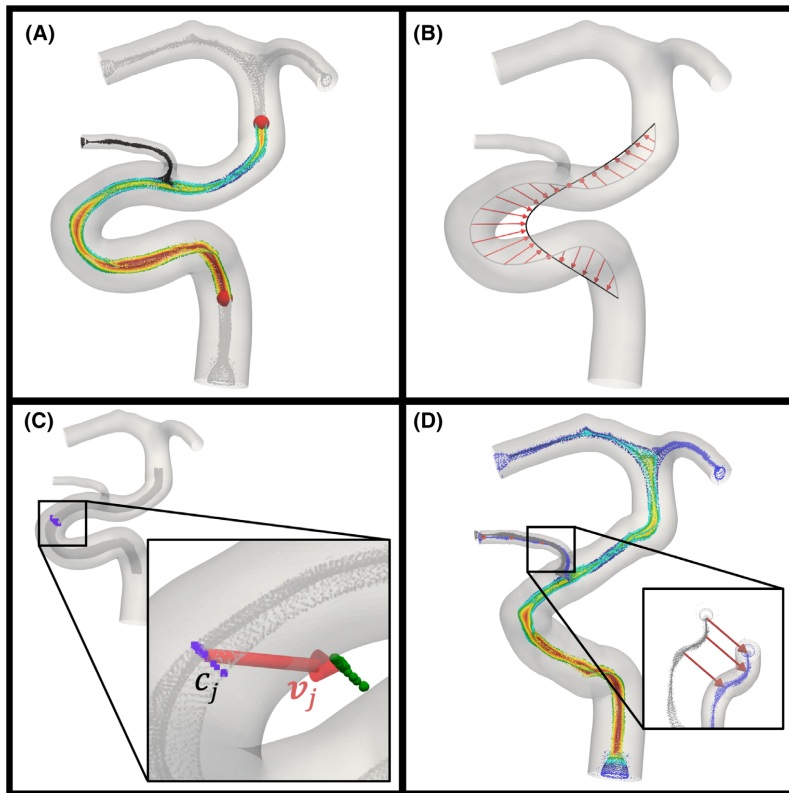


**FIGURE 5** A step-by-step depiction of the algorithm for altering curvature and torsion of a vessel. Panel A shows the original model in opaque with two points marking the ROI in red. The VD of the ROI is marked in a rainbow color scheme while the diverging branch and the remaining regions are marked in black and grey, respectively. Panel B shows the original centerline of the ROI in grey, and a new smoothed centerline in black with red arrows marking the corresponding points on each line. Panel C focuses on the VD points closest to the centerline point ( $c_j$ ), marked in purple. The points are translated  $v_j$ , marked in red. The points in the new location are marked in green. To increase the curvature and torsion, we instead move the points  $-v_j$ . Panel D shows the manipulated VD, where we have inserted the VD of the diverging branch again, adjusting for the local changes where the branch diverged, as indicated by the red arrows in the zoomed frame. The new surface enveloped from the modified VD is shown in opaque

$$\beta = \frac{1 \log(A_{\text{ratio}}^{\text{new}})}{2 \log(A_{\text{ratio}}^{\text{old}})} - \frac{1}{2}, \quad (4)$$

where the superscripts *new* and *old* refers to the modified and original surface, respectively. From Equation (4), we can see that  $\beta > 0$  and  $-0.5 < \beta < 0$  would increase and decrease the area ratio, respectively. Setting  $\beta = -0.5$  corresponds to an area ratio of 1, and decreasing  $\beta$  any further would only increase the area ratio again.

## 2.6 | Curvature and torsion

The algorithm for increasing or decreasing the overall curvature and torsion of a vessel is presented in Figure 5. The main idea is to smooth the centerline in the ROI, resulting in a second centerline (Figure 5A,B). The distance between the two centerlines is then used to move the VD (Figure 5C), before we adjust any diverging branches and create the new surface as visualized in Figure 5D. Oppositely, to increase the curvature and torsion, all vectors are multiplied by  $-1$ , effectively “flipping” the direction of  $v_j$ .

## 2.7 | Shape of a bend

In contrast to section 2.6, we here present an algorithm to manipulate only one bend, not a larger segment. The keystone of the algorithm is to identify two directions of the bend, referred to as the horizontal and vertical direction (Figure 6A,B). Colloquially, we can imagine that the bend of the artery follows the path of a semi-ellipse, where the two directions are analogous to the short and long axis. The displacement in the horizontal direction is defined as

$$v_{h,j} = 4\alpha v_h \left( \frac{(j-N)(M-j)}{(M-N)^2} \right), \quad (5)$$

and for the vertical direction

$$v_{v,j} = \begin{cases} \beta v_v \left( \frac{j_{\text{mid}}^2 - j^2}{j_{\text{mid}}^2 - N^2} \right) & \text{for } j < j_{\text{mid}} \\ -\beta v_v \left( \frac{j - j_{\text{mid}}}{M - j_{\text{mid}}} \right)^{\frac{1}{2}} & \text{for } j \geq j_{\text{mid}} \end{cases}, \quad (6)$$

where  $j = N, N + 1, \dots, M - 1, M$  are the indices of the centerline point  $p_j$ , with  $N, M$ , and  $j_{\text{mid}}$  corresponding to points  $p_0, p_1$ , and  $p_{\text{mid}}$  as defined in Figure 6B. We then move the VD a length  $\alpha$  and  $\beta$  in each direction (Figure 6C) before adjusting the diverging branch and converting back to a surface, as shown in Figure 6D.

## 2.8 | Surface roughness

Classical smoothing methods like Laplace reduces the surface roughness, but also affect other morphological features. Inspired by Ford et al,<sup>33</sup> we here overcome these challenges by smoothing the VD instead of the surface, as outlined in Figure 7. Briefly, the main idea is to recognize that only the spheres with the smallest radius contribute to the high-frequency surface features. Therefore, we loop over each point in the VD and check if the radius is larger than a local, relative threshold. For the sake of completeness, we can also reverse the process; instead of removing points, we add new points at random locations with smaller radii within a specified bandwidth, resulting in an increase in the surface roughness.



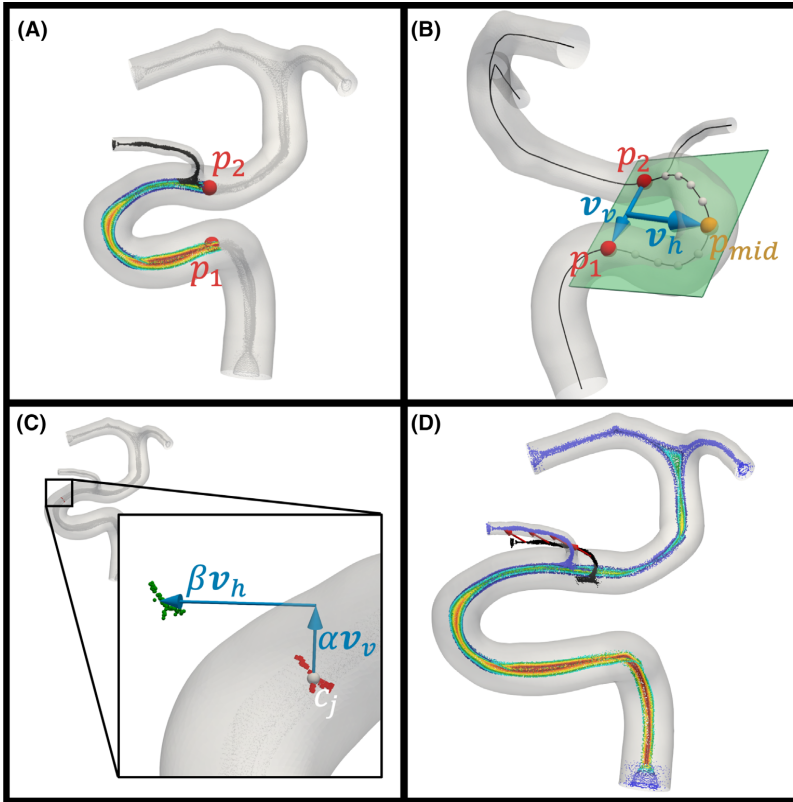


**FIGURE 6** A step-by-step depiction of the algorithm for altering the shape of a bend. Panel A shows the ROI, marked by two landmarking points  $p_1$  and  $p_2$ . The VD of the ROI is marked in a rainbow color scheme while the diverging branch and the remaining geometry are marked in black and grey, respectively. Panel B shows the two directions we can move the bend,  $v_h$  and  $v_v$ , referred to as the horizontal and vertical direction, respectively. The vertical direction is defined as  $v_v = p_1 - p_2$  and the horizontal is the vector perpendicular to  $v_v$  that resides in the least-squares plane approximating  $n$  equally spaced points along the centerline in the ROI, shown as small white spheres along the centerline. The plane is visualized in opaque green. Here the plane is aligned with  $p_{mid}$ , but that is coincidental. Panel C focuses on the centerline point ( $c_j$ ) and visualize how the VD is moved. For each point  $j$ , excluding any diverging branches defined in panel A, we move the closest Voronoi points a distance  $\alpha v_{v,j} + \beta v_{h,j}$ , as defined in Equations (5) and (6). For the horizontal displacement, only the ROI is affected. Panel D shows the altered VD, including the diverging branch, which is moved according to the local changes, and the new surface is shown in opaque

## 2.9 | Validation of the algorithms

From section 2.3-2.8, we identified a total of 15 different ways of modifying the surfaces, now referred to as modes. To demonstrate qualitative results, we applied each mode to 15 different surfaces, where we zoomed in on the ROI for visual inspection. From the complete set of 15 modes, we identified six where we could specify a target value and perform a quantitative evaluation. We then applied each mode in the subset to all the 15 surfaces and reported the relative error, defined as  $E = |\text{target-observed}|/\text{target}$ . For inflation and linear change of the cross-sectional area, the error is measured in each point along the centerline in the ROI, whereas the other categories are based on point measurements.

When converting a VD to a surface, one has to set a resolution  $N$ , in each spatial direction. To investigate how execution time and accuracy of the result depends on the resolution we varied  $N$  from 120, the lower limit for recreating

all surfaces without an error, to 300, at which point we no longer observed any difference with an additional increase. In total, we performed 360 *modifications* (15 *models*  $\times$  4 *spatial resolutions*  $\times$  6 *modes*) for the quantitative results.

To enable reproducibility and improve transparency in science, we have created an online repository with the scripts, we used to perform the validation of the algorithms and all the resulting surfaces.<sup>39</sup>

## 2.10 | Computational fluid dynamics

To exemplify the type of studies that *morphMan* enables, we modified the area in the ICA<sup>37</sup> in a single model to investigate the global hemodynamic response. We modified the surface using the algorithm described in section 2.5, resulting in two new geometries with increased and decreased area variability ( $A_{\text{ratio}}$ ). The models were meshed using the

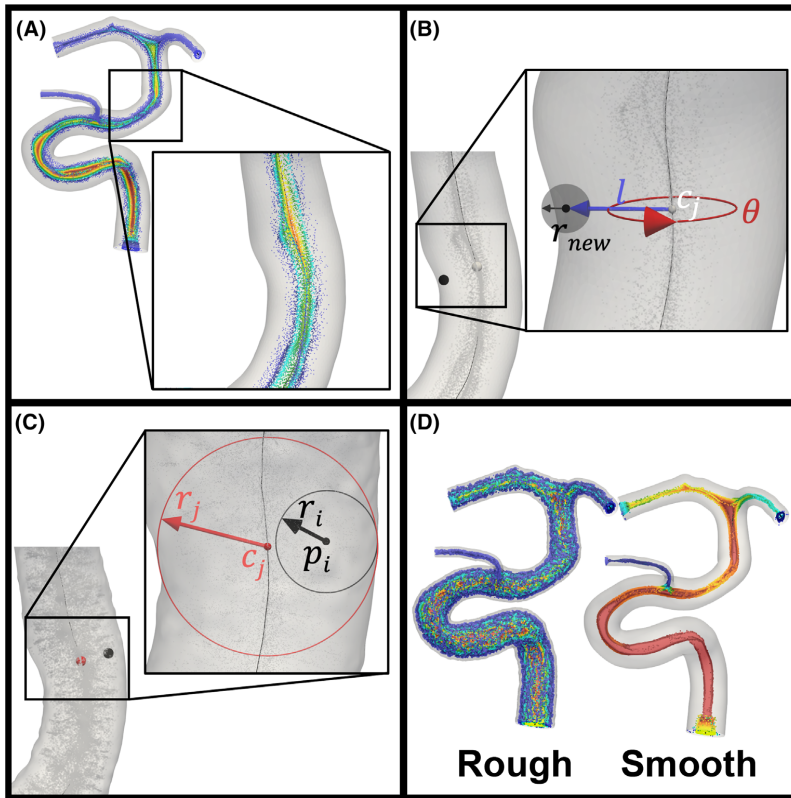
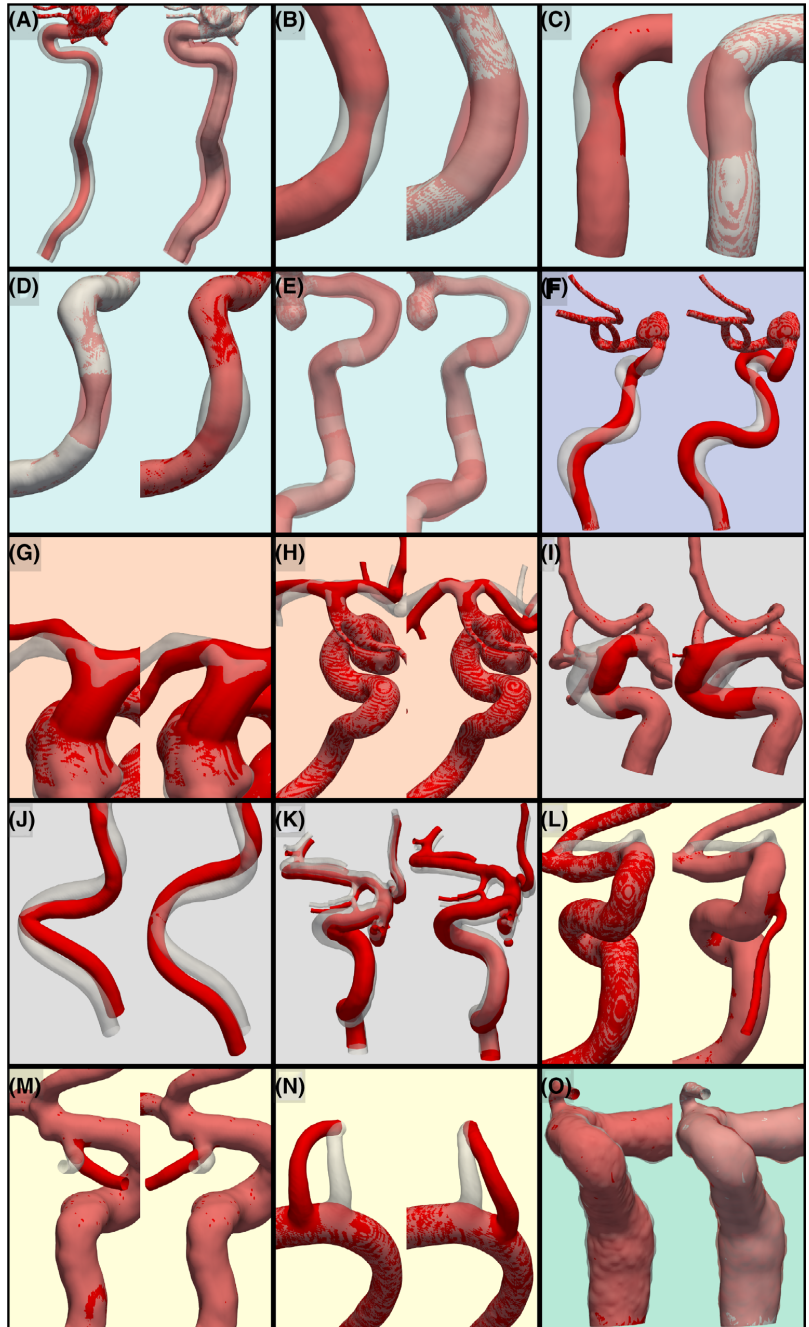


**FIGURE 7** A step-by-step depiction of the algorithm for altering the surface roughness. Panel A shows an unsmoothed VD and the original surface. Here, the entire geometry is the ROI, but we will focus on the section shown in the zoomed frame. Panel B shows an outline of the algorithm for adding noise to the VD. For each centerline point ( $c_j$ ), we first compute the Frenet frame, giving a tangent, normal, and bi-normal vector of the centerline. We then add  $n$  number of new points, where  $n$  is drawn from a normal distribution with mean and SD defined by the user. The location of the new point is a distance  $l$  from the centerline in the direction of the *frenetNormal* <sub>$j$</sub> , shown in blue, rotated  $\theta$  degrees around the *frenetTangent* <sub>$j$</sub> , illustrated with a red circle. The radius of the new point, illustrated by a black arrow, is defined as the distance between the new point and the surface times  $r_{\text{scale}}$ . The parameters  $l$ ,  $\theta$ , and  $r_{\text{scale}}$  are drawn from uniform distributions given as  $l \in [\text{distance}_{\text{lower}}, \text{distance}_{\text{upper}}]$ ,  $\theta \in [0, 360]$ ,  $r_{\text{scale}} \in [\text{radius}_{\text{min}}, \text{radius}_{\text{max}}]$ . Note that the bounds are provided by the user. Panel C shows the section from the zoomed frame from panel A from a surface where we have added noise. For smoothing, we loop over each point in the VD ( $p_i$ ) find the closest point on the centerline ( $c_j$ ) with the corresponding radii  $r_i$  and  $r_j$ , respectively. If  $r_i < (1 - \text{smoothing factor})r_j$ , then point  $i$  is excluded. Panel D shows the noisy and smoothed VDs and their convoluted surfaces, from left to right, respectively

**FIGURE 8** Each panel shows the result of applying the 15 modes on 15 different models. We have given each panel a background color according to which algorithm was applied. Panel A-E shows changes in cross-sectional area with a light blue background, panel F shows changes in curvature with a crayola background, panel G-H shows changes in bifurcation angle in an orange background, panel I-K shows changes in a bend with a grey background, panel L-N shows a branch being removed, moved or rotated with a yellow background, and panel O shows smoothing from a rough surface to the left, and creating noise to the right with a mint-colored background



vascular modeling toolkit<sup>31</sup> and consisted of ~3 million tetrahedrons, with four boundary layers, and flow extensions five times the local radius.

To investigate the flow, we used *Oasis*, an open-source, second-order energy-conserving and minimally dissipative CFD solver, previously used for biomedical applications<sup>40,41</sup> and is verified<sup>42</sup> and validated.<sup>43</sup> We assumed the blood to

behave as a Newtonian fluid<sup>44,45</sup> with a kinematic viscosity of  $\nu = 0.0035 \text{ m}^2/\text{second}$ . We used the inlet waveform from Hoi et al<sup>46</sup> and scaled the mean flow rate with the inlet area.<sup>47</sup> We imposed a varying pressure condition on the outlets<sup>48</sup> to impose the precomputed flow split.<sup>49</sup> We simulated the flow over two cardiac cycles, using 10 000 time steps per cycle. The presented results are from the second cycle to wash out the unrealistic initial conditions. To visualize the results, we showed the Q-criterion<sup>50</sup> at peak systole, and velocity traces over the last cardiac cycle from three locations in the ICA.

### 3 | RESULTS

#### 3.1 | Qualitative results

We first focus on the qualitative results, presented in Figure 8 with a different background color for each of the algorithms presented in section 2.3-2.8. To highlight the effects of the algorithms, the modified and input surfaces are marked in red and white, respectively. Consistent for each panel is that we show a decrease of the relevant value to the left and an increase to the right. The general trends for all modifications are that the geometries are still intuitive anatomical plausible, and the models are only modified in the ROI and indistinguishable elsewhere.

We are now focusing on the changes in the cross-sectional area shown in Figure 8A-E with a light blue background. Panel A shows a constant 50% decrease and increase in radius ( $F^{\text{area}} = 0.5$  and  $1.5$ ) with ROI from the inlet up to the first bifurcation. In panel B, we show a 50% symmetrical local narrowing and widening of the artery over a total length of four times the local radius ( $F^{\text{local}}$  with  $C = 0.5$  and  $1.5$ ). The asymmetrical counterpart is shown in panel C. In panel D, the input surfaces have an added local narrowing or widening, which we removed by modifying the area to change linearly ( $F^{\text{linear}}$ ). A visualization of amplifying and reducing the area variation ( $F^{\text{variation}}$ ) is shown in panel E with  $\beta = \pm 0.5$ . Note that in contrast to all other panels, we here visualize both surfaces in opaque, where we can observe that the surfaces cross at the same locations, but inversely. Thus, showing that the locations with a mean area are unchanged while the extremes are reduced or amplified. To summarize panels from A to E, the resulting surfaces all reflect the expected change applied for the different modes of cross-sectional area modification.

In panel F with a crayola colored background, we show a decrease and increase in overall curvature and torsion of the ICA with a relaxation factor of 0.35 and 20 000 iterations using a Laplace method. In panel G, we rotate one upstream branch in the bifurcation  $\pm 15^\circ$  and keeping the other fixed, while in panel H, we rotate both branches shown with an orange background. The geometries are both anatomically plausible in both G and H, despite an aneurysm upstream of bifurcation in the former. Looking at the three modes for manipulating a bend marked with a grey background color, we show a change in the horizontal direction panel I ( $\alpha = \pm 0.5$ ), in the vertical direction in panel J ( $\beta = \pm 0.5$ ), and in both directions simultaneously in panel K ( $\alpha = \pm 0.5$  and  $\beta = \pm 0.5$ ). In panel L, we first remove, then move the location of the ophthalmic artery before we in panel M rotate a smaller branch  $\pm 90^\circ$  around the surface normal, and in panel N, we move a branch while keeping the outlet fixed, all with a yellow background color. Although we have moved the location of the branch, we cannot observe any artifacts proximal to the orifice either at the new or old location. Finally, in panel O with a mint-colored background, we show the surface smoothing algorithm with  $n$  drawn from a distribution with a mean of zero and a SD of one,  $l \in [0.7, 0.9]$ , and  $r_{\text{scale}} \in [1.05, 1.3]$ . We have used the surface with added noise as input for the smoothing to visually create a more significant difference.

#### 3.2 | Quantitative results

From the quantitative results presented in Table 1, we observe that the accuracy of the area algorithms improves when moving from  $N = 120$  to  $N = 200$ . Moreover, for *stenosis*, *area ratio*, and *linear area*, the error consistently decrease with increasing  $N$ , while for *area* and *bulge*, the error increases slightly. In contrast, the accuracy of the bifurcation angle is unaffected by the resolution of the new surface since the error measure only depends on the centerline.

Shifting focus to the execution times, we observe that the modification of one model varies for each algorithm, but is within minutes on a personal laptop. Furthermore, we can also see that the conversion of the VD to a surface is a bottleneck in the algorithms. However, even when increasing the resolution, the execution times are still reasonable.

**TABLE 1** A summary of the error and execution times for 360 modifications

Algorithm	Target	Value	Resolution of reconstructed surface (-)			
			$N = 120$	$N = 200$	$N = 250$	$N = 300$
Area	20%	Time (s)	$49.29 \pm 15.49$	$204.70 \pm 90.61$	$338.12 \pm 118.48$	$530.64 \pm 148.16$
		Error (%)	$3.29 \pm 3.72$	$1.70 \pm 2.13$	$1.89 \pm 2.15$	$2.05 \pm 1.98$
Stenosis	50%	Time (s)	$35.92 \pm 9.25$	$119.54 \pm 24.47$	$235.89 \pm 59.62$	$437.55 \pm 122.94$
		Error (%)	$4.30 \pm 1.91$	$1.76 \pm 0.83$	$1.22 \pm 0.57$	$0.94 \pm 0.44$
Bulge	50%	Time (s)	$53.64 \pm 19.29$	$194.07 \pm 79.07$	$255.08 \pm 96.46$	$320.13 \pm 101.13$
		Error (%)	$0.51 \pm 0.38$	$0.22 \pm 0.20$	$0.23 \pm 0.14$	$0.29 \pm 0.15$
Area ratio	2.0	Time (s)	$39.98 \pm 10.78$	$113.92 \pm 32.46$	$191.17 \pm 50.69$	$298.65 \pm 84.98$
		Error (%)	$4.25 \pm 4.73$	$3.32 \pm 4.14$	$3.10 \pm 3.95$	$2.89 \pm 3.87$
Linear area	Linear change	Time (s)	$75.43 \pm 22.23$	$217.85 \pm 77.86$	$273.67 \pm 74.49$	$429.94 \pm 146.64$
		Error (%)	$6.34 \pm 1.79$	$1.90 \pm 5.37$	$1.41 \pm 2.42$	$1.17 \pm 2.50$
Bifurcation angle	30°	Time (s)	$71.67 \pm 21.69$	$165.38 \pm 63.35$	$282.25 \pm 113.77$	$473.00 \pm 243.93$
		Error (%)	$6.06 \pm 4.78$	$6.06 \pm 4.78$	$6.06 \pm 4.78$	$6.06 \pm 4.78$

Note: The general trends are that the error is reduced for increasing resolution, except for the bifurcation angle. The latter is because the error is based on the centerlines and not the cross-sectional area. Note that for a typical resolution of  $N = 250$ , the mean relative error is at the order of 2.3%. Additionally, the execution times increase consistently with the resolution.

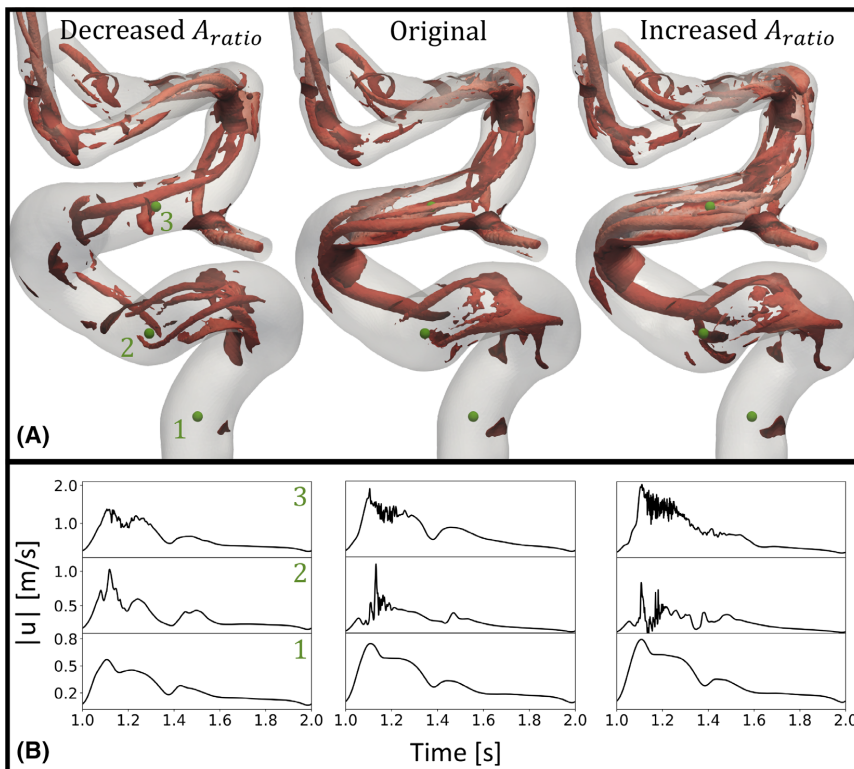


**FIGURE 9** Panel A shows the iso volume of the Q-criterion at peak systole with an increasing  $A_{ratio}$  from left to right, respectively. We have also marked three probes (1-3), where we have sampled the velocity. Panel B shows the velocity magnitude trace in probe location (1-3) from the second cardiac cycle

### 3.3 | Proof-of-concept: Application to the internal carotid artery

In Figure 9A, we present the modified models with increasing area variation from left to right with Q-criterion at peak systole and three probe locations marked in green. Focusing first on the general flow features in the original model shown in the middle, we observe that the flow develops turbulent-like vortices in the first bend. These vortices are transported downstream and further increased throughout the ICA due to the area variation. Visually comparing the flow fields to the left and right, it is a clear trend that an increase in  $A_{\text{ratio}}$  corresponds to an increase in the intensity of flow instabilities. The increase is also reflected by the velocity traces shown in Figure 9B, where the turbulent-like fluctuations are more high-frequency and last longer after peak systole for increased  $A_{\text{ratio}}$ .

## 4 | DISCUSSION

We have here presented a framework for robust, objective, automatic, and reproducible modification of tubular structures with applications to the ICA. We validated the algorithms both qualitatively and quantitatively with reasonable execution times. To exemplify the use, we also performed CFD on two modified models and compared the flow fields. The framework was developed to be in concert with the much-used<sup>14</sup> open-source vascular modeling toolkit, which has implemented tools for segmentation of medical images and meshing,<sup>31</sup> and morphological characterization.<sup>51</sup> Combined, the tools can be effective instruments in a patient-specific medical image-based CFD platform.

We have here shown the applicability of the algorithms to the ICA, but we can also use the algorithms to modify other vascular beds. To exemplify, we changed the angle and location of one right pulmonary vein and performed CFD on the two models (Figure 10A). Details of the modification, meshing, and CFD can be found in the Appendix.

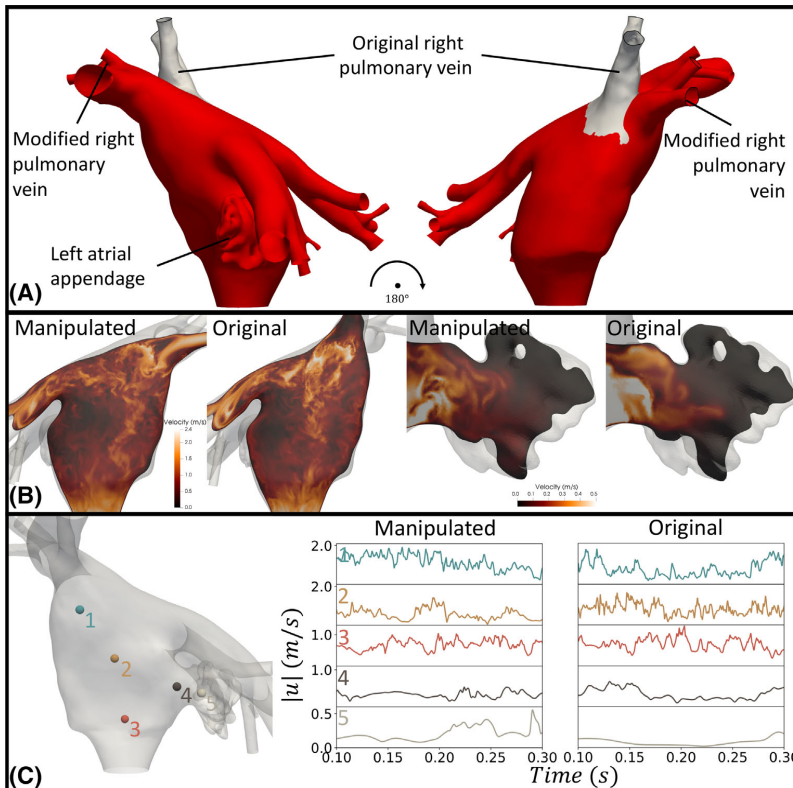


**FIGURE 10** Panel A displays the manipulated atrium model in red with an artificial extension at the mitral orifice from two views, with anatomical features marked. Additionally, we also show the original geometry in white. The outlets that have been manipulated are marked in black at the inlet. Panel B shows the velocity in two slices for comparing the manipulated and original model. Panel C shows the velocity magnitude from five probes in the atrium and the appendage from 0.1 to 0.3 second

Focusing first on the general flow features presented to the left in Figure 10B, we can observe that the turbulent-like structures are shifted towards the wall in the manipulated model. Reflected in the velocity traces shown in Figure 10C, there is also a deeper flow penetration with higher velocities in probe five in the manipulated model. That being said, with  $n = 1$ , the above results have a very limited scientific value. We only intended to demonstrate that morphological modifications can alter the flow. The latter can be used to gain fruitful insight into mechanisms of cardiovascular disease. More generally, the tool is in principle applicable to any tubular structure, and cardiovascular bed by extension. Ultimately, the only constraint is physiology realistic scenarios and the user's imagination.

Although not empathized in our proof-of-concept, how the geometry is altered should be motivated from physiological measurements. In the area and bifurcation angle algorithms, the target is defined in the algorithm, but for curvature and bend, there are many possible target definitions like mean curvature, max curvature, or the angle of a bend. To ease the search for appropriate parameters to match the desired modification, we implemented extra functionality where we apply the alteration to only the centerline, as a surrogate measure. We then sample the parameter space and find a set of values that will achieve the set target. The user can then apply these values to perform the alteration.

Although the algorithms were verified and validated, it is important to bear in mind that the modifications, and therefore resulting surfaces, are inevitably idealized and not patient-specific. Thus, we do not fully circumvent the aforementioned inherent limitation of parametrization. However, the number of associated limitations is drastically reduced, as the medical image is the basis of the operation. Furthermore, since *morphMan* was designed to be adaptable, the user has the possibility to control the mathematical functions describing the resulting surface, for instance, of a stenosis. Implementing new workflows, or altering existing ones, is straightforward as the code is open-source. Hence, the six presented algorithms can therefore be viewed as examples of workflows that *morphMan* enables.

A consequence of performing alterations on the VD is that the reconstructed output surface has to be re-meshed if used for CFD. An alternative to our approach is to manipulate the surface or volume mesh directly using methods like free-form deformation,<sup>52</sup> radial basis functions,<sup>53</sup> or inverse distance weighting.<sup>54</sup> In particular, free-form deformation would be effective to create similar algorithms for manipulating cross-sectional area, curvature, and a bend. However, altering small branches, or objectively reconstructing a bifurcation would be challenging. Therefore, modifying the VD directly is the only approach for implementing all six presented algorithms.

A critical step in the algorithms is the conversion of the VD to a surface. One then has to find an adequate balance between acceptable execution times and needed resolution, which can be challenging to predict a priori. If the resolution is not chosen carefully, the models could be reconstructed incorrectly and might exhibit undesired features; for instance, where two arteries are close to each other, or the ratio between the smallest diameter and the extent of the model is large. As a remedy, we check the new surface and provide the user with a warning if reconstructed incorrectly. Furthermore, recreating the sharp edges at the inlet and outlet is challenging with a limited resolution. We circumvent the latter by using an open surface and clip the inlet and outlet after reconstructing the VD back to a surface.

From extensive experience as users and developers of the tools, we wish to highlight some features of each algorithm. The algorithm for adjusting the bifurcation angle is a mathematical method and does not guaranty physiologically plausible morphology if used on other vascular beds. We have mainly tested the algorithm on ICA and middle cerebral artery bifurcations, and if used for very wide or narrow bifurcation angles, we recommend not to include the two centerlines between the two downstream branches. Additionally, the bifurcation algorithm can also be used to remove saccular aneurysms.<sup>33,36</sup> Of note for the branch algorithm is that it can be applied to equally sized bifurcations as well. However, the branch algorithm is sensitive to the surface curvature of the new location of the branch. If the new location has considerably higher surface curvature, there might be artifacts around the orifice of the altered branch. Another feature is that the curvilinear length of the vessel is altered when manipulating a bend or the curvature. Therefore, the area variation in the original ROI will be compressed or stretched out. A possible remedy is to run the area modification algorithm to remove any unphysiological features. Nevertheless, the user has to exercise discretion when applying *morphMan* and should always substantiate modifications with clinical observations and measurements. Careful usage combined with a handful of accurately segmented models, *morphMan* can be used to create new models that would reflect the morphological variability found in extensive databases. By reducing the number of required models, we are effectively mitigating the segmentation bottleneck in medical image-based CFD.

## 5 | CONCLUSION

We have here shown qualitative and quantitative validation of algorithms for an objective, reproducible, robust, and automated modification of geometric features in tubular structures. We have also shown how the algorithms can be combined with CFD to investigate hypotheses of the link between morphology and flow response. The proposed algorithms can contribute to acceleration and widening of the latter, which ultimately can impact evidence-based medicine and contribute to answer basal research questions.

### ACKNOWLEDGMENTS

The work was carried out as a part of the Centre for Cardiological Innovation, and SIMMIS, project number 262827, funded by the Research Council of Norway. Computations were performed on the Abel Cluster, owned by the University of Oslo and the Norwegian metacenter for High-Performance Computing (NOTUR), and operated by the Department for Research Computing at USIT, the University of Oslo IT-department, grant number nn9316k.

### CONFLICT OF INTEREST

The authors have no conflicts of interest.

### ORCID

Aslak W. Bergersen  <https://orcid.org/0000-0001-5063-3680>

Henrik A. Kjeldsberg  <https://orcid.org/0000-0002-7764-4248>

Kristian Valen-Sendstad  <https://orcid.org/0000-0002-2907-0171>

### REFERENCES

- Roth GA, Abate D, Abate KH, et al. Global, regional, and national age-sex-specific mortality for 282 causes of death in 195 countries and territories, 1980–2017: a systematic analysis for the global burden of disease study 2017. *Lancet*. 2018;392(10159):1736-1788.
- Sturm JW, Donnan GA, Dewey HM, et al. Quality of life after stroke: the north East Melbourne stroke incidence study (NEMESIS). *Stroke*. 2004;35(10):2340-2345.
- Edmondson D, Richardson S, Falzon L, Davidson KW, Mills MA, Neria Y. Posttraumatic stress disorder prevalence and risk of recurrence in acute coronary syndrome patients: a meta-analytic review. *PLoS One*. 2012;7(6):e38915.
- de Weerd M, Greving JP, Hedblad B, et al. Prevalence of asymptomatic carotid artery stenosis in the general population: an individual participant data meta-analysis. *Stroke*. 2010;41(6):1294-1297.
- Brisman JL, Song JK, Newell DW. Cerebral aneurysms. *N Engl J Med*. 2006;355(9):928-939.
- Lee SW, Antiga L, Spence JD, Steinman DA. Geometry of the carotid bifurcation predicts its exposure to disturbed flow. *Stroke*. 2008;39(8):2341-2347.
- Piccinelli M, Bacigaluppi S, Boccardi E, et al. Geometry of the internal carotid artery and recurrent patterns in location, orientation, and rupture status of lateral aneurysms: an image-based computational study. *Neurosurgery*. 2011;68(5):1270-1285.
- Cebal JR, Castro MA, Burgess JE, Pergolizzi RS, Sheridan MJ, Putman CM. Characterization of cerebral aneurysms for assessing risk of rupture by using patient-specific computational hemodynamics models. *Am J Neuroradiol*. 2005;26(10):2550-2559.
- Chiastra C, Gallo D, Tasso P, et al. Healthy and diseased coronary bifurcation geometries influence near-wall and intravascular flow: A computational exploration of the hemodynamic risk. *J Biomech*. 2017;58:79-88.
- Xenos M, Alemu Y, Zamfir D, et al. The effect of angulation in abdominal aortic aneurysms: fluid-structure interaction simulations of idealized geometries. *Med Biol Eng Comput*. 2010;48(12):1175-1190.
- Bhagavan D, Di Achille P, Humphrey J. Strongly coupled morphological features of aortic aneurysms drive intraluminal thrombus. *Sci Rep*. 2018;8:13273.
- Lauric A, Hippelheuser JE, Malek AM. Induction of aneurysmogenic high positive wall shear stress gradient by wide angle at cerebral bifurcations, independent of flow rate. *J Neurosurg*. 2018;1:1-11.
- Lauric A, Greim-Kuczewski K, Antonov A, et al. Proximal parent vessel tapering is associated with aneurysm at the middle cerebral artery bifurcation. *Neurosurgery*. 2018;84:1082-1089.
- Valen-Sendstad K, Bergersen AW, Shimogonya Y, et al. Real-world variability in the prediction of intracranial aneurysm wall shear stress: the 2015 international aneurysm CFD Challenge. *Cardiovasc Eng Technol*. 2018;9:544-564.
- Berg P, Vofß S, Saalfeld S, et al. Multiple Aneurysms AnaTomy CHallenge (MATCH): phase I: segmentation. *Cardiovasc Eng Technol*. 2018;9:565-581.
- Valen-Sendstad K, Piccinelli M, Steinman DA. High-resolution computational fluid dynamics detects flow instabilities in the carotid siphon: implications for aneurysm initiation and rupture? *J Biomech*. 2014;47(12):3210-3216.
- Baharoglu MI, Lauric A, Gao BL, Malek AM. Identification of a dichotomy in morphological predictors of rupture status between sidewall-and bifurcation-type intracranial aneurysms. *J Neurosurg*. 2012;116(4):871-881.



18. Farnoush A, Avolio A, Qian Y. Effect of bifurcation angle configuration and ratio of daughter diameters on hemodynamics of bifurcation aneurysms. *Am J Neuroradiol*. 2013;34(2):391-396.
19. Kjeldsberg HA, Bergersen AW, Valen-Sendstad K. morphMan: automated manipulation of vascular geometries. *Journal of Open Source Software*. 2019;4(35):1065.
20. Cui Y, Zeng W, Yu J, et al. Quantification of left coronary bifurcation angles and plaques by coronary computed tomography angiography for prediction of significant coronary stenosis: A preliminary study with dual-source CT. *PLoS One*. 2017;12(3):e0174352.
21. Ingebrigtsen T, Morgan MK, Faulder K, Ingebrigtsen L, Sparr T, Schirmer H. Bifurcation geometry and the presence of cerebral artery aneurysms. *J Neurosurg*. 2004;101(1):108-113.
22. Sakalihasan N, Limet R, Defawe OD. Abdominal aortic aneurysm. *Lancet*. 2005;365(9470):1577-1589.
23. Hansson GK. Inflammation, atherosclerosis, and coronary artery disease. *N Engl J Med*. 2005;352(16):1685-1695.
24. European Carotid Surgery Trialists' Collaborative Group et al. MRC European carotid surgery trial: interim results for symptomatic patients with severe (70–99%) or with mild (0–29%) carotid stenosis. *Lancet*. 1991;337(8752):1235-1243.
25. Sangalli LM, Secchi P, Vantini S, Veneziani A. A case study in exploratory functional data analysis: geometrical features of the internal carotid artery. *J Am Stat Assoc*. 2009;104(485):37-48.
26. Lauric A, Hippelheuser J, Safain MG, Malek AM. Curvature effect on hemodynamic conditions at the inner bend of the carotid siphon and its relation to aneurysm formation. *J Biomech*. 2014;47(12):3018-3027.
27. Waihrich E, Clavel P, Mendes G, Iosif C, Kessler IM, Mounayer C. Influence of carotid siphon anatomy on brain aneurysm presentation. *Am J Neuroradiol*. 2017;38(9):1771-1775.
28. Aneurisk-Team, AneuriskWeb project website, <http://ecm2.mathcs.emory.edu/aneuriskweb/>; 2012. <http://ecm2.mathcs.emory.edu/aneuriskweb/>. Accessed July 1, 2018.
29. Sangalli LM, Secchi P, Vantini S, et al. AneuRisk65: A dataset of three-dimensional cerebral vascular geometries. *Electron J Stat*. 2014;8(2):1879-1890.
30. Dey TK, Zhao W. Approximate medial axis as a voronoi subcomplex. Paper presented at: Proceedings of the seventh ACM symposium on Solid modeling and applications ACM; 2002. p. 356–366.
31. Antiga L, Piccinelli M, Botti L, Ene-Iordache B, Remuzzi A, Steinman DA. An image-based modeling framework for patient-specific computational hemodynamics. *Med Biol Eng Comput*. 2008;46(11):1097-1112.
32. Huttenlocher DP, Kedem K, Sharir M. The upper envelope of Voronoi surfaces and its applications. *Discrete Comput Geom*. 1993;9(3):267-291.
33. Ford M, Hoi Y, Piccinelli M, Antiga L, Steinman D. An objective approach to digital removal of saccular aneurysms: technique and applications. *Br J Radiol*. 2009;82:S55-S61.
34. Bogunović H, Pozo JM, Cárdenas R, et al. Automated landmarking and geometric characterization of the carotid siphon. *Med Image Anal*. 2012;16(4):889-903.
35. Schroeder WJ, Lorensen B, Martin K. *The Visualization Toolkit: an Object-Oriented Approach to 3D Graphics*. Clifton Park, NY: Kitware; 2004.
36. Bergersen AW, Chnafa C, Gallo D, Piccinelli M, Steinman DA, Valen-Sendstad K. Automated and objective removal of bifurcation aneurysms: incremental improvements, and validation against healthy controls. *J Biomech*. 2019;96:109342.
37. Schimansky S, Patel S, Rahal J, Lauric A, Malek AM. Extradural internal carotid artery caliber dysregulation is associated with cerebral aneurysms. *Stroke*. 2013;44(12):3561-3564.
38. Bishop RL. There is more than one way to frame a curve. *Amer Math Monthly*. 1975;82(3):246-251.
39. Bergersen AW, Kjeldsberg HA, Valen-Sendstad K. Data for "A Framework for Automated and Objective Modification of Tubular Structures: Application to the Internal Carotid Artery". figshare; 2019. [https://figshare.com/articles/Data\\_for\\_An\\_Automated\\_Framework\\_for\\_Objective\\_Modification\\_of\\_Tubular\\_Structures\\_with\\_Focus\\_on\\_Patient-Specific\\_Blood\\_Vessels\\_/9731000/2](https://figshare.com/articles/Data_for_An_Automated_Framework_for_Objective_Modification_of_Tubular_Structures_with_Focus_on_Patient-Specific_Blood_Vessels_/9731000/2).
40. Valen-Sendstad K, Steinman DA. Mind the gap: impact of computational fluid dynamics solution strategy on prediction of intracranial aneurysm hemodynamics and rupture status indicators. *Am J Neuroradiol*. 2014;35(3):536-543.
41. Arzani A. Accounting for residence-time in blood rheology models: do we really need non-Newtonian blood flow modelling in large arteries? *J R Soc Interface*. 2018;15(146):20180486.
42. Mortensen M, Valen-Sendstad K. Oasis: A high-level/high-performance open source Navier–Stokes solver. *Comput Phys Commun*. 2015;188:177-188.
43. Bergersen AW, Mortensen M, Valen-Sendstad K. The FDA nozzle benchmark: "in theory there is no difference between theory and practice, but in practice there is". *Int J Numer Methods Biomed Eng*. 2019;35(1):e3150.
44. Khan M, Steinman D, Valen-Sendstad K. Non-Newtonian versus numerical rheology: practical impact of shear-thinning on the prediction of stable and unstable flows in intracranial aneurysms. *Int J Numer Methods Biomed Eng*. 2017;33(7):e2836.
45. Khan M, Valen-Sendstad K, Steinman D. Direct numerical simulation of laminar-turbulent transition in a non-axisymmetric stenosis model for newtonian vs. shear-thinning non-Newtonian rheologies. *Flow Turbulence Combust*. 2019;102(1):43-72.
46. Hoi Y, Wasserman BA, Xie YJ, et al. Characterization of volumetric flow rate waveforms at the carotid bifurcations of older adults. *Physiol Meas*. 2010;31(3):291-302.
47. Valen-Sendstad K, Piccinelli M, KrishnankuttyRema R, Steinman DA. Estimation of inlet flow rates for image-based aneurysm CFD models: where and how to begin? *Ann Biomed Eng*. 2015;43(6):1422-1431.

48. Gin R, Straatman AG, Steinman DA. A dual-pressure boundary condition for use in simulations of bifurcating conduits. *J Biomech Eng.* 2002;124(5):617-619.
49. Chnafa C, Brina O, Pereira V, Steinman D. Better than nothing: a rational approach for minimizing the impact of outflow strategy on cerebrovascular simulations. *Am J Neuroradiol.* 2018;39(2):337-343.
50. Hunt JCR, Wray AA, Moin P. *Eddies, streams, and convergence zones in turbulent flows. Studying Turbulence Using Numerical Simulation Database II. Paper presented at: Proceedings of the Summer Program, Center for Turbulence Research Report.* Stanford, CA: Stanford University and NASA; 1988:193-208.
51. Piccinelli M, Veneziani A, Steinman DA, Remuzzi A, Antiga L. A framework for geometric analysis of vascular structures: application to cerebral aneurysms. *IEEE Trans Med Imaging.* 2009;28(8):1141-1155.
52. Sederberg TW, Parry SR. Free-form deformation of solid geometric models. *ACM SIGGRAPH Comput Graph.* 1986;20(4):151-160.
53. Forti D, Rozza G. Efficient geometrical parametrisation techniques of interfaces for reduced-order modelling: application to fluid-structure interaction coupling problems. *Int J Comput Fluid Dyn.* 2014;28(3-4):158-169.
54. Shepard D. A two-dimensional interpolation function for irregularly-spaced data. Paper presented at: Proceedings of the 1968 23rd ACM national conference ACM; 1968. p. 517-524.
55. Kochanek DH, Bartels RH. Interpolating splines with local tension, continuity, and bias control. *ACM SIGGRAPH Comput Graph.* 1984; 18:33-41.
56. Rosset A, Spadola L, Ratib O. OsiriX: an open-source software for navigating in multidimensional DICOM images. *J Digit Imaging.* 2004; 17(3):205-216.
57. OsiriX-Team, OsiriX DICOM database, <https://www.osirix-viewer.com/resources/dicom-image-library/>; 2019. <https://www.osirix-viewer.com/resources/dicom-image-library/>. Accessed July 1, 2019.
58. Yushkevich PA, Piven J, Hazlett HC, et al. User-guided 3D active contour segmentation of anatomical structures: significantly improved efficiency and reliability. *Neuroimage.* 2006;31(3):1116-1128.
59. Ahrens J, Geveci B, Law C. Paraview: an end-user tool for large data visualization. *The Visualization Handbook.* Amsterdam: Elsevier; 2005:717-731.
60. Schmidt R, Singh K. Meshmixer: an interface for rapid mesh composition. Paper presented at: ACM SIGGRAPH 2010 Talks; 2010. p. 6.
61. ISO. *Cardiovascular Implants—Cardiac Valve Prostheses Part 1: General Requirements.* Geneva, Switzerland: International Organization for Standardization; 2015.

**How to cite this article:** Bergersen AW, Kjeldsberg HA, Valen-Sendstad K. A framework for automated and objective modification of tubular structures: Application to the internal carotid artery. *Int J Numer Meth Biomed Engng.* 2020;e3330. <https://doi.org/10.1002/cnm.3330>

## APPENDIX

We segmented a cardiac electrocardiography-gated computed tomography image, labeled CARDIX in the OsiriX<sup>56</sup> DICOM database,<sup>57</sup> in ITK-SNAP<sup>58</sup> using growing regions. The surface was then clipped and smoothed using Paraview<sup>59</sup> and Meshmixer<sup>60</sup> and then modified using the algorithm for manipulating a branch, see section 2.4. The new center of the branch was chosen to be 1 cm towards the mitral orifice and to adjust for the changes in surface normals, and the branch was rotated 49.28° around the normal of the old and new surface normals. We then added flow extension to the pulmonary veins four times the local radius, and a conical shaped extension at the mitral orifice to avoid backflow at the outlet.

The volumetric meshes were created using VMTK, and with  $\Delta x = 0.6$  mm in the atrium, resulting in 12 million tetrahedral cells, but with a refinement in the pulmonary veins to ensure at least 10 cells across the diameter. For simplicity, we simulated the atrial morphology at one instant in time, corresponding to peak E-wave velocity, with  $Q = 400$  mL/second and a rigid wall. The flow rate is on the high-side of a healthy normal individual.<sup>61</sup> The flow split between each pulmonary vein was scaled according to the area and prescribed as a parabolic velocity profile, and for the outflow boundary conditions we prescribed  $p = 0$  at the mitral orifice. We simulated the flow for 0.3 second, equivalent to  $\sim 3$  flow-through based on the average curvilinear length along the centerlines from the outlets to the inlet and the velocity at the inlet, with a time step of  $5 \times 10^{-5}$  seconds.